UNIVERSIDADE FEDERAL DO RIO GRANDE DO SUL
INSTITUTO DE FÍSICA – ESCOLA DE ENGENHARIA – INSTITUTO DE QUÍMICA – INSTITUTO DE INFORMÁTICA
PROGRAMA DE PÓS-GRADUAÇÃO EM MICROELETRÔNICA

CAROLINE DOS SANTOS SOARES

Quantum-Corrected Monte Carlo Device Simulator for n-type Tri-gate Transistors

Thesis presented in partial fulfillment
of the requirements for the degree of
PhD in Microelectronics

Advisor: Prof. Dr. Gilson Inácio Wirth

Porto Alegre
2023

CIP – CATALOGAÇÃO NA PUBLICAÇÃO

dos Santos Soares, Caroline

Quantum-Corrected Monte Carlo Device Simulator for n-type Tri-gate Transistors / Caroline dos Santos Soares. -- 2023.

111 f.

Orientador: Gilson Inácio Wirth.

Tese (Doutorado) -- Universidade Federal do Rio Grande do Sul, Instituto de Informática, Programa de Pós-Graduação em Microeletrônica, Porto Alegre, BR-RS, 2023.

1. Monte Carlo device simulator. 2. Quantum Corrections. 3. Effective Potential. 4. FinFET. 5. Nanowire FET. I. Wirth, Gilson Inácio, orient. II. Título.

UNIVERSIDADE FEDERAL DO RIO GRANDE DO SUL
Reitor: Prof. Carlos André Bulhões
Vice-Reitora: Profa. Patricia Pranke
Pró-Reitor de Pós-Graduação: Prof. Celso Giannetti Loureiro Chaves
Diretora do Instituto de Informática: Profa. Carla Maria Dal Sasso Freitas
Coordenador do PGMICRO: Prof. Tiago Roberto Balen
Bibliotecário-chefe do Instituto de Informática: Alexsander Borges Ribeiro

Mel, I love you wholeheartedly. This is for you.

ABSTRACT

The dimensions of planar transistors were reduced until detrimental effects caused by the miniaturization of the transistor became significant. To address this issue, the microelectronics industry has changed the structure of the transistor from a planar to a multi-gate structure. A Monte Carlo device simulator is an efficient tool to predict and investigate the performance and reliability of transistors. This simulator employs a semiclassical theoretical model to describe the transport of charge carriers. Nevertheless, quantum corrections can be included in this simulator to take into consideration the impact of quantum effects on the electrical behavior of nanoscale transistors. This work proposes a quantum-corrected Monte Carlo device simulator for n-type FinFETs and n-type nanowire transistors. The quantum correction employed here is the Effective Potential approach, where the size of the electrons is no longer disregarded. Thus, space quantization effects such as quantum confinement can be modeled in the device simulator. We have developed a Schrödinger-Poisson solver and an Effective Potential-Poisson solver to extract the unique parameter of the Effective Potential of the transistors of interest. For the n-type FinFET, the Effective Potential parameter is equal to 0.45 nm, while for the n-type nanowire transistor, the Effective Potential parameter is equal to 0.4 nm. Comparing the results of these solvers, we can evaluate that the Effective Potential is a suitable quantum correction to simulate quantum confinement in three-dimensional devices. We have included the Effective Potential as a quantum correction to the Monte Carlo device simulator n-type FinFETs and n-type nanowire transistors. The n-type FinFET was simulated using semiclassical and quantum-corrected simulators. The results of both simulators were contrasted, and it was shown that the quantum-corrected simulator models volume inversion and the reduction of the electron density in the channel, which both are effects of quantum confinement. The nanowire transistor of interest was simulated using the quantum-corrected simulator, the transfer characteristic curve was compared to experimental results, demonstrating that our quantum-corrected simulator results agree very well with the experimental measurements.

Keywords: Monte Carlo device simulator. Quantum corrections. Effective Potential. FinFET. Nanowire transistor.

RESUMO

As dimensões dos transistores planares foram reduzidas até que efeitos indesejáveis causados pela miniaturização do transistor tornaram-se significativos. Para contornar esse problema, a indústria microeletrônica mudou a estrutura do transistor de uma estrutura planar para uma estrutura multiportas. Um simulador de dispositivos Monte Carlo é uma ferramenta eficiente para prever e investigar o desempenho e a confiabilidade de transistores. Este simulador utiliza um modelo teórico semiclássico para descrever o transporte de portadores de carga. No entanto, correções quânticas podem ser incluídas nesse simulador para considerar o impacto dos efeitos quânticos no comportamento elétrico de transistores em escala nanométrica. Neste trabalho, propomos um simulador de dispositivo Monte Carlo com correção quântica para FinFETs tipo-n e transistores nanofios tipo-n. A correção quântica empregada aqui é o Potencial Efetivo, onde o tamanho dos elétrons não é mais desconsiderado. Assim, efeitos de quantização espacial, como o confinamento quântico, podem ser modelados no simulador do dispositivo. Desenvolvemos um Schrödinger-Poisson *solver* e um Potencial Efetivo-Poisson *solver* para extrair o único parâmetro do Potencial Efetivo de ambos os transistores de interesse. Para o FinFET tipo-n, o parâmetro do Potencial Efetivo é igual a 0,45 nm, enquanto para o transistor de nanofios tipo-n, o parâmetro do Potencial Efetivo é igual a 0,4 nm. Comparando os resultados desses *solvers*, podemos avaliar que o Potencial Efetivo é uma correção quântica adequada para simular o confinamento quântico em dispositivos tridimensionais. Incluímos o Potencial Efetivo como correção quântica nos simuladores de dispositivo Monte Carlo dos transistores FinFET e nanofio tipo-n. O transistor FinFET tipo-n foi simulado usando o simulador semiclássicos e o simulador com correção quântica. Os resultados de ambos os simuladores foram contrastados, mostrando que o simulador com correção quântica modela *volume inversion* e a redução da densidade eletrônica no canal, os quais são efeitos do confinamento quântico. O transistor de nanofio de interesse foi simulado usando o simulador com correção quântica. A curva transferência desse transistor foi comparada com os resultados experimentais, demonstrando que os resultados do nosso simulador com correção quântica concordam muito bem com as medidas experimentais.

Palavras-chave: Simulador de dispositivos Monte Carlo. Correções quânticas. Potencial Efetivo. FinFET. Transistores de nanofio.

LIST OF ABBREVIATIONS AND ACRONYMS

1D	One Dimensional
2D	Two Dimensional
3D	Three Dimensional
BTE	Boltzmann Transport Equation
BTI	Bias Temperature Instability
CIC	Cloud-in-Cell
EMC	Ensemble Monte Carlo Simulation
EOT	Equivalent Oxide Thickness
FinFET	Fin Field Effect Transistor
IC	Integrated Circuit
MC	Monte Carlo Simulation
MOSFET	Metal-Oxide-Semiconductor Field-Effect Transistor
PETSc	Portable, Extensible Toolkit for Scientific Computation
RDF	Random Dopant Fluctuation
SIP	Strongly Implicit Procedure
SLEPc	Scalable Library for Eigenvalue Problem Computations
SOI	Silicon on Insulator

LIST OF SYMBOLS

$f(\mathbf{r},\mathbf{k},t)$	Electron distribution function
$\mathbf{r}$	Electron’s position in spherical coordinates
$\dot{\mathbf{r}}$	First derivative of electron’s position with respect to time
$\mathbf{k}$	Electron’s wavevector
$\dot{\mathbf{k}}$	First derivative of electron’s wavevector with respect to time
t	Time
∇_{r}	Laplacian in real space
∇_{k}	Laplacian in the reciprocal space
$S(\mathbf{k},\mathbf{k}')$	Transition rate out of $\mathbf{k}$ to $\mathbf{k}'$
$\mathbf{p}$	Free-electron momentum
$\mathbf{F}$	Electrostatic force
$\hbar$	Planck’s constant
q	Elementary charge
$\mathbf{v}$	Electron’s velocity
$E(\mathbf{k})$	Dispersion relation of the conduction band
$\mathbf{a}$	Acceleration
m_{eff}	Effective mass
m	Mass
x	Device’s length direction
y	Device’s height direction
z	Device’s width direction
x_i	position of the i-th electron along the device’s length direction
y_i	position of the i-th electron along the device’s height direction
z_i	position of the i-th electron along the device’s width direction
v_x	x component of electron’s velocity
v_y	y component of electron’s velocity
v_z	z component of electron’s velocity
k_x	x component of electron’s wavevector
k_y	y component of electron’s wavevector
k_z	z component of electron’s wavevector
E_x	x component of electric field

E_y	y component of electric field
E_z	z component of electric field
X	The symmetry point in the reciprocal space
Δ	The symmetry point in the reciprocal space
${m_x}^{\nu}$	Electron's effective mass in x direction of the ν-th valley pair
${m_y}^{\nu}$	Electron's effective mass in y direction of the ν-th valley pair
${m_z}^{\nu}$	Electron's effective mass in z direction of the ν-th valley pair
m_l	Electron's effective mas parallel to the ellipsoidal longest axis
m_t	Electron's effective mass in the cross-section perpendicular to the longest axis
m_0	Free-electron mass
k_i^*	Electron's wavevector in the Herring-vogt transformation along *i*-th direction
α	Nonparabolicity factor of the conduction band
$\mathrm{g}(k)$	Density of states in the reciprocal space
V_c	Crystal volume
$\mathrm{g}(E)$	Density of states per unit energy
H_T	Total Hamiltonian
H_e	Electron's Hamiltonian
$H_{crystal}$	Crystal Hamiltonian
H_i'	Hamiltonian of the *i*-th perturbation
c	Crystal eigenstate
$S_i(\mathbf{k},\mathrm{c};\mathbf{k}',\mathrm{c}')$	Transition rate out of $\lvert\mathbf{k},\mathrm{c}\rangle$ to $\lvert\mathbf{k}',\mathrm{c}'\rangle$
$E(\mathbf{k},c)$	Energy of the state $\lvert\mathbf{k},\mathrm{c}\rangle$
$\Gamma_i(E)$	Scattering rate out of the state E of the *i*-th scattering mechanism
k_B	Boltzmann constant
T	Temperature
Ξ	Acoustic deformation potential
ρ_{si}	Silicon density
u	Sound velocity
D_tK	Coupling constant of the optical phonon scattering,
Z	Number of available final valleys
ω_{op}	Optical phonon frequency
$n(\omega_{op})$	Optical phonon occupancy
$\hbar\omega_{op}$	Optical phonon energy

$\Gamma_j(E(t))$ Total scattering rate of the *j-th* mechanism at the time *t*

N_s Number of scattering mechanisms

$P(t)dt$ Probability that an electron that suffered a scattering at $t = 0$ and had a free-flight time equal to t will suffer a new scattering event between t and $t + dt$

t_r Free-flight time

r Probability that an electron has a free-flight time t_r

Γ_0 The maximum value that the total scattering can assume

$\Gamma_{self}(\mathrm{E})$ The scattering rate of the self-scattering mechanism

E_{in} Electron's initial energy

$rand0$ random number uniformly distributed between 0 to 1

$rand1$ random number uniformly distributed between 0 to 1

$rand2$ random number uniformly distributed between 0 to 1

$rand3$ random number uniformly distributed between 0 to 1

$rand4$ random number uniformly distributed between 0 to 1

ϕ Azimuthal angle

θ Polar angle

Δt Observation time

dte The time until the next scattering event

V Hartree potential

ρ Charge density

ε Material permittivity

X_i Mesh spacing along the x-direction of the mesh point i, j, k

Y_j Mesh spacing along the y-direction of the mesh point i, j, k

Z_k Mesh spacing along the x-direction of the mesh point i, j, k

p Hole's densities

n Electron's density

N_A Dopant densities of acceptor atoms

N_D Dopant densities of donor atoms

δ Small update in the Hartree potential

n_i Intrinsic carrier density

f Force function of Poisson's equation

N_V Effective density of states of the valence band

$F_{\frac{1}{2}}$ Fermi-Dirac integral of order ½

E_C	Conduction band level
E_i	Intrinsic Fermi level
E_g	Bandgap energy
$ch(i,j,k)$	Particle density at the mesh point i,j,k
$Q(i,j,k)$	Total charge attributed to the mesh point i,j,k
$vol(i,j,k)$	Volume associated to the mesh point i,j,k
F_i	Electrostatic force that acts upon the *i*-th electron
F^n	Electrostatic force associated to the mesh point *n*
w^n	Distance between the electron and the mesh point *n*
ω_p	Plasma frequency
ε_{si}	Permittivity of silicon
$\bar{V}$	Total potential of a system of electrons
$n(\mathbf{r})$	Local electron density
N_e	Number of electrons in a system of electrons
$n_i(\mathbf{r})$	Density of an electron
σ	Smoothing parameter of the Effective Potential
V_{eff}	Effective Potential
x_i	The position along the *x*-direction of the mesh point i,j,k
y_j	The position along the *y*-direction of the mesh point i,j,k
z_k	The position along the *z*-direction of the mesh point i,j,k
Δ_x	Distance between the mesh point i,j,k and its neighbor along the *x*-direction
Δ_y	Distance between the mesh point i,j,k and its neighbor along the *y*-direction
Δ_z	Distance between the mesh point i,j,k and its neighbor along the *z*-direction
N_x	Number of cells along *x*-direction employed to calculate the Effective Potential
N_y	Number of cells along *y*-direction employed to calculate the Effective Potential
N_z	Number of cells along *z*-direction employed to calculate the Effective Potential
$I^1_{i,j,k,l,m,n}$	Effective Potential coefficient
$I^2_{i,j,k,l,m,n}$	Effective Potential coefficient
$I^3_{i,j,k,l,m,n}$	Effective Potential coefficient
$I^4_{i,j,k,l,m,n}$	Effective Potential coefficient
H_o	One-electron Hamiltonian of the crystal
$U(x,y,z)$	Confinement potential

$\Psi(\mathrm{x,y,z})$	Wavefunction
$\varphi_{n,\mathbf{k}}(x,y,z)$	Bloch wavefunction
$E_m(\mathbf{k})$	Energy of the band m
$\psi(x,y,z)$	Envelope wavefunction
$E_C(y,z)$	Conduction band as a function of the device's height and width
$H_\parallel$	Hamiltonian parallel to the confinement
$H_\perp$	Hamiltonian perpendicular to the confinement
$\psi^{n,\nu}(y,z)$	Envelope wavefunction function of the n subband of the ν valley
$E^{n,\nu}$	Eigenvalue of the n subband of the ν valley
$\mathbf{\Omega}$	Control surface
$S_{y,i}$	Length of the *i-th* surface along the y direction
$S_{z,i}$	Length of the *i-th* surface along the z direction
A'	Area of the surface control $\mathbf{\Omega}$
$N^{n,\nu}$	Electron line density of the n subband of the ν valley pair
$g_{1\mathrm{D}}(E)$	1D density of states
$F_{-1/2}$	Fermi-Dirac integral of order -1/2
n_Q	Quantum electron density
χ^{si}	Silicon's electron affinity
N_c	Effective density of states of silicon conduction's band
$\chi^{j,k}$	Electron affinity at the mesh point j,k
$E_C - E_i$	Conduction band edge minus the intrinsic Fermi level of silicon

LIST OF FIGURES

Figure 2.1: Diagram of the relevant scattering mechanisms in silicon devices. 20

Figure 2.2: Flowchart of the scattering mechanism selection. 26

Figure 2.3: Flowchart of the Monte Carlo transport simulator. 27

Figure 2.4 Transport evolution in a Ensemble Monte Carlo simulation. The movement of electrons is evaluated at observation times Δt, the *j*-th observation time is represented by the *j*-th vertical line. The red squares represent random scattering events. The *i*-th horizontal lines represent the evolution of the trajectory of the i-th electron. 29

Figure 2.5: Diagram of the seven-point stencil employed to discretize the 3D Poisson's equation. The potential at the mesh point i, j, k (represented as a black circle) is calculated taking into account its six closest neighbors (represented as red circles). 31

Figure 2.6: The grid used to calculate the permittivity in green. The midpoints are at the center of the face of the green grid. 32

Figure 2.7: Flowchart of the Monte Carlo device simulator. 41

Figure 3.1: Diagram of the mesh cells that surround the mesh point i, j, k (in red). 50

Figure 4.1 – Cross-section of the FinFET device investigated in this work. The cross-section is along the height and the width of the transistor. The metal gate is represented in red; the silicon is represented in blue, and the dielectric is represented in gray. $Wfin$ and $Hfin$ represent the fin width and height respectively 56

Figure 4.2: Cross-section of the silicon nanowire transistor investigated in this work. The cross-section is along the height and the width of the transistor. The metal gate is represented in red; the silicon is represented in blue, and the dielectric and the buried oxide are represented in gray. $Wfin$ and $Hfin$ represent the fin width and height respectively 57

Figure 4.3: Five-point stencil used to discretize the Schrödinger equation. The volume control is represented by the dashed line square. This volume control is divided into four squares, each with a surface along the *y*-direction and *z*-direction. 60

Figure 4.4: Five-point stencil used to discretize the 2D Poisson's equation. Four control surfaces surround the control volume (in gray). 65

Figure 4.5: Flowchart of the Schrödinger-Poisson solver 70

Figure 4.6: Flowchart of the Effective Potential-Poisson solver. 72

Figure 4.7: Electron density calculated classically (using only Poisson solver). V_G = 1 V. 75

Figure 4.8: Electron density calculated using the 2D Effective Potential-Poisson solver. V_G = 1 V.... 75

Figure 4.9: Electron density calculated using the 2D Schrödinger-Poisson solver. V_G = 1 V. 76

Figure 4.10: Line density of the electrons in the FinFET as a function of the gate bias calculated using the semiclassical model (blue curve), the Effective Potential solver (red curve), and the Schrödinger-Poisson solver (black curve). 77

Figure 4.11: Line density of the electrons in the nanowire transistor as a function of the gate bias calculated using the semiclassical model (blue curve), the Effective Potential solver (red curve), and the Schrödinger-Poisson solver (black curve). 78

Figure 4.12: Potential energy calculated classically and by the Effective Potential-Poisson solver. Using V_G = 1 V. 78

Figure 5.1: Flowchart of the quantum-corrected MC device simulator. 80

Figure 6.1: Schematic of the FinFET investigated in this work. The silicon regions are in blue, the silicon oxide region in gray, and the gate dielectric in light gray. The gate metal is represented in red.

The region referred to as S represents the source, G represents the gate and D represents the drain. $Wfin$ and $Hfin$ represent the fin width and height respectively, and L represents the channel length.83

Figure 6.2: Cumulative charge as a function of the time through the source and drain contact with V_{DS}=1.0 V, V_{GS} = 0.8 V, and V_{BS} = 0 V. 84

Figure 6.3: Conduction band taken at the middle of the FinFET width calculated using the semiclassical simulator. V_{DS} = 0.2 V, V_{GS} = 0.8 V and V_{BS} = 0 V. 85

Figure 6.4: Conduction band taken at the middle of the FinFET width calculated using the quantum-corrected simulator. The circle in red indicates the region where the conduction band is smoothed. V_{DS} = 0.2 V, V_{GS} = 0.8 V and V_{BS} = 0 V. 85

Figure 6.5 Electron density taken at a cross-section in the channel region calculated using the semiclassical simulator. V_{DS} = 0.2 V, V_{GS} = 0.8 V and V_{BS} = 0 V. 86

Figure 6.6: Electron density taken at a cross-section in the channel region calculated using the quantum-corrected simulator. V_{DS} = 0.2 V, V_{GS} = 0.8 V and V_{BS} = 0 V. 86

Figure 6.7: Average surface roughness scattering events per electron crossing the channel in the semiclassical simulator (blue curve) and quantum-corrected simulator (red curve) for 10 samples. The error bars indicate 95% confidence interval. V_{DS} = 0.5 V, and V_{BS} = 0 V. 87

Figure 6.8: Average phonon scattering events per electron crossing the channel in the semiclassical simulator (blue curve) and quantum-corrected (red) simulators for 10 samples. The error bars indicate 95% confidence interval. V_{DS} = 0.5 V, and V_{BS} = 0 V. 88

Figure 6.9: Average electron velocity along the device length for 10 samples. Curves estimated by the semiclassical simulator are in blue, while curves estimated by the quantum-corrected simulator are in red. The error bars indicate 95% confidence interval. V_{BS} = 0 V, V_{DS} = 0.5 V, V_{GS} = 0.8 V. 89

Figure 6.10: Electron density along the device length for 10 samples. Curves estimated by the semiclassical simulator in blue, while curves estimated by the quantum-corrected simulator are in red. The error bars indicate 95% confidence interval. V_{BS} = 0 V, V_{DS} = 0.5 V, V_{GS} = 0.8 V. 89

Figure 6.11 Transfer characteristic curves estimated by the semiclassical (blue curve) and quantum-corrected (red) simulator. The curves represent the average value of the 10 samples. The error bars indicate 95% confidence interval. V_{BS} = 0 V, V_{DS} = 0.5 V. 90

Figure 6.12 Output curves estimated by the semiclassical (blue) and quantum-corrected (red) simulators. The curves represent the average value of the 10 samples. The error bars indicate 95% confidence interval. V_{BS} = 0 V, V_{GS} = 0.8V. 91

Figure 7.1: Schematic of the nanowire transistor investigated in this work. The silicon dioxide is represented in gray, the gate dielectric is represented in gray, the buried oxide is represented in light gray, and the silicon regions are represented in blue. The gate metal is represented in red. The region referred to as S represents the source, G represents the gate and D represents the drain. $Wfin$ and $Hfin$ represent the fin width and height respectively, and L represents the channel length. 92

Figure 7.2: Transfer characteristic curve estimated by the quantum-corrected simulator (red) and measured experimentally (black). The curves represent the average value of the 20 samples. The error bars indicate 95% confidence interval. V_{BS} = 0 V, V_{DS} = 0.7 V. 93

Figure 7.3: Transfer characteristic curves in log scale estimated by the quantum-corrected simulator (red) and measured experimentally (black). The curves represent the average value of the 20 samples. The error bars indicate 95% confidence interval. V_{BS} = 0 V, V_{DS} = 0.7 V. 93

Figure 7.4: Conduction band taken at the middle of the nanowire width calculated using the quantum-corrected simulator. The circles in red indicate the regions where the conduction band is smoothed. V_{DS} = 0.7 V, V_{GS} = 0.9 V and V_{BS} = 0 V. 94

Figure 7.5: Electron density taken at a cross-section in the channel region calculated by the quantum-corrected simulator results. V_{DS} = 0.7 V, V_{GS} = 0.9 V and V_{BS} = 0 V. 95

Figure 7.6: Phonon scattering events (green) and surface roughness scattering events (magenta) per electron crossing the channel in the quantum-corrected simulator. The curves represent the average value of the 20 samples. The error bars indicate 95% confidence interval. V_{DS}=0.7 V, and V_{BS} = 0 V. 95

Figure 7.7: Electron density along the channel length of the device without any dopant in the channel (black curve) and of the device with one dopant in the channel at x = 45 nm (red curve). The channel length of the nanowire transistor is 40 nm (from x = 34 nm to x = 74 nm). 97

Figure 7.8 Average velocity of electrons along the length of the device without any dopant in the channel (black curve) and of the device with one dopant in the channel at x = 45 nm (red curve). The channel length of the nanowire transistor is 40 nm (from x = 34 nm to x = 74 nm). The dashed lines represent the limits of the channel region. 97

LIST OF TABLES

Table 3.1: Results of the integrals of equations (3.25) and (3.26). 55

TABLE OF CONTENTS

ABSTRACT ... ii
RESUMO ... v
LIST OF ABBREVIATIONS AND ACRONYMS ... vi
LIST OF SYMBOLS ... vii
LIST OF FIGURES ... xii
LIST OF TABLES ... xv
TABLE OF CONTENTS ... xvi
1 INTRODUCTION ... 10
2 MONTE CARLO DEVICE SIMULATOR ... 13
2.1 Monte Carlo Transport Simulation ... 13
2.1.1 Simulation of the Free-Flight Movement ... 16
2.1.2 Effective Mass Approximation ... 18
2.1.3 Scattering and Scattering Rates ... 20
2.1.4 Generation of the Free-Flight Time ... 24
2.1.5 Simulation of a Scattering Event ... 25
2.1.6 Ensemble Monte Carlo Transport Simulation ... 27
2.2 3D Poisson’s Equation Solver ... 30
2.2.1 Charge Assignment ... 37
2.2.2 Electric Field and Electric Force Calculation ... 38
2.3 Boundary Conditions ... 39
2.4 Monte Carlo Device Simulator Flowchart ... 40
3 QUANTUM CORRECTION ... 46
3.1 Effective Potential Approach ... 47
3.2 Methodology to Speed up the Calculation of the Effective Potential ... 49
4 EXTRACTION OF THE SMOOTHING PARAMETERS OF THE EFFECTIVE POTENTIAL ... 56
4.1 2D Schrödinger-Poisson Solver ... 57
4.1.1 The 2D Schrödinger equation ... 58
4.1.2 The 2D Poisson solver ... 64
4.1.3 Solving Poisson and Schrödinger Equations Self-consistently ... 68
4.1.4 The Flowchart of a 2D Schrödinger-Poisson Solver ... 70
4.2 2D Effective Potential-Poisson solver ... 71
4.3 Results of the Effective Potential-Poisson Solver and Schrödinger-Poisson Solver ... 74
5 DEVICE SIMULATOR WITH EFFECTIVE POTENTIAL AS QUANTUM CORRECTION ... 80
6 RESULTS OF THE N-TYPE FINFET ... 83
7 RESULTS OF THE NANOWIRE TRANSISTOR ... 92
7.1 Random Dopant Fluctuation ... 96

8 CONCLUSIONS AND FUTURE WORK 99
9 REFERENCES... 101

1 INTRODUCTION

For the last six decades, the microelectronic industry has been following Moore's law (MOORE, 1965), which is based on doubling the number of transistors in Integrated Circuits (IC) about every two years to reduce the cost of chips while increasing their processing power. The rise in number of transistors per chip was possible by scaling down their dimensions following the scaling rules of MOSFET (DENNARD, 1974). However, it was observed that planar MOSFET with small channel lengths presents irregular electrical behavior in contrast to the electrical behavior of the long-channel ones (KHANNA, 2016). The impact of the small size of the transistor dimensions on the electrical behavior of the transistors is called short-channel effects. It was observed that changing the planar structure of the MOSFET to a three-dimensional one reduces the impact of short-channel effects (MENDIRATTA; TRIPATHI, 2020). Because of that, the microelectronic industry has been fabricating 3D MOSFET transistors (BOHR; MISTRY, 2011).

MOSFETs only perform well if some metrics that characterize their performance match the industry requirements (LUNDSTROM, 2016). Considering that, investigating the influence of physical parameters – the materials employed, the doping density, and the oxide thickness – on the transistor performance is relevant. The reliability of the transistor is another aspect that must be investigated. As the size of transistors reached the nanometer scale, the variability of their electrical properties became more relevant (VASILESKA; ASHRAF, 2015). This deviation of the electrical properties from the nominal values is caused by the imperfections inherent to the semiconductor fabrication process. For instance, random dopant fluctuation (RDF) and trap activity are factors responsible for reliability issues in transistors. The RDF is responsible for threshold voltage and drain current variations among devices fabricated on the same chip (VASILESKA; ASHRAF, 2015). Trap activity results in the bias temperature instability effect (BTI) which is responsible for reliability issues concerning the deterioration of the transistor current (GRASSER, 2014).

Device simulators can be an alternative methodology to electrically characterize transistors (VASILESKA; GOODNICK; KLIMECK, 2010). They can be classified in terms of the model used to represent the transport of carriers. Regarding the semiclassical description of the transport of carriers, the most relevant are the Drift-Diffusion, the Hydrodynamic, and the Monte Carlo simulators (VASILESKA; GOODNICK; KLIMECK, 2010). In the Drift-Diffusion and Hydrodynamic simulations, assumptions are made to describe the carrier

distribution function and solve the Boltzmann transport equation (BTE). Thus, the transport of carriers is modeled using analytical equations, while in the Monte Carlo model, no assumptions are made to describe the carriers' distribution function and the Boltzmann transport equation is solved by treating the carriers as particles and simulating their transport (JACOBONI, 1989). The Drift-Diffusion and hydrodynamic models fail to represent a couple of physical phenomena, for instance, velocity overshoot and ballistic transport (VASILESKA; GOODNICK; KLIMECK, 2010). Because of that, the Monte Carlo device simulator is more accurate than the Drift-Diffusion and hydrodynamic models. Monte Carlo device simulators can be employed to investigate the reliability and performance of planar transistors (ROSSETTO, 2018), (ROSSETTO; CAMARGO; BOTH; VASILESKA; WIRTH, 2020), (CAMARGO, 2016), (CAMARGO; ROSSETTO; VASILESKA; WIRTH, 2020) and tri-gate transistors (FURTADO; CAMARGO; VASILESKA; WIRTH, 2021), (FURTADO; CAMARGO; VASILESKA; WIRTH, 2022), (FURTADO; CAMARGO; VASILESKA; WIRTH, 2022).

In devices whose dimensions are on the nanometer scale, quantum effects are relevant. For instance, in n-type FinFET and n-type nanowire transistors, electrons are confined in two directions (COLINGE, 2008). The quantum confinement changes the density of states, thus reducing the electron density (HAN; WANG, 2013). Besides, the inversion layer is placed a few nanometers away from the Si/SiO_2 interface, resulting in the phenomenon called volume inversion (COLINGE; GREER, 2016). Therefore, quantum confinement impacts the electrical properties of these transistors. Hence, this quantum effect must be considered to adequately model the device's physics. In a Monte Carlo device simulator, the carriers are treated as semiclassical particles. However, a quantum correction can be incorporated into this simulator to take into consideration the role of quantum effects in the electrical behavior of FinFET and nanowire devices.

The Effective Potential approach is a quantum correction that was proposed by Ferry (2000). It accounts for the wave-like behavior of electrons by describing the electrons as non-zero-size particles, whose size is given by a Gaussian wave packet. The size of electrons is characterized by the standard deviation of the Gaussian wave packet, which in this work is referred to as the smoothing parameter of the Effective Potential. The mathematical expression of the Effective Potential incorporates the electron size. Hence, in the quantum-corrected Monte Carlo device simulator, the electrons can still be treated as zero-size particles that are exposed to the Effective Potential. Because of that, the Effective Potential approach can be straightforwardly employed as a quantum correction in Monte Carlo simulators. Previous works

have successfully incorporated the Effective Potential into the Monte Carlo simulators of planar silicon on insulator (SOI) devices (RAMEY; FERRY, 2002), (VASILESKA; 2002).

The goal of this work is to incorporate the Effective Potential approach as a quantum correction to the Monte Carlo device simulator of n-type FinFETs and n-type nanowire transistors. The semiclassical Monte Carlo device simulator of n-type FinFET was developed by Furtado (2021), and the Monte Carlo device simulator of n-type nanowire transistors was concluded in this work. The smoothing parameters of the Effective Potential of these two devices were obtained by adjusting them until the electron linear density calculated using the Effective Potential agreed with the one calculated by the Schrödinger equation. Thus, to include the Effective Potential as a quantum correction to the Monte Carlo device simulators of n-type FinFETs and n-type nanowire transistors, firstly, a 2D Schrödinger-Poisson solver and a 2D Effective Potential-Poisson solver for the cross-section of these two devices were developed. Therefore, in this work, six simulators were developed, namely: 2D Schrödinger-Poisson solvers and 2D Effective Potential-Poisson solvers for the cross-section of n-type FinFETs and n-type nanowire transistors, and a 3D quantum-corrected Monte Carlo device simulator of n-type FinFETs and a 3D quantum-corrected Monte Carlo device simulator of n-type nanowire transistors.

The organization of this work proceeds as follows: the Monte Carlo device simulator is explained in Chapter 2, where the two important modules of the Monte Carlo device simulator are explained in detail. In Chapter 0, the Effective Potential approach and the methodology used to implement the effective potential in the Monte Carlo device simulator are presented. In Chapter 4, the method used to obtain the smoothing parameter of the Effective Potential is explained. In Chapter 5, the quantum-corrected Monte Carlo device simulator is explained. In Chapter 6, the simulation results of the n-type FinFET employing the quantum-corrected and the semiclassical Monte Carlo device simulators are demonstrated and compared. In Chapter 7, the nanowire transistor is investigated using the quantum-corrected device simulator, and the characteristic curve obtained by the simulations is compared with experimental data. Finally, in Chapter 8, the conclusions of this work and suggestions for future work are presented.

2 MONTE CARLO DEVICE SIMULATOR

A Monte Carlo device simulator consists of a Monte Carlo transport simulator coupled to a Poisson's equation solver. In the Monte Carlo device simulator, the transport of carriers is simulated using a semiclassical theoretical model. The electric field responsible for accelerating the carriers in the Monte Carlo transport simulation is calculated by a Poisson's equation solver, while the charge density used to calculate the Hartree potential in this solver comes from the Monte Carlo transport simulator. Thus, the Monte Carlo transport simulator and Poisson's equation are solved self consistently.

Within the Monte Carlo device simulator, there are three types of charged particles, namely: dopant ions, electrons, and holes. The dopants are fixed particles; therefore, their density is constant over the entire simulation. The second type is the charge carriers responsible for carrying the current, which in n-type MOSFETs are the electrons. They can be located at any position in the device and their dynamics are simulated in the Monte Carlo transport simulation. To solve Poisson's equation, their density is calculated based on their distribution over the semiconductor. Taking into account that MOSFETs are unipolar devices, the third type of particle is the charged particle that does not carry current in the device, in n-type devices these particles are holes; thus, their transport is disregarded, and their density is calculated using the Hartree potential and assuming quasi-equilibrium condition.

In this Chapter, firstly, the Monte Carlo transport simulation is explained in Section 2.1. Then, in Section 2.2, the 3D Poisson's equation solver is described. In Section 2.3, the boundary conditions for the transport simulation and for Poisson's equation are presented. Finally, in Section 2.4, the flowchart of the device simulator is presented and the considerations that are necessary to couple the Monte Carlo transport simulator with Poisson's equation solver are discussed.

2.1 Monte Carlo Transport Simulation

The drift current in n-type MOSFETs is a result of the oriented movement of electrons due to an external electric field. Considering that describing the transport of electrons in a semiconductor device using quantum mechanics is too time and memory-consuming (VASILESKA; GOODNICK; KLIMECK, 2010), an alternative to that is using a semiclassical theoretical model to describe their transport. The semiclassical model generalizes the theory

employed to describe the transport of free electrons to describe the transport of electrons in a periodic potential. In this case, the electrons represent Bloch wave packets instead of plane waves.

Instead of tracking the state of each electron, in the semiclassical model, the goal is to find the electron distribution function $f(\mathbf{r},\mathbf{k},t)$, which gives the probability of finding an electron in a position **r** in real space, in the **k** state in reciprocal space at the time *t*. The Boltzmann Transport Equation (BTE) describes the semiclassical transport of electrons, expressing the variations the electron distribution function is subjected to. The BTE is shown in equation (2.1) (JACOBONI; LUGLI, 1989).

$$\frac{\partial f}{\partial \mathrm{t}} + \dot{\mathbf{r}} \cdot \nabla_{\mathrm{r}} f + \dot{\mathbf{k}} \cdot \nabla_{\mathrm{k}} f = \left.\frac{\partial f}{\partial \mathrm{t}}\right|_{\mathrm{scat}} \tag{2.1}$$

The first term on the left side of equation (2.1) describes the temporal variation of the distribution function, which is equal to zero in steady-state conditions (HAMAGUCHI, 2001). The second term in the left side of equation (2.1) $(\dot{\mathbf{r}} \cdot \nabla_{\mathrm{r}} f)$ is called diffusion term of the BTE. This term comes from the variation of the distribution function in the real space and is caused by temperature or charge carrier density gradients. The third term in the left side of equation (2.1) $(\dot{\mathbf{k}} \cdot \nabla_{\mathrm{k}} f)$ is the drift term of the BTE. It represents the variation of the distribution function in reciprocal space caused by an external electromagnetic field (VASILESKA; GOODNICK; KLIMECK, 2010). The term on the right side of equation (2.1) is the scattering term of the BTE. While moving in a semiconductor, electrons are subjected to interactions that are referred to as scatterings. The probability per unit of time that an electron in the state **k** transitions to the state $\mathbf{k}'$ due to a scattering event is given by the transition rate $S(\mathbf{k},\mathbf{k}')$, while $S(\mathbf{k}',\mathbf{k})$ represents the transition rate out of $\mathbf{k}'$ to the state **k**. The scattering term is the difference between electrons scattered in and out of the state **k** and is expressed as (JACOBONI, 2010):

$$\left.\frac{\partial f}{\partial \mathrm{t}}\right|_{\mathrm{scat}} = \frac{V_c}{(2\pi)^3}\int \left[f(\mathbf{k}')S(\mathbf{k}',\mathbf{k})\big(1-f(\mathbf{k})\big) - f(\mathbf{k})S(\mathbf{k},\mathbf{k}')\big(1-f(\mathbf{k}')\big)\right] \mathrm{d}\mathbf{k}' \tag{2.2}$$

The scatterings are treated as time-dependent perturbations; thus, Fermi's golden rule is employed to calculate the transition rates.

In summary, the BTE is an integro-differential equation and the electron's distribution function can be changed by an electromagnetic field, scattering events, and gradients of temperature and charge carrier density. Although approximations can be employed to

analytically solve the BTE, one can solve the BTE directly by simulating the electron movement.

The BTE can be directly solved using a Monte Carlo (MC) transport simulator (JACOBONI; LUGLI, 1989). In a Monte Carlo transport simulation, the dynamic of electrons is described as periods of free-flight – where the electrons are accelerated by the electric field – that are terminated by instantaneous scattering events. During the free-flight time, the electron wavevector is modified only by the electric field. In n-type channel transistors, the electric fields are the driving forces for the transport of electrons in the conduction band (KANO, 1998). In the Monte Carlo transport simulation, electrons are point-like particles that represent Bloch wave packets. Classical equations are employed to describe their dynamics; thus, the position and the momentum of the electrons are well-defined (VASILESKA; GOODNICK; KLIMECK, 2010). Scattering is treated as a perturbation that changes the trajectory of the electron and may change its energy. The scattering events may be caused by phonons, other carriers, and crystal defects (LUNDSTROM, 2000). The stochastic behavior of scattering events is simulated by generating random numbers that represent the scattering probability density, which is given by the scattering rates (JACOBONI; LUGLI, 1989).

In a Monte Carlo transport simulation, the time is discretized, while the real space and the reciprocal space are continuous. This means that the dynamic of electrons is evaluated at discrete periods of time called observation time or time step, while electrons can move everywhere in the semiconductor. The total simulation time depends on the time needed to reach a steady state, which is usually about a few picoseconds. At the end of the simulation, average values of interest can be estimated (VASILESKA; GOODNICK; KLIMECK, 2010). The Monte Carlo method can be employed to simulate the transport of a unique electron or the movement of an ensemble of electrons. To simulate n-type MOSFETs, the transport of an ensemble of electrons must be simulated.

The next sections explain the Monte Carlo transport simulator. The free-flight period is described in Section 2.1.1, while the dispersion relation of silicon's conduction band is explained in Section 2.1.2. In Section 2.1.3, the scattering mechanisms, the scattering rates, and the scattering table – which is a lookup table where the scattering rates are stored and accessed to select the scattering mechanism responsible for ending the free-flight period of the carriers – are explained. The generation of the free-flight time and the scattering event simulation are explained, respectively, in Sections 2.1.4 and 2.1.5. The flowchart of the Ensemble Monte Carlo transport simulation is described in Section 2.1.6.

2.1.1 Simulation of the Free-Flight Movement

The electron's dynamics during the free-flight period is described by semiclassical physics. In this approach, the electron is treated as a wave packet of Bloch wavefunctions, and its transport is modeled as the propagation of a Bloch wave packet.

The wavevector of the electron in a crystal ($\mathbf{k}$) is related to the free-electron momentum ($\mathbf{p}$) as (VASILESKA; GOODNICK; KLIMECK, 2010)

$$\mathbf{k} = \frac{\mathbf{p}}{\hbar} \tag{2.3}$$

The Bloch wave packet (electron) behaves as a classical particle with momentum $\hbar\mathbf{k}$. Thus, the force, which is the variation of momentum with respect to time, is expressed as

$$\mathbf{F} = \frac{d(\hbar\mathbf{k})}{dt}, \tag{2.4}$$

where the force **F** is the electrostatic force, which is defined as $\mathbf{F} = q\mathbf{E}$, in which **E** is the electric field and q is the elementary charge.

The group velocity of Bloch wave packet is given by (HAMAGUCHI, 2001).

$$\mathbf{v} = \frac{1}{\hbar}\frac{\partial E(\mathbf{k})}{\partial \mathbf{k}}, \tag{2.5}$$

where $E(\mathbf{k})$ is the dispersion relation of the conduction band when describing the transport of electrons.

The acceleration of the Bloch electron is given by (HAMAGUCHI, 2001).

$$\mathbf{a} = \frac{d}{dt}\left(\frac{1}{\hbar}\frac{\partial E(\mathbf{k})}{\partial \mathbf{k}}\right) = \frac{1}{\hbar}\frac{\partial^2 E(\mathbf{k})}{\partial \mathbf{k}^2}\left(\frac{d\mathbf{k}}{dt}\right) = \frac{1}{\hbar^2}\frac{\partial^2 E(\mathbf{k})}{\partial \mathbf{k}^2}\left(\hbar\frac{d\mathbf{k}}{dt}\right) \tag{2.6}$$

Substituting equation (2.4) into equation (2.6) results in

$$\mathbf{a} = \frac{1}{\hbar^2}\frac{\partial^2 E(\mathbf{k})}{\partial \mathbf{k}^2}\mathbf{F} \tag{2.7}$$

Using an analogy with Newton's second law ($F = ma$), the effective mass is given by

$$m_{eff} = \hbar^2 \left(\frac{\partial^2 E(\mathbf{k})}{\partial \mathbf{k}^2}\right)^{-1} \tag{2.8}$$

Thus, the acceleration can be rewritten as

$$\mathbf{a} = \frac{\mathbf{F}}{m_{eff}} \tag{2.9}$$

Hence, employing the effective mass approximation, the transport of electrons can be evaluated using the classical equations that describe the dynamics of macroscopic particles (VASILESKA; GOODNICK; KLIMECK, 2010). Therefore, to calculate the position of the i-th electron at a time t, the following equations are employed:

$$\begin{aligned} x_i(t) &= x_i(t-1) + v_x \Delta t \\ y_i(t) &= y_i(t-1) + v_y \Delta t \\ z_i(t) &= z_i(t-1) + v_z \Delta t \end{aligned} \tag{2.10}$$

where v_x, v_y, and v_z are, respectively, the components of the electron's velocity along the *x*, *y* and *z* directions. In the device referential, the *x*-direction corresponds to the device's length direction, the *y* direction corresponds to the device's height direction, and the *z* direction corresponds to the device's width direction.

To calculate the change in the electrons wavevector caused by the electric field, equation (2.4), which relates the time variation of the electrons wavevector ($\dot{\mathbf{k}}$) with the external electric field (**E**), must be evaluated. The new wavevector of the electron at a discrete time *t* is calculated using equation (2.11) (VASILESKA; GOODNICK; KLIMECK, 2010).

$$\begin{aligned} k_x(t) &= k_x(t-1) + \frac{qE_x}{\hbar} \Delta t \\ k_y(t) &= k_y(t-1) + \frac{qE_y}{\hbar} \Delta t \\ k_z(t) &= k_z(t-1) + \frac{qE_z}{\hbar} \Delta t \end{aligned} \tag{2.11}$$

In summary, equation (2.10) and equation (2.11) are employed to evaluate the trajectory of electrons during the free-flight period. Note that the dispersion relation of the conduction

band is needed to calculate the energy, the velocity (equation (2.5)), and, consequently, the position of electrons (equation (2.10)).

2.1.2 Effective Mass Approximation

In n-type silicon FinFET and nanowire transistors, the electrons are accelerated in the conduction band. The velocity of the Bloch wave packet is given by the gradient of the silicon conduction band. Therefore, when it comes to simulating the transport of electrons using the semiclassical model, to evaluate the velocity, energy, and position of electrons, the conduction band information is necessary. Besides, to calculate the scattering probabilities (discussed in Section 2.1.3), the density of states in energy is necessary. The velocity and density of states can be estimated by calculating the silicon full-band structure. Considering that the full-band structure calculation is a very time and memory-consuming method, an alternative method is describing the dispersion relation of the conduction band using an analytical expression in terms of the effective mass. Although the effective mass approach is an approximation, the silicon conduction band around the minima is adequately described by this approach (RODRÍGUEZ-BOLÍVAR, 2005; DEWEY; OSMAN, 1993). Thus, in this work, the dispersion relation of the silicon conduction band is described by the effective mass approximation.

The conduction-band minimum of silicon is located at the symmetry point Δ, which is 15% distant from the X point along the family <100> (GONZALEZ, 2001). Since this family has six equivalent directions, the silicon conduction band has six equivalent valleys. Due to the degeneracy, the conduction band can be described using a three-valley-pair model. In terms of the constant energy surfaces, the dispersion relation of the silicon conduction band is ellipsoidal (JACOBONI, 2010). Thus, the dispersion relation along the (100) direction can be expressed as

$$E(\mathbf{k}) = \frac{\hbar^2 k_x^2}{2{m_x}^{\nu}} + \frac{\hbar^2 k_y^2}{2{m_y}^{\nu}} + \frac{\hbar^2 k_z^2}{2{m_z}^{\nu}} \tag{2.12}$$

where ${m_x}^{\nu}$ is the effective mass in x direction of the ν-th valley pair, ${m_y}^{\nu}$ is the effective mass in y direction of the ν-th valley pair, ${m_z}^{\nu}$ is the effective mass in z direction of the ν-th valley pair. The effective mass parallel to the ellipsoidal longest axis is m_l, and the effective mass in the cross-section perpendicular to the longest axis is m_t. For silicon, m_l is equal to $0.92m_o$ and m_t is $0.19m_o$, where m_o is the mass of the free electron. Thus, the effective mass of the valley pair along the (100) direction is $m_x = m_l$, $m_y = m_t$ and $m_z = m_t$. The effective mass of the

valley pair along the (010) direction is $m_y = m_l$, $m_x = m_t$ and $m_z = m_t$. And for the valley pair along the (001) direction $m_z = m_l$, $m_x = m_t$ and $m_y = m_t$.

Therefore, there is a dispersion relation to each valley pair when describing the conduction band using the three-valley-pair model. This complicates the transport simulation. For instance, if the electric field is applied along the (100) direction, in two valley pairs the electrons will be accelerated in a direction perpendicular to the longest axis of the ellipsoidal, whereas in one valley pair the movement will be parallel to the longest axis. An alternative to that is employing the Herring-Vogt transformation (HERRING; VOGT, 1956) which transforms the ellipsoidal constant energy surfaces into spherical constant energy surfaces. This is achieved by changing the wavevector using (JACOBONI, 2010):

$$k_i^* = k_i \sqrt{\frac{m_0}{m_i}} \tag{2.13}$$

Thus, by employing the Herring-Vogt transformations, the resulting dispersion relation is

$$E(k) = \frac{\hbar^2 k^{*2}}{2m_0} \tag{2.14}$$

Distant from the conduction minimum, the energy is a nonparabolic function of the wavevector. Considering that, the relation dispersion can be represented as (VASILESKA; GOODNICK; KLIMECK, 2010)

$$E(k)(1 + \alpha E(k)) = \frac{\hbar^2 k^{*2}}{2m_0} \tag{2.15}$$

where α is the nonparabolicity factor of the conduction band of silicon (VASILESKA; GOODNICK; KLIMECK, 2010).

The number of states in a spherical shell of radius k and thickness dk is expressed by equation (2.16). It is equal to the density of states in the reciprocal space ($V_c/(2\pi)^3$) multiplied by the volume of the spherical shell in the reciprocal space, including spin degeneracy (VASILESKA; GOODNICK; KLIMECK, 2010).

$$g(k)dk = 2\frac{V_c}{(2\pi)^3} 4\pi k^2 dk \tag{2.16}$$

where V_c is the crystal volume. Equation (2.16) in the new k-space is given by

$$g(k^*)dk^* = \frac{V_c}{\pi^2}\sqrt{\frac{m_t^2 m_l}{{m_0}^3}}{k^*}^2 dk^* \tag{2.17}$$

The density of states in energy is obtained by changing the variables from k^* to E.

$$g(E)dE = \frac{V_c}{\pi^2}\frac{2^{3/2}\sqrt{m_t^2 m_l}\sqrt{E(\mathbf{k})(1+\alpha E(\mathbf{k}))}}{2\hbar^3}(1+2\alpha E(\mathbf{k})) \tag{2.18}$$

2.1.3 Scattering and Scattering Rates

In the Monte Carlo transport simulation, the electron free-flight period is interrupted by scattering events which can modify the energy and momentum of electrons, deviating its trajectory (VASILESKA; GOODNICK, 2006). A scattering event represents an interaction between an electron and a scattering center. While electrons are moving in silicon, they can interact with defects, other charge carriers, and lattice vibrations (phonons) (VASILESKA; GOODNICK, 2006). Figure 2.1 shows the scattering mechanisms considered in our device simulator of n-type silicon devices.

Figure 2.1: Diagram of the relevant scattering mechanisms in silicon devices.

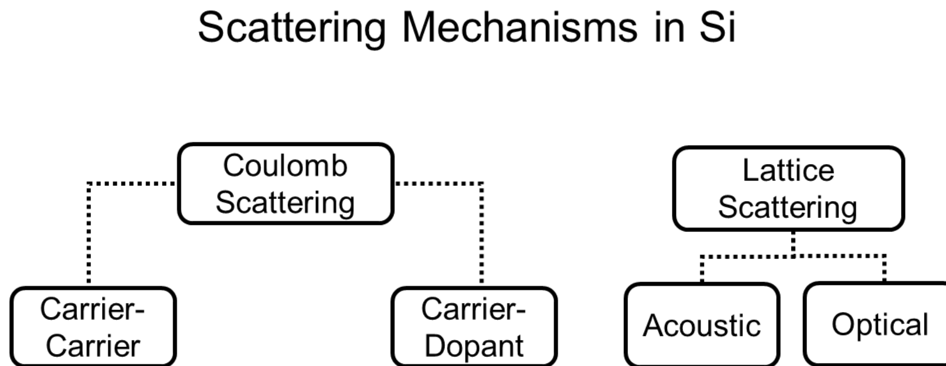

Source: Elaborated by the author.

As shown in Figure 2.1, the carrier-carrier and carrier-dopant scattering represent the electrostatic interaction that electrons face while moving in silicon. Additionally, electrons can interact with acoustic and optical phonons. Phonons are quantum particles that carry vibrational

energy generated by the vibrational movement of atoms with respect to their equilibrium position in the crystal lattice (SÓLYOM, 2007). The periodic potential of the crystal suffers variations due to the displacement of atoms from their equilibrium position. The electron-phonon scattering is described by this perturbation in the crystal potential. In terms of their vibrational mode, phonons can be acoustic when atoms move in phase, and optical when two adjacent atoms move out of phase (ASCHROFT, 1976). The displacement of each neighboring atom caused by optical phonon contributes directly to the lattice distortion since they move in opposite directions. However, in the acoustic phonon, neighboring atoms are dislocated from their equilibrium position in the same directions; hence, the strain created by the acoustic mode distorts the crystal lattice (VASILESKA; GOODNICK; KLIMECK, 2010; LUNDSTROM, 2000).

In the Monte Carlo transport simulation, a scattering can be modeled in the real space or the reciprocal space. For the device simulator, to simulate the transport of electrons in silicon, the Coulomb interactions are treated in real space. The Coulomb interaction between carrier-carrier and carrier-dopant is considered by the electrostatic force calculated from the Hartree potential, which is obtained by solving Poisson's equation.

The acoustic and optical phonon scatterings are described in the reciprocal space. Within this description, the scattering events are described, employing quantum mechanics, as time-independent perturbations. In the time-independent perturbation theory, when an electron transitions from a Bloch state to another one due to a perturbation, the total Hamiltonian of the system is described as

$$H_T = H_e + H_{crystal} + H_i' \tag{2.19}$$

Thus, the total Hamiltonian of a perturbed system is a sum of the Hamiltonian of the electron in the unperturbed crystal (H_e), the Hamiltonian of the crystal ($H_{crystal}$) and the Hamiltonian of the i-th perturbation (H_i') – which is the potential that describes the interaction between the electron and the particle that induces the scattering (phonon, defect, carrier). The first two are the unperturbed Hamiltonian, which eigenstates are **k** and c.

Scattering mechanisms can be classified by the final energy state of the electron after a scattering event. When the energy of an electron changes after a scattering event, the scattering is said to be inelastic. On the other hand, when the energy remains the same, the scattering is said to be elastic. The scattering mechanisms can also be divided into intravalley and intervalley. When the first occurs, the initial and final state are in the same valley, whereas in

intervalley transitions the initial and final state are in different valleys (VASILESKA; GOODNICK; KLIMECK, 2010).

For each scattering mechanism, there is a transition rate, which is the probability per unit of time that an electron in a state $|\mathbf{k}, \mathrm{c}\rangle$ transitions to an empty state $|\mathbf{k}', \mathrm{c}'\rangle$ after being scattered by the scattering process. The transition rate from a state $|\mathbf{k}, \mathrm{c}\rangle$ to a final state $|\mathbf{k}', \mathrm{c}'\rangle$ can be evaluated by using Fermi's Golden rule. Equation (2.20) expresses the transition rate of the ith scattering process out of state $|\mathbf{k}, \mathrm{c}\rangle$ to a final state $|\mathbf{k}', \mathrm{c}'\rangle$ (JACOBONI, 2010).

$$S_i(\mathbf{k}, \mathrm{c}; \mathbf{k}', \mathrm{c}') = \frac{2\pi}{\hbar} |\langle \mathbf{k}', c' | H_i' | \mathbf{k}, c\rangle|^2 \delta(E(\mathbf{k}', c') - E(\mathbf{k}, c)) \tag{2.20}$$

In equation (2.20), $\langle \mathbf{k}', c' | H_i' | \mathbf{k}, c\rangle$ is the matrix element of the i-th scattering mechanism, $E(\mathbf{k}, c)$ is the energy of the unperturbed state $|\mathbf{k}, \mathrm{c}\rangle$ and $E(\mathbf{k}', \mathrm{c}')$ is the energy of the perturbed state $|\mathbf{k}', \mathrm{c}'\rangle$.

The scattering rate out of the state **k** of the i-th scattering mechanism is obtained by summing the transition rate equation (2.20) over the available states $\mathbf{k}'$ in the final valley. It is given by

$$\Gamma_j(\mathbf{k}) = S_i(\mathbf{k}, \mathrm{c}; \mathbf{k}', \mathrm{c}') \frac{g(k')d\mathrm{k}'}{2} \tag{2.21}$$

Where $g(k')dk'$ is the number of available states in a sphere of radius k' and thickness dk' and $g(k')$ is the density of states (see equation (2.17)).

The variable k' in equation (2.21) can be changed to $E(k')$ using equation (2.18). The scattering rate out of the state E of the ith mechanism is given by equation (2.22).

$$\Gamma_i(E) = S_i(\mathbf{k}, \mathrm{c}; \mathbf{k}', \mathrm{c}') \frac{g(E')dE'}{2} \tag{2.22}$$

In the transport simulation of electrons in silicon, the acoustic phonon scattering is modeled as elastic and intravalley scattering. By assuming that the acoustic phonon scattering is elastic, the phonon population is estimated using equipartition approximation. Besides, the absorption and emission acoustic phonon scattering results in the same final state; thus, there is no difference between them. The acoustic phonon scattering rate is given by equation (2.23) (VASILESKA; GOODNICK; KLIMECK, 2010).

$$\Gamma(E(\mathbf{k})) = \frac{2k_B T}{\hbar u^2 \rho_{si}} \Xi^2 \frac{2^{3/2}\sqrt{m_t^2 m_l}\sqrt{E(\mathbf{k}')(1+\alpha E(\mathbf{k}'))}}{4\pi\hbar^3}(1+2\alpha E(\mathbf{k}')) \tag{2.23}$$

Where Ξ is the acoustic deformation potential, u is the sound velocity, ρ_{si} is the silicon density, k_B is the Boltzmann constant and T is the temperature.

The optical phonon scattering is inelastic, resulting in the emission or absorption of an optical phonon, and it can be intervalley and intravalley. To simulate intervalley scattering, the six degenerated valleys of the silicon conduction band along (100) directions must be considered. A scattering that causes a transition between valleys along the same orientation is called g-process scattering, while a scattering that causes a transition between valleys along distinct orientation is called f-process (VASILESKA; GOODNICK; KLIMECK, 2010). Thus, for the g-process, the number of final valleys for electrons to scatter into is equal to 1, whereas for the f-process, the number of final valleys for electrons to scatter into is equal to 4. To calculate the scattering rate of these two processes, the number of available final valleys is taken into account. Therefore, the f-process is more likely to occur. The optical phonon scattering rate is given by (VASILESKA; GOODNICK; KLIMECK, 2010):

$$\Gamma(E) = Z\frac{\pi(D_t K)^2}{\rho_{si}\omega_{op}}\left[n(\omega_{op}) + \frac{1}{2} \mp \frac{1}{2}\right]\frac{2^{3/2}\sqrt{m_t^2 m_l}\sqrt{E(\mathbf{k}')(1+\alpha E(\mathbf{k}'))}}{4\pi^2\hbar^3}(1+2\alpha E(\mathbf{k}')) \tag{2.24}$$

Where $D_t K$ is the coupling constant of the optical phonon scattering, Z in the number of available final valleys (which is equal to 4 for f-process and 1 for g-process), and ω_{op} is the optical phonon frequency, and $n(\omega_{op})$ is the phonon population, which is calculated using Bose–Einstein distribution function. The top sign in equation (2.24) corresponds to the phonon absorption process, while the bottom one corresponds to the phonon emission process. To assure energy conservation, the energy term in equation (2.24) is given by

$$E(\mathbf{k}') = E(\mathbf{k}) \pm \hbar\omega_{op} \tag{2.25}$$

Where $\hbar\omega_{op}$ is the optical phonon energy, and the top sign corresponds to the phonon absorption process, while the bottom one corresponds to the emission process.

2.1.4 Generation of the Free-Flight Time

The free-flight time is assigned to each electron based on the density probability of an electron being scattered around a time t and $t + dt$ after having a free-flight period equal to t. To obtain this density probability, first, the total scattering rate out of E in at the time t ($\Gamma(E(t))$) must be calculated. The total scattering rate is given by

$$\Gamma\big(E(t)\big) = \sum_{j}^{N_S} \Gamma_j(E(t)) \tag{2.26}$$

Where N_s is the number of scattering mechanisms, and $\Gamma_j(E(t))$ is the total scattering rate of the *j-th* mechanism at the time *t*, which can be calculated using equation (2.22).

The total scattering rate is the probability per unit of time that an electron will transit out of the state *E*. Thus, $\Gamma(E(t))dt$ is the probability that a scattering event will occur in an interval of time *dt* around *t*, whereas the probability that an electron that suffered a scattering at $t = 0$ is not scattered during an interval of time t is exp $(-\int_0^t \Gamma(E(t))dt')$. Therefore, the probability that an electron that suffered a scattering at $t = 0$ and had a free-flight time equal to t will suffer a new scattering event between t and $t + dt$ is (LUNDSTROM, 2000)

$$P(t)dt = \Gamma(E(t))\mathrm{exp}\left[-\int_0^t \Gamma(E(t))dt'\right]dt \tag{2.27}$$

The probability that an electron has a free-flight time t_r is given by integrating $P(t)dt$ from zero to t_r.

$$r = \int_0^{t_r} P(t)dt \tag{2.28}$$

Solving equation (2.28) after substituting equation (2.27) on equation (2.28) leads to equation (2.29).

$$r = 1 - exp\left[-\int_0^{t_r} \Gamma(E(t))dt'\right] \tag{2.29}$$

Equation (2.29) can be rewritten by substituting the term $1 - r$ for r, since they have the same probability distribution, thus are statistically the same (YORSTON, 1986). Assuming this, equation (2.29) results in equation (2.30).

$$\ln(r) = \int_0^{t_r} \Gamma(E(t))dt' \qquad (2.30)$$

Equation (2.30) can be solved to obtain the free-flight time t_r after each scattering event. However, equation (2.30) is too time-consuming to be solved analytically. Therefore, the self-scattering approximation is used to keep $\Gamma(E(t))$ constant. In this approximation, a fictitious scattering called self-scattering is included in the simulation, which has no impact on the trajectory and energy of the electron. The only consequence of adding the self-scattering is keeping the total scattering rate constant. This is made by calculating the maximum value that the total scattering can assume (Γ_0). Thus, the scattering rate of the fictious scattering mechanism $\Gamma_{self}(\mathrm{E})$ is given by (VASILESKA; GOODNICK; KLIMECK, 2010)

$$\Gamma_{self}(\mathrm{E}) = \Gamma_0 - \Gamma(\mathrm{E}) \qquad (2.31)$$

Using the self-scattering approximation, the total scattering rate is constant and equal to Γ_0. Thus, the integral of equation (2.30) can be easily solved, and the free-flight time can be written as

$$t_r = -\frac{1}{\Gamma_0}\ln(r) \qquad (2.32)$$

The free-flight time (t_r) is calculated using the expression given by equation (2.32). A random number (*rand0*) that varies from 0 to 1 is generated in the Monte Carlo code to represent r, which is the probability of a scattering occurring after some time t_r .

2.1.5 Simulation of a Scattering Event

Since each scattering mechanism has a different impact on the electron trajectory, as the free-flight ends, the next step is selecting the scattering mechanism that will scatter the electron, so the final state can be updated. To define which scattering mechanism is responsible for ending the free-flight period, a random number is generated *rand1*, which represents the total scattering rate.

In the simulation, the scattering rate of all mechanisms (including the self-scattering) as a function of the electron energy is calculated for an extended range of energy, Then, the scattering rates are normalized by this maximum value. Afterward, the cumulative scattering

rates are saved in a table, called the scattering table. In the scattering table, each line represents an energy level, and, in each row, the cumulative scattering rate is saved. For instance, in the first row, the normalized scattering rate of the first scattering mechanism is saved, in the second row the sum of the normalized scattering rate of the first scattering mechanism and the normalized scattering rate of the second scattering mechanism is saved. This goes on until the N_s-*th* row. In the $(N_s + 1)$-th row the complementary of the sum of the normalized scattering rates of the N_s scattering mechanism, which represents the self-scattering rate, is saved.

The method used to select the scattering mechanism responsible for ending the free-flight time of an electron is based on generating a random number evenly distributed between 0 and 1. The mechanism that will scatter the electron that has an energy E is stochastically chosen by comparing the generated random number with the probabilities on the scattering table for that specific electron energy, E. The selection process consists of finding the line in the scattering table that represents the electron energy, then, comparing the random number generated with the cumulative scattering rates that are stored in the following columns. If the random number is smaller than the value in the first column, the first mechanism is chosen. If the random number is greater than that, then, it is compared with the value on the second column. If the random number is smaller than the second column value, the second mechanism is chosen. If the random number is greater than the second column value, the analysis goes on until a mechanism is selected. The energy and the wavevector of the electron are updated in accordance with the selected scattering mechanism. The flowchart of the scattering mechanism selection process is shown is shown in Figure 2.3.

Figure 2.2: Flowchart of the scattering mechanism selection.

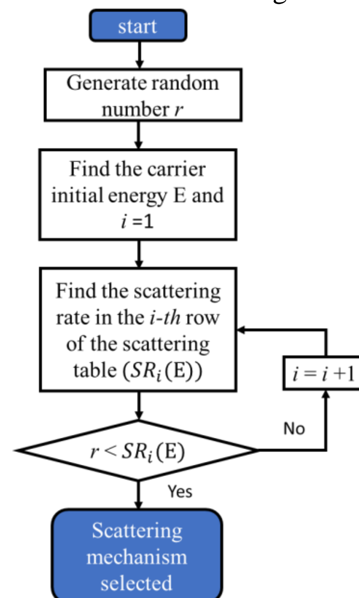

Source: Elaborated by the author.

2.1.6 Ensemble Monte Carlo Transport Simulation

The flowchart of an Ensemble Monte Carlo (EMC) transport simulation is shown in Figure 2.3. The simulation consists of initializing the conditions of the simulation, then creating the scattering tables, and initializing the electrons. Finally, the transport of the ensemble is simulated in a loop, where the free-flight period and scattering events take place. The simulation ends when the last time is reached.

Initialization of parameters

As the simulation starts, values are assigned to the variables that describe the conditions of the simulation – for example, temperature, maximum simulation time, materials properties, and observation time. These parameters are read in an input file; therefore, they can be easily modified by the user.

Figure 2.3: Flowchart of the Monte Carlo transport simulator.

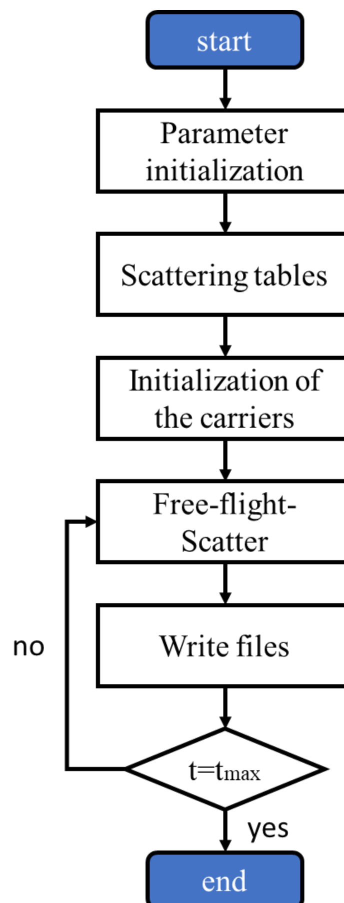

Source: Elaborated by the author.

Scattering tables

Next, the total scattering rate of all mechanisms is calculated as a function of the electron energy. Then the scattering rates are stored in the scattering table.

Initialization of electrons

After the scattering tables are generated, the electron initialization is performed. Each electron is initialized with energy, wavevector, and initial free-flight time.

The initial energy of the ensemble is given by the Boltzmann distribution. To randomize the initial energy of the electron, the initial energy is calculated by

$$E_{in} = -\frac{3}{2}k_B T \ln(rand2) \tag{2.33}$$

where *rand2* is a random number uniformly distributed between 0 and 1.

The dispersion relation of the conduction band relates the initial energy of the electron with the magnitude of the initial wavevector. The orientation of the wavevector is randomly assigned to the electrons, following equations (2.34).

$$\begin{aligned} \phi &= 2\pi(rand3) \\ cos\theta &= 1 - 2(rand4) \end{aligned} \tag{2.34}$$

In equation (2.34), *rand3* and *rand4* are random numbers uniformly distributed between 0 and 1, ϕ is the azimuthal angle that can vary from 0 to 2π, and θ is the polar angle which can vary from 0 to π. Then, the components k_x, k_y and k_z of the wavevector can be calculated.

Transport loop

In the transport loop, the trajectory of electrons is evolved until the final time is reached. Figure 2.4 represents the time evolution of an EMC simulation. The evolution of the trajectory of the i-th electron is represented by the i-th solid line. As mentioned in Section 2.1.1, the time evolution of the electron transport is divided into small intervals of time (observation time) where the movement of electrons is updated. In Figure 2.4, the red squares represent a scattering event, while the dotted vertical lines represent an observation time. As can be seen in Figure 2.4, the scattering event may coincide with an observation time, may occur before an observation time, may not occur between two consecutive observation times, besides, more than one scattering may occur during a unique observation time.

Figure 2.4 Transport evolution in a Ensemble Monte Carlo simulation. The movement of electrons is evaluated at observation times Δt, the *j*-th observation time is represented by the *j*-th vertical line. The red squares represent random scattering events. The i-th horizontal lines represent the evolution of the trajectory of the i-th electron.

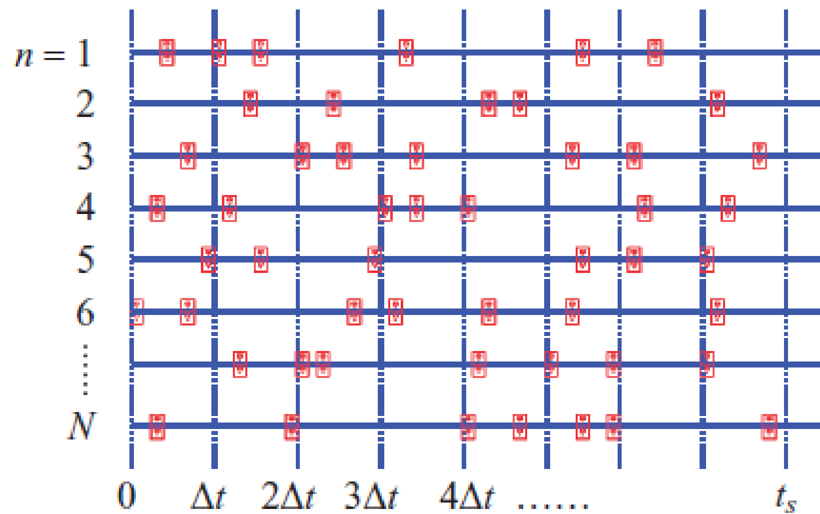

Source: Obtained from Vasileska and Goodnick (2006).

To simulate all these possibilities, the variables Δt (an observation time) and dte (the time until the next scattering event) are employed in the code. At an observation time, the time until the next scattering event (dte) of each electron is compared with the observation time. There are two possibilities, dte may be greater than Δt or smaller than Δt.

dte is larger than Δt: the electron is not scattered during Δt. The electron is accelerated by the electric field, changing the wavevector of the electron. The new wavevector is calculated, and the energy of the electron is calculated using the dispersion relation of the conduction band. The trajectory of the electron is updated, then the code tracks the next electron.

dte is smaller than Δt: a scattering event occurs before the next observation time. The electron is accelerated by the electric field in an interval of time equal to dte and then it is scattered by the chosen mechanism. The type of scattering that will deviate the trajectory of the i-th electron is chosen based on its energy at dte. The energy and the wavevector of the electron are updated based on the scattering mechanism chosen, and a new free-flight time is assigned to the electron. The new free-flight time is compared with the time left until the next observation time.

- the new free-flight time is smaller than the time left until the next observation time: another scattering event occurs before the next observation time. The electron is accelerated by the electric field in an interval of time equal to the new free-flight time, and the energy and

wavevector are updated. Then a scattering event is simulated again, the electron is scattered by the chosen mechanism, then energy and the wavevector of the electron are updated and a new free-flight time is assigned to the electron.

- the new free-flight time is greater than the time left until the next observation time: the electron is not scattered. The electron is accelerated by the electric field during the time left until the next Δt, and its wavevector and energy are updated. Then, the code tracks the next electron.

2.2 3D Poisson's Equation Solver

The electrostatic potential, or Hartree potential, in a MOSFET is controlled by the bias applied to its terminals and is related to the charge density in the device. The electrostatic potential is calculated by solving Poisson's equation, which comes from Gauss's law and is expressed in equation (2.35) as a Partial Differential Equation.

$$\nabla \cdot \left(\varepsilon(x,y,z)\nabla \mathrm{V}(x,y,z)\right) = -\rho(x,y,z), \quad (2.35)$$

where $V(x,y,z)$ is the three-dimensional Hartree potential, $\rho(x,y,z)$ is the charge density, and $\varepsilon(x,y,z)$ is the material permittivity at the coordinates *x*,*y* and *z*. Note that ε spatially varies due to the presence of different materials in MOSFET structures.

Poisson's equation must be discretized and linearized to be numerically solved (VASILESKA; GOODNICK; KLIMECK, 2010; JACOBONI, 2010). Thus, the first step is describing the device as a set of small three-dimensional cells that form a mesh. The position of each mesh node is fixed, and the mesh spacing, which is the distance between two consecutive mesh nodes, can be uniform or nonuniform in all three dimensions. Thus, the mesh nodes of the device are the discrete points where Poisson's equation is solved. The mesh point i,j,k, where Poisson's equation is solved, and its neighborhood is represented using a seven-point stencil represented in Figure 2.5.

Poisson's equation showed in equation (2.35) can be rewritten as

$$\frac{\partial}{\partial x}\left(\varepsilon\frac{\partial}{\partial x}V(x,y,z)\right) + \frac{\partial}{\partial y}\left(\varepsilon\frac{\partial}{\partial y}V(x,y,z)\right) + \frac{\partial}{\partial z}\left(\varepsilon\frac{\partial}{\partial z}V(x,y,z)\right) = \rho(x,y,z) \quad (2.36)$$

Figure 2.5: Diagram of the seven-point stencil employed to discretize the 3D Poisson's equation. The potential at the mesh point i, j, k (represented as a black circle) is calculated taking into account its six closest neighbors (represented as red circles).

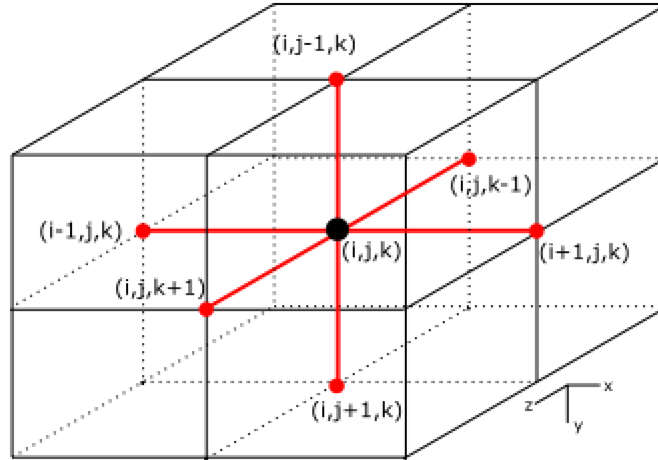

Source: Elaborated by the author.

To calculate equation (2.36) at the mesh point i, j, k, the left-hand side of equation (2.36) is discretized using the central finite difference method. Applying the central difference method to discretize the first term of the left-hand side of equation (2.36), which is the derivative with respect to the *x*-direction, results in

$$\frac{\partial}{\partial x}\left(\varepsilon \frac{\partial}{\partial x} V(x, y, z)\right) = \frac{\left(\varepsilon \frac{\partial V}{\partial x}\right)_{i+1/2,j,k} - \left(\varepsilon \frac{\partial V}{\partial x}\right)_{i-1/2,j,k}}{0.5(X_i + X_{i-1})} \tag{2.37}$$

The second derivative of the potential with respect to *x* at the point i, j, k is the discrete derivative of the first derivative. In equation (2.37), X_i is the mesh spacing along the *x*-direction of the point i, j, k. The index of the first derivatives in the numerator of equation (2.37) indicates that they are evaluated at the midpoints of the grid along the *x*-direction. This means that the point $i + 1/2\,, j, k$ is the midpoint between i, j, k and its neighbor at the right side along the *x*-direction $i + 1, j, k$, while the point $i - 1/2\,, j, k$ is the midpoint between i, j, k and its neighbor at the left side along the *x*-direction $i - 1, j, k$.

The discrete first derivative of the potential evaluated at the midpoints of the mesh along the *x*-direction is

$$\left(\frac{\partial V}{\partial x}\right)_{i+1/2,j,k} = \frac{V_{i+1,j,k} - V_{i,j,k}}{X_i} \tag{2.38}$$

$$\left(\frac{\partial V}{\partial x}\right)_{i-1/2,j,k} = \frac{V_{i,j,k} - V_{i-1,j,k}}{X_{i-1}} \tag{2.39}$$

where $V_{i+1,j,k}$ and $V_{i-1,j,k}$ are respectively the potential at the point $i+1, j, k$ and $i-1, j, k$. Note that these two points are the neighbors of the point i, j, k along the x-direction.

Figure 2.6: The grid used to calculate the permittivity in green. The midpoints are at the center of the face of the green grid.

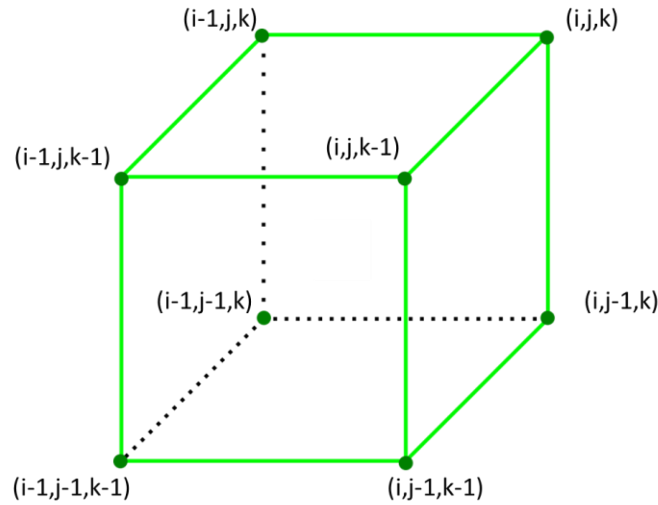

Source: Elaborated by the author.

To calculate ε at the midpoints, in equation (2.37), a different grid is used, which is shown in Figure 2.6. The mesh points of this new grid are represented by green circles. In this new representation, the point i, j, k (where the Poisson's equation is solved) is at the center of the cube. The midpoints (where ε is evaluated) coincide with the center faces of the cell. Thus, the permittivity at the midpoints is defined as

$$\varepsilon_{i+1/2,j,k} = \frac{\varepsilon_{i,j,k} + \varepsilon_{i,j,k-1} + \varepsilon_{i,j-1,k} + \varepsilon_{i,j-1,k-1}}{4} \tag{2.40}$$

$$\varepsilon_{i-1/2,j,k} = \frac{\varepsilon_{i-1,j,k-1} + \varepsilon_{i-1,j,k} + \varepsilon_{i-1,j-1,k-1} + \varepsilon_{i-1,j-1,k}}{4} \tag{2.41}$$

Substituting equations (2.38), (2.39), (2.40) and (2.41) into equation (2.37) results in

$$\frac{\partial}{\partial x}\varepsilon\frac{\partial}{\partial x}\mathrm{V} = \frac{\varepsilon_{i,j,k} + \varepsilon_{i,j,k-1} + \varepsilon_{i,j-1,k} + \varepsilon_{i,j-1,k-1}\left(V_{i+1,j,k} - V_{i,j,k}\right)}{2(X_i + X_{i-1})X_i} - \frac{\varepsilon_{i-1,j,k-1} + \varepsilon_{i-1,j,k} + \varepsilon_{i-1,j-1,k-1} + \varepsilon_{i-1,j-1,k}\left(V_{i,j,k} - V_{i-1,j,k}\right)}{2(X_i + X_{i-1})X_{i-1}} \tag{2.42}$$

The same discretization process is followed to discretize the second and third term of the right-hand side of Poisson's equation (equation (2.36)), which are the derivatives with respect to the *y*- and *z*-direction, respectively. This results in

$$\frac{\partial}{\partial y}\varepsilon\frac{\partial}{\partial y}V = \frac{\varepsilon_{i-1,j,k} + \varepsilon_{i,j,k} + \varepsilon_{i,j,k-1} + \varepsilon_{i-1,j,k-1}\left(V_{i,j+1,k} - V_{i,j,k}\right)}{2(Y_j + Y_{j-1})Y_j} - \frac{\varepsilon_{i-1,j-1,k-1} + \varepsilon_{i,j-1,k-1} + \varepsilon_{i,j-1,k} + \varepsilon_{i-1,j-1,k}\left(V_{i,j,k} - V_{i,j-1,k}\right)}{2(Y_j + Y_{j-1})Y_{j-1}} \tag{2.43}$$

$$\frac{\partial}{\partial z}\varepsilon\frac{\partial}{\partial z}V = \frac{\varepsilon_{i-1,j,k} + \varepsilon_{i,j,k} + \varepsilon_{i,j-1,k} + \varepsilon_{i-1,j-1,k}\left(V_{i,j,k+1} - V_{i,j,k}\right)}{2(Z_k + Z_{k-1})Z_k} - \frac{\varepsilon_{i-1,j,k-1} + \varepsilon_{i,j,k-1} + \varepsilon_{i-1,j-1,k-1} + \varepsilon_{i,j-1,k-1}\left(V_{i,j,k} - V_{i,j,k-1}\right)}{2(Z_k + Z_{k-1})Z_{k-1}} \tag{2.44}$$

Substituting equations (2.42), (2.43), and (2.44) into the left-hand side of Poisson's equation (equation (2.36)) and rearranging the expressions that multiply the potential terms to describe them as coefficients, results in

$$\nabla\cdot\left(\varepsilon\nabla\mathrm{V}(x,y,z)\right) = B_{i,j,k}V_{i,j,k-1} + C_{i,j,k}V_{i,j-1,k} + D_{i,j,k}V_{i-1,j,k} + E_{i,j,k}V_{i,j,k} + F_{i,j,k}V_{i+1,j,k} + G_{i,j,k}V_{i,j+1k} + H_{i,j,k}V_{i,j,k+1} \tag{2.45}$$

Where

$$B_{i,j,k} = \frac{\varepsilon_{i-1,j,k-1} + \varepsilon_{i,j,k-1} + \varepsilon_{i-1,j-1,k-1} + \varepsilon_{i,j-1,k-1}}{2(Z_k + Z_{k-1})Z_{k-1}}$$

$$C_{i,j,k} = \frac{\varepsilon_{i-1,j-1,k-1} + \varepsilon_{i,j-1,k-1} + \varepsilon_{i,j-1,k} + \varepsilon_{i-1,j-1,k}}{2(Y_j + Y_{j-1})Y_{j-1}} \tag{2.46}$$

$$D_{i,j,k} = \frac{\varepsilon_{i-1,j,k-1} + \varepsilon_{i-1,j,k} + \varepsilon_{i-1,j-1,k-1} + \varepsilon_{i-1,j-1,k}}{2(X_i + X_{i-1})X_{i-1}}$$

$$F_{i,j,k} = \frac{\varepsilon_{i,j,k} + \varepsilon_{i,j,k-1} + \varepsilon_{i,j-1,k} + \varepsilon_{i,j-1,k-1}}{2(X_i + X_{i-1})X_i}$$

$$G_{i,j,k} = \frac{\varepsilon_{i-1,j,k} + \varepsilon_{i,j,k} + \varepsilon_{i,j,k-1} + \varepsilon_{i-1,j,k-1}}{2(Y_j + Y_{j-1})Y_j}$$

$$H_{i,j,k} = \frac{\varepsilon_{i-1,j,k} + \varepsilon_{i,j,k} + \varepsilon_{i,j-1,k} + \varepsilon_{i-1,j-1,k}}{2(Z_k + Z_{k-1})Z_k}$$

$$E_{i,j,k} = -B_{i,j,k} - C_{i,j,k} - D_{i,j,k} - F_{i,j,k} - G_{i,j,k} - H_{i,j,k}$$

In addition to discretizing the left-hand side of Poisson's equation, we must linearize the right-hand side of Poisson's equation. In semiconductors, the charge density is a sum of the charge carrier densities and the dopant density, considering that all atoms are ionized.

$$\rho = -q(p - n - N_A + N_D) \tag{2.47}$$

where p and n are respectively the hole and electron densities, and N_A and N_D are the dopant densities of the acceptor and donor atoms.

Assuming a semiclassical description, where the electron and hole densities are described using the Boltzmann approximation, in thermal equilibrium, the holes and electrons densities are given by

$$\begin{aligned} n &= n_i \exp\left(\frac{qV(x,y,z)}{k_B T}\right) \\ p &= n_i \exp\left(-\frac{qV(x,y,z)}{k_B T}\right) \end{aligned} \tag{2.48}$$

where n_i is the intrinsic carrier density.

Considering a small update δ in the known Hartree potential (V^{old}), the new potential (V^{new}) can be described as

$$V^{new} = V^{old} + \delta \tag{2.49}$$

Assuming this, Poisson's equation for V^{new} is given by

$$\nabla \cdot (\varepsilon \nabla V^{new}) = \rho^{new} \tag{2.50}$$

Substituting equation (2.49) in equation (2.50) results in

$$\nabla \cdot \left(\varepsilon \nabla V^{old}\right) + \nabla \cdot (\varepsilon \nabla \delta) = \rho^{new} \tag{2.51}$$

In which

$$\rho^{new} = -q\left(n_i \exp\left(-\frac{qV^{new}}{k_B T}\right) - n_i \exp\left(\frac{qV^{new}}{k_B T}\right) - N_A(x,y,z) + N_D(x,y,z)\right) \tag{2.52}$$

The charge density ρ^{new}can be approximated using the first and second term of Taylor series expansion around V^{old}

$$\rho^{new} = \rho^{old} + \left.\frac{\partial \rho^{new}}{\partial V^{new}}\right|_{V^{old}} \delta \tag{2.53}$$

where

$$\rho^{old} = -q\left(n_i \exp\left(-\frac{qV^{old}}{k_B T}\right) - n_i \exp\left(\frac{qV^{old}}{k_B T}\right) - N_A(x,y,z) + N_D(x,y,z)\right) \tag{2.54}$$

and

$$\left.\frac{\partial \rho^{new}}{\partial V^{new}}\right|_{V^{old}} = \frac{q^2}{k_B T}\left(n^{old} + p^{old}\right) \tag{2.55}$$

In which n^{old} and p^{old} are the charge carrier densities related to the potential V^{old}. Substituting equation (2.55) into equation (2.53) results in

$$\rho^{new} = \rho^{old} + \frac{q^2}{k_B T}\left(n^{old} + p^{old}\right)\delta \tag{2.56}$$

Substituting equation (2.56) into equation (2.51) and rearranging the terms results in

$$\nabla \cdot (\varepsilon \nabla \delta) - \frac{q^2}{k_B T}\left(n^{old} + p^{old}\right)\delta = \rho^{old} - \nabla \cdot \left(\varepsilon \nabla V^{old}\right) \tag{2.57}$$

Equation (2.57) is the final expression used to calculate the Hartree potential in the Poisson solver. The Laplacian terms are expressed in their discrete form (equation (2.45)). The right-hand side of equation (2.57) is called force function and is expressed as

$$f = \rho^{old} - \nabla \cdot \left(\varepsilon \nabla V^{old}\right) \tag{2.58}$$

In which $\nabla \cdot (\varepsilon \nabla V^{old})$ is given by

$$\nabla \cdot \left(\varepsilon \nabla V^{old}\right) = B_{i,j,k} V^{old}_{i,j,k-1} + C_{i,j,k} V^{old}_{i,j-1,k} + D_{i,j,k} V^{old}_{i-1,j,k} + E_{i,j,k} V^{old}_{i,j,k} + F_{i,j,k} V^{old}_{i,+1,j,k} + G_{i,j,k} V^{old}_{i,j+1k} + H_{i,j,k} V^{old}_{i,j,k+1} \tag{2.59}$$

The left-hand side of equation (2.57) is related to δ. The first term of the left-hand side ($\nabla \cdot (\varepsilon \nabla \delta)$) is calculated using the discrete representation of the Laplacian, which is expressed as

$$\nabla \cdot (\varepsilon \nabla \delta) = B_{i,j,k} \delta_{i,j,k-1} + C_{i,j,k} \delta_{i,j-1,k} + D_{i,j,k} \delta_{i-1,j,k} + E_{i,j,k} \delta_{i,j,k} + F_{i,j,k} \delta_{i,+1,j,k} + G_{i,j,k} \delta_{i,j+1k} + H_{i,j,k} \delta_{i,j,k+1} \tag{2.60}$$

To consider the second term of the left-hand side of equation (2.57), the coefficient $E_{i,j,k}$ is rewritten as

$$E_{i,j,k} = -B_{i,j,k} - C_{i,j,k} - D_{i,j,k} - F_{i,j,k} - G_{i,j,k} - H_{i,j,k} - \frac{q^2}{k_B T} \left(n^{old} + p^{old}\right) \tag{2.61}$$

Equation (2.57) represents a $Ax = b$ problem, in which A represents the coefficients of the discretization, b represents the force function and x is δ.

In our Monte Carlo device simulator, the Poisson solver uses an iterative method called strongly implicit procedure (SIP) (STONE, 1968) to solve Poisson's equation. The Hartree potential that accelerates the electrons during the next observation time in the Monte Carlo transport simulation is obtained at the end of the previous observation times (using the charge distribution calculated after the transport simulation). Thus, during an observation time, the potential profile is frozen.

The inputs of the Poisson solver are the potential profile of the previous observation time (V^{old}) and the charge density that is calculated at the end of the transport simulation (ρ^{old}). At the end of an iteration of the Poisson solver, the convergence is checked. If the δ is small enough, the iteration process is ended, and the potential profile of the next observation time is obtained. Otherwise, a new iteration starts, where $V^{old} = V^{new}$. In the Poisson solver iteration, the charge density is not updated. Therefore, ρ^{old} is kept as the charge density that was calculated at the end of the transport simulation.

In the Monte Carlo device simulator, after the end of the transport simulation, the charge density is evaluated at each mesh point to solve Poisson's equation and obtain the potential

profile of the next observation time. When we are simulating n-type transistors, the density of holes is calculated at each mesh node using a quasi-equilibrium approximation given by

$$p_{i,j,k} = N_V F_{\frac{1}{2}}\left(E_c - E_i - E_g - q\frac{V_{i,j,k}}{k_B T}\right) \tag{2.62}$$

where $p_{i,j,k}$ is the density of holes at the mesh point i, j, k, N_V is the effective density of states of the valence band, and $F_{\frac{1}{2}}$ is the Fermi-Dirac integral of order ½. E_C, E_i, and E_g are, respectively, the conduction band, intrinsic Fermi level and the bandgap energy. $V_{i,j,k}$ is the potential at the mesh point i, j, k calculated in the previous observation time.

To determine the density of the dopants and the density of the electrons at each mesh node, a charge assignment procedure is employed, which will be discussed in the next section.

2.2.1 Charge Assignment

As mentioned in the previous section, to numerically solve Poisson's equation, the charge density at each mesh node must be calculated. In n-type MOSFET, the charge density of holes is given by equation (2.62). The charge of particles that can be distributed anywhere inside the device (dopants and electrons) must be assigned to the mesh points. Considering that the dopants are static particles, the procedure to attribute the dopants to the mesh nodes can be performed only once, whereas the process of assigning the charge of the electrons to the mesh nodes must be performed after their trajectory is updated. Therefore, after simulating the dynamics of the electrons in the Monte Carlo transport simulation, their charge must be assigned to the mesh nodes of the cell they are inside.

The assignment of the charge of an electron to the mesh points consists of, firstly, finding the mesh cell where the particle is. Secondly, attributing the charge of the particle to the mesh nodes of the cell in accordance with the rules of assignment of the chosen method. In this device simulator, the cloud-in-cell (CIC) method is employed to assign the charge of the particles to the mesh nodes of the cell. The CIC scheme consists of attributing a fraction of the charge for each of the mesh nodes of the cell in which the particle is. The charge that is assigned to each node is weighted by the distance between the particle and the node.

Finally, the particle density at the mesh point i, j, k is calculated as

$$ch(i,j,k) = \frac{Q(i,j,k)}{qvol(i,j,k)} \quad (2.63)$$

where $Q(i,j,k)$ is the total charge attributed to the mesh point i,j,k and $vol(i,j,k)$ is the volume associated to the mesh point i,j,k.

2.2.2 Electric Field and Electric Force Calculation

The force responsible for accelerating the electrons in the Monte Carlo transport simulation comes from the Hartree potential, which is calculated by Poisson's equation solver. To calculate the electric field equation (2.64) is employed.

$$\mathbf{E}(x,y,z) = -\nabla \mathrm{V}(x,y,z) \quad (2.64)$$

To calculate the electric field at the mesh point (i,j,k), equation (2.64) must be transformed into its discrete form. Using the first order central difference scheme, the discrete component of the electric field in the *x*, *y*, and *z* directions, are given by equations (2.65), (2.66), and (2.67), respectively.

$$E_x(i,j,k) = -\frac{1}{2}\left(\frac{V(i+1,j,k) - V(i,j,k)}{X_i} + \frac{V(i,j,k) - V(i-1,j,k)}{X_{i-1}}\right) \quad (2.65)$$

$$E_y(i,j,k) = -\frac{1}{2}\left(\frac{V(i,j+1,k) - V(i,j,k)}{Y_j} + \frac{V(i,j,k) - V(i,j-1,k)}{Y_{j-1}}\right) \quad (2.66)$$

$$E_z(i,j,k) = -\frac{1}{2}\left(\frac{V(i,j,k+1) - V(i,j,k)}{Z_k} + \frac{V(i,j,k) - V(i,j,k-1)}{Z_{k-1}}\right) \quad (2.67)$$

The process to calculate the resulting mesh force that acts upon each electron consists of finding the mesh cell in which the electron is located, after that, the force that acts on the electron is calculated by interpolating the forces of all eight mesh points using the same scheme used to assign the particle charge to the mesh nodes. Thus, in the CIC method, the mesh force seen by the *i-th* electron is the sum of the mesh force of the *n-th* node (F^n) weighted by the distance from the electron to the *n-th* node (w^n) over all the eight nodes of the cell where the electron is located.

$$F_i = \sum_{n=1}^{8} F^n w^n \tag{2.68}$$

2.3 Boundary Conditions

In Monte Carlo device simulators, there are two types of boundary conditions. The boundary conditions that limit the dynamics of the electrons in the ensemble Monte Carlo routine, and boundary conditions that represent the terminals of the device in the solution of Poisson's equation.

The boundary conditions of the Monte Carlo transport simulation are the physical device boundaries, for instance, the sides, the bottom, the top, and the interfaces between different materials. To simulate them properly, each boundary should be modeled to obtain results that represent their physical nature. Thus, the side and bottom boundaries are treated as a reflecting boundary condition, when electrons cross these boundaries, they are reflected into the device with the same velocity. Thus, the magnitude of velocity is not changed, but the direction of the velocity along the direction normal to the surface is reflected (GROSS, 1999).

The boundary condition for the interface between silicon and silicon dioxide is considered as surface roughness scattering mechanism. Taking into consideration the wave-like behavior of electrons, the interaction of electrons with a surface can be explained as a diffraction phenomenon. The electrons that hit a perfectly smooth surface would always suffer a specular reflection, while electrons that hit a rough surface would always suffer a diffuse reflection. The so-called Fuchs' approach (FUCHS, 1938) consists of describing the interaction between the surface roughness and the electron as a combination of diffuse and specular scattering. The probability of specular scattering is given by p_s, while the probability of diffuse scattering is 1-p_s. The surface roughness scattering is then implemented in Monte Carlo simulations by generating a random number that defines whether the probability of scattering is either diffusive or specular. In the literature, this approach was successfully employed in planar bulk, and SOI devices, and in both p-type and n-type devices (FISCHETTI; LAUX, 1988), (VASILESKA; GROSS; FERRY, 2000), (BUFLER; SCHENK; FICHTNER, 2000), (LAUX; FISCHETTI, 1997). Laux and Fischetti (1997) suggested that the specular and diffuse scattering rates could be adjusted so the current calculated by the Monte Carlo device simulator is equal to the Drift-Diffusion current at low bias, where the drift-diffusion model is valid. In terms of tri-gate

transistors, this approach has been employed by (BUFLER; SMITH, 2013) in a FinFET, where the specular scattering probability was set to 85%, thus the diffuse probability was set to 15%.

During the transport simulation, electrons are allowed to leave the source and drain contacts, contributing to the current of the respective terminal. The source and drain terminals are ohmic contacts, because of that, the source and drain contacts and their vicinity must be charge neutral. After simulating the transport of electrons, a routine checks the charge neutrality of these regions. In this routine, electrons can be injected or deleted to balance the number of electrons and dopant ions in these regions. If there are fewer electrons than dopant ions in any cell in these regions, this routine injects electrons. The energy of the electrons injected is given by the Boltzmann distribution; hence, their average energy is the thermal energy. The wavevector of the electrons injected is oriented towards the interior of the surface where they are injected. The position of the electrons injected is randomly set in the cell where electrons are missing. This routine also checks if there are more electrons than dopant ions in any cell in these regions, in this case, the electrons in excess are removed from the simulation. If the injection and deletion are not adequately performed in this routine, it might impact the simulation results. Thus, to assure that this routine is performed correctly, the doping density and the electron density in these regions should be similar.

In terms of Poisson's equation, the Neumann and Dirichlet are the types of boundary conditions employed (GROSS, 1999). For the contacts, the Dirichlet condition is applied, in which the potential is constant and assumes the value of the bias voltage applied to the terminal. For the other surfaces of the devices, the Neumann condition is employed, in which the derivative of the potential normal to the surface is zero.

2.4 Monte Carlo Device Simulator Flowchart

The first version of the Monte Carlo device simulator employed in this work was developed by Gross (1999) during his Ph.D. work at Arizona State University to simulate a silicon n-type planar transistor. Our research group has been improving this Monte Carlo device simulator in terms of implementing different transistors structures and including the effects of relevant physics phenomena to investigate the state-of-art transistors. The first improvement made by our research group (CAMARGO, 2016) was including the structure of a silicon p-type

planar transistor. In the second work (ROSSETTO, 2018), a thermal module was incorporated into the device simulator to consider the impact of self-heating in p-type silicon planar transistors. Most recently, the subroutines employed to simulate the n-type silicon planar transistor were improved and the structure of an n-type silicon FinFET transistor was included (FURTADO, 2021).

The simulator was written in FORTRAN 77 language and is formed by thirteen source files, where several subroutines and functions are employed to simulate the operation of transistors. Note that subroutines and functions must be included or modified to implement the improvements in the simulator.

Figure 2.7 shows the flowchart of our device simulator and each step of the Monte Carlo device simulation is described below.

Figure 2.7: Flowchart of the Monte Carlo device simulator.

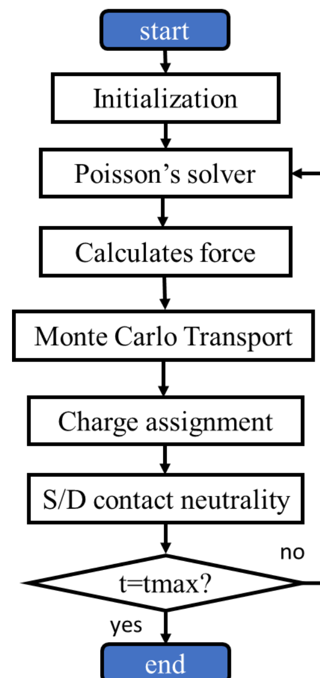

Source: Elaborated by the author.

1. Initialization
    a. Read input files

The initialization of the device simulation starts by reading the files that the final user can edit. These files contain the parameters that describe the type of simulation and the device. In terms of the type of simulation, the user can choose the charge assignment method employed and the type of device (n-type MOSFET, p-type MOSFET, n-type FinFET). In addition, if the users select a silicon p-type planar transistor, they can choose between including the thermal

mode or performing an isothermal simulation. Concerning the parameter that defines the device, the user can define the size of the device, the doping density in each region, the temperature, the method of initialization of the electrons, the bias applied in each terminal, and the number of mesh cells in each direction.

b. Scattering tables

Then the second step is calculating the scattering rates for all scattering mechanisms that are relevant. The scattering rates are stored in the scattering table as a function of the electron energy. When an electron is scattered, the scattering table is accessed to determine which scattering mechanism will be responsible for terminating its free flight.

c. Initializing the electrons

After creating the scattering tables, the next step is initializing the electrons. The user can select whether the initial energy, wavevector, free-flight time, and valley will be attributed to the electron by reading an input file or by randomly attributing them to the electrons using the electron initialization routine.

d. Create the mesh

This step concerns discretizing the device by creating the mesh. As it was mentioned, the number of mesh cells and the size of the device in each direction are read in the input files. In this process, it is attributed to each mesh node a position and a mesh spacing, which is the distance between two consecutive mesh nodes.

e. Distributing the dopants

The average number of dopants is calculated in accordance with the dopant density chosen by the user and the volume of the region that will be doped. Since the number of dopants in nanoscale devices follows a Poisson distribution function, the number of dopants is calculated using a Poisson distribution whose average value is the average number of dopants. After calculating the number of dopants, the dopants are randomly distributed in the semiconductor. It is also in this step that the charge of the dopants is assigned to the mesh nodes using the CIC particle charge assignment method. Note that the dopants are static, therefore their charge assignment to the mesh points is performed only in the initialization. By treating the dopant ions as particles, the effect of random dopant fluctuation on the transistor's properties can be assessed by this device simulator.

f. Calculates the initial potential assuming charge neutrality

Assuming charge neutrality, the carrier density and the potential are calculated for each mesh point.

g. Solves Poisson's equation in equilibrium

Poisson's equation is solved assuming thermal equilibrium by applying the set bias at the gate contact, and keeping the other contacts at 0 V. In this step, to calculate the first iteration of the Poisson solver, the initial guess is the initial potential calculated in step (f).

h. Initializes the electron position based on the charges of each mesh node

The position of the electrons is set in accordance with the charge density at each mesh node.

i. Checks charge neutrality

In this step, the code checks if it is necessary to add or delete electrons in the vicinity of the source and drain contacts to guarantee charge neutrality in these regions and properly describe an ohmic contact.

j. Assign the biases to all the terminals

Now a bias is applied to each terminal (source, drain, and body terminals).

After the (j) step, the initialization process is ended.

2. Solve Poisson

   Poisson's equation is solved.

3. Calculate the Electric Field and Force

   After the solution of Poisson's equation converges, the electric field at each mesh point and the mesh force that acts on each electron are calculated.

4. Monte Carlo Transport

   The transport of the electrons is simulated for a period equal to one observation time.

5. Charge Assignment

The density of holes is calculated at each mesh node using equation (2.62), while the charge of electrons is assigned to the mesh nodes of the cell the electron is inside using the CIC charge assignment method.

6. Checks charge neutrality

In this step, the code checks if it is necessary to add electrons in the vicinity of the source and drain contacts to guarantee charge neutrality.

Goes back to step (2) until the final time is reached. Note that the transport of the electrons is simulated in the Monte Carlo transport simulation. At the end of the observation time, the electric fields that will accelerate the electrons at the next observation time are calculated in the Poisson solver.

To couple the Monte Carlo transport simulation and Poisson's solver, some aspects must be considered. The Hartree potential of the time $N\Delta t$ is calculated by the Poisson solver using the charge distribution of the time $(N-1)\Delta t$. Between the interval of time $(N+1)\Delta t$ and $N\Delta t,$ it is assumed that the Hartree potential is static, and the electrons are accelerated using the electric field that was calculated at $N\Delta t$. To find stable results, the appropriate observation time and the mesh spacing must be chosen. The observation time must be much smaller than the inverse plasma frequency, which is given by (VASILESKA; GOODNICK; KLIMECK, 2010)

$$\frac{1}{\omega_p} = \sqrt{\frac{\varepsilon_{si} m_{eff}}{q^2 n}} \tag{2.69}$$

where ε_{si} is the permittivity of silicon.

A good spatial resolution of the potential is found when the mesh space can resolve the charge variations. Thus, the adequate mesh spacing must be smaller than the smallest wavelength of the charge variation, which is given by the Debye length (VASILESKA; GOODNICK; KLIMECK, 2010).

$$\lambda_D = \sqrt{\frac{\varepsilon_{si} k_B T}{q^2 n}} \tag{2.70}$$

The observation time and the mesh spacing are also related to each other. If the observation time is too long, the distance an electron travels in an observation time might be much bigger than the mesh space; thus, the force that accelerates the electron is obsolete, and

the assumption that the Hartree potential is static between two consecutive observation times is no longer valid (GROSS, 1999). To avoid this, the observation time should be short enough (around 1 fs and 0.01 fs) so that the maximum distance the electron can travel during an observation time is shorter than the mesh spacing.

3 QUANTUM CORRECTION

Quantum effects became important as the dimensions of transistors reached the nanometer scale (HAN; WANG, 2013). In n-type FinFET and nanowire transistors, electrons are confined in two directions (along the width and height directions of these devices) where a two-dimensional quantum well is formed (RAMAYYA; KNEZEVIC, 2010). This quantum well is formed due to the conduction band offset between silicon and silicon dioxide and the nanometric dimensions of these devices. The electron confinement in FinFET and nanowire transistors results in the reduction of electron density in their channel. In terms of the transistor's electrical properties, this effect decreases the drain current of the device (WU; SU, 2009). Besides reducing the electron density, the quantum confinement also shifts the distribution of electrons away from the silicon/silicon dioxide interface, impacting the capacitance and threshold voltage of the device (LEE, 2006), (KOBAYASHIA; HIRAMOTO, 2008). In summary, quantum effects can impact the electrical characteristics of transistors, such as threshold voltage, drain current, and channel capacitance (RAMEY, 2003).

In computational electronics, these quantum effects can be considered by coupling a Schrödinger-Poisson solver to a Monte Carlo transport simulation or by including a quantum correction into the Monte Carlo device simulator. The Schrödinger-Poisson solver coupled to the Monte Carlo transport simulation method is based on solving the 2D Schrödinger-Poisson equations along the directions where the 2D quantum well is formed and simulating the transport along the direction in which the electrons are free to move. Thus, the transport is simulated considering that the potential of the 2D quantum well is fixed along the entire transport direction (JACOBONI, 1989). Along the channel of a transistor, this potential varies; thus, the assumption of a fixed potential is not adequate for field effect transistors. In addition, this method is very time and memory-consuming (JACOBONI, 1989).

The quantum correction method is based on employing a potential that encompasses these quantum effects (FERRY, 2018; RAMEY, 2003). In this work, the Effective Potential that was proposed by Ferry (2000) is included in the Monte Carlo device simulator of n-type tri-gate transistors to consider the quantum behavior of electrons. The only parameter of this potential is the standard deviation of the Gaussian wake packet, and it physically represents the effective size of the electron (FERRY, 2018). This parameter can be obtained by adjusting it so that the line density of the electron calculated using the Effective Potential agrees with the line density obtained by the solution of the Schrödinger-Poisson equations (YAMAKAWA, 2005).

The line density is the linear density of electrons that will move from the source to the drain at a given cross-section. In this way, the Schrödinger and Poisson equations are self-consistently solved once. To include the Effective Potential model in the device simulation, the Effective Potential is calculated after solving Poisson's equation at each observation time. Note that by using this approach, the computational time of the simulation is not significantly increased, and the Schrödinger equation solution is employed as a reference (AKIS, MILICIC; FERRY; VASILESKA, 2001).

3.1 Effective Potential Approach

In quantum physics, the size of electrons is described by their wave function and their de Broglie wavelength (FERRY, 2018). For long-channel devices, the size of electrons is negligible in comparison with the device dimensions; therefore, the electrons can be treated as zero-sized particles (FERRY, 2018). However, the size of electrons in nanoscale devices is no longer negligible. The Effective Potential approach proposed by Ferry (2000) concerns identifying the minimum area where an electron can be localized. In this method, the size of the electron is represented as the magnitude squared of the wavefunction, which is a Gaussian-wave packet (FERRY, 2018).

The expression of the Effective Potential is obtained by considering the size of electrons in the calculation of the total potential energy of a system of electrons. Equation (3.1) represents the total potential of a system of electrons (FERRY, 2018)

$$\bar{V} = \int V(\mathbf{r})n(\mathbf{r})d\mathbf{r} \tag{3.1}$$

where $V(\mathbf{r})$ is the Hartree potential, and $n(\mathbf{r})$ is the local electron density. If the electrons are considered point-like particles, their density can be rewritten as the sum of the density of a point-like particle $n_i(\mathbf{r})$ over all N_e electrons (FERRY, 2018). Thus, equation (3.1) can be rewritten as

$$\bar{V} = \int V(\mathbf{r})d\mathbf{r} \sum_{i}^{N_e} n_i(\mathbf{r}) \tag{3.2}$$

Assuming the size of the electrons is zero, the density of the electrons $n_i(\mathbf{r})$ can be expressed using a Dirac-delta function centered at $\mathbf{r}_i$.

$$\bar{V} = \int V(\mathbf{r})d\mathbf{r} \sum_{i}^{N_e} \delta(\mathbf{r} - \boldsymbol{r_i}) \tag{3.3}$$

Now, taking into account that electrons have a finite size, given by a Gaussian wave-packet, their density can be expressed using:

$$n_i(\mathbf{r}) = \int \frac{1}{(2\pi\sigma^2)^{3/2}} exp\left(-\frac{|\mathbf{r} - \mathbf{r}'|^2}{2\sigma^2}\right) \delta(\mathbf{r}' - \boldsymbol{r_i})d\mathbf{r}' \tag{3.4}$$

where σ is the standard deviation of the Gaussian wave-packet. Substituting equation (3.4) in equation (3.3) results in

$$\bar{V} = \int V(\mathbf{r})d\mathbf{r} \sum_{i}^{N} \int \frac{1}{(2\pi\sigma^2)^{3/2}} exp\left(-\frac{|\mathbf{r} - \mathbf{r}'|^2}{2\sigma^2}\right) \delta(\mathbf{r}' - \boldsymbol{r_i})d\mathbf{r}' \tag{3.5}$$

In equation (3.5), the primed and unprimed variables can be interchanged, resulting in

$$\bar{V} = \int V(\mathbf{r}')d\mathbf{r}' \sum_{i}^{N} \int \frac{1}{(2\pi\sigma^2)^{3/2}} exp\left(-\frac{|\mathbf{r} - \mathbf{r}'|^2}{2\sigma^2}\right) \delta(\mathbf{r} - \boldsymbol{r_i})d\mathbf{r} \tag{3.6}$$

Rearranging the terms of equation (3.6) results in

$$\bar{V} = \sum_{i}^{N} \int \delta(\mathbf{r} - \boldsymbol{r_i})d\mathbf{r} \int \frac{1}{(2\pi\sigma^2)^{3/2}} V(\mathbf{r}') exp\left(-\frac{|\mathbf{r} - \mathbf{r}'|^2}{2\sigma^2}\right) d\mathbf{r}' \tag{3.7}$$

The integral on the right-hand side of equation (3.7) represents the Effective Potential. Therefore, the mathematical expression of the Effective Potential is given in equation (3.8) (FERRY, 2018)

$$V_{eff}(\mathbf{r}) = \int \frac{1}{(2\pi\sigma^2)^{3/2}} V(\mathbf{r}') exp\left(-\frac{|\mathbf{r} - \mathbf{r}'|^2}{2\sigma^2}\right) d\mathbf{r}' \tag{3.8}$$

Equation (3.8) is the convolution of the classical potential with the Gaussian wave packet. Note that the Effective Potential is the Hartree potential smoothed by the Gaussian wave packet.

To compare the classical description with the effective potential description, equation (3.7) can be rewritten in the same way as equation (3.3):

$$\bar{V} = \int V_{eff}(\mathbf{r})d\mathbf{r}\sum_{i}^{N}\delta(\mathbf{r}-\boldsymbol{r}_i) \tag{3.9}$$

Equation (3.3) represents the total potential energy considering a classical description of the electrons, whereas equation (3.9) represents the total potential energy considering the wave-like behavior of electrons. The difference between them is that the former employs the Hartree potential to calculate the total potential energy, and the latter uses the Effective Potential. By comparing equation (3.3) to equation (3.9), one can conclude that the electron size is incorporated by the Effective Potential. Therefore, in the device simulation, the electrons can still be treated as zero-size particles that are exposed to the Effective Potential (FERRY, 2018).

The standard deviation of the Gaussian wave-packet σ is called the smoothing parameter of the Effective Potential and is the unique parameter of the Effective Potential approach. Equation (3.8) can be rewritten in terms of the coordinates x, y and z:

$$V_{eff}(x,y,z) = \frac{1}{(2\pi)^{3/2}\sigma_x\sigma_y\sigma_z}\iiint V(x',y',z')\exp\left(-\frac{(x-x')^2}{2\sigma_x^2}-\frac{(y-y')^2}{2\sigma_y^2}-\frac{(z-z')^2}{2\sigma_z^2}\right)dx'dy'dz' \tag{3.10}$$

Note that the potential well that the electrons are subjected to is given by the conduction band. Thus, the Effective Potential is calculated by convoluting the conduction band with the Gaussian wave packet.

3.2 Methodology to Speed up the Calculation of the Effective Potential

Considering that Poisson's equation is solved at the mesh points, the Effective Potential is calculated only at the mesh nodes as well. The integral of equation (3.10) can be transformed into a sum of volume integrals over the mesh cells that surround the mesh point i, j, k. Employing this approximation, the Effective Potential at the point mesh point i, j, k is given by

$$V_{eff}^{i,j,k} = \frac{1}{(2\pi)^{3/2}\sigma_x\sigma_y\sigma_z}\sum_{l,m,n}\int_{x_{init}}^{x_{fin}}\int_{y_{init}}^{y_{fin}}\int_{z_{init}}^{z_{fin}} V(x,y,z)\exp\left(-\frac{(x-x_i)^2}{2{\sigma_x}^2}\right) * \exp\left(-\frac{(y-y_j)^2}{2{\sigma_y}^2}\right) * \exp\left(-\frac{(z-z_k)^2}{2{\sigma_z}^2}\right)dzdydx \tag{3.11}$$

where l, m and n indexes refer to the neighboring mesh points that surround the mesh point i, j, k. And x_i, y_j, z_k are the position of the mesh point i, j, k. The triple integral in equation (3.11) is calculated over the volume of the cell. The indexes *fin* and *init* in the limits of the integrations define the line segment along the direction where the integration is being calculated.

Figure 3.1: Diagram of the mesh cells that surround the mesh point i, j, k (in red).

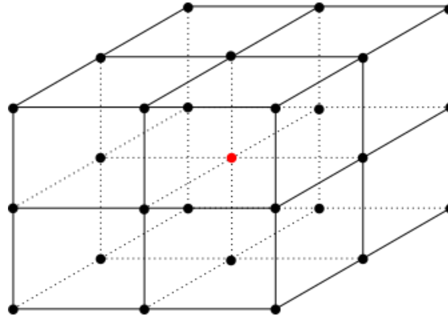

Source: Elaborated by the author.

Figure 3.1 represents the mesh point i, j, k (in red), where the Effective Potential is calculated, and the closest mesh cells that surround it. The l, m, n mesh points are defined as

$$
\begin{aligned}
l &= i \pm 1, i \pm 2, \dots, i \pm N_x \\
m &= j \pm 1, j \pm 2, \dots, j \pm N_y \\
n &= k \pm 1, k \pm 2, \dots, k \pm N_z
\end{aligned}
\tag{3.12}
$$

Where N_x, N_y and N_z are natural numbers and represent, respectively, the number of cells along x ,y and z directions considered to calculate the Effective Potential at the mesh point i, j, k using equation (3.11).

Some approximations can be made to obtain a simplified expression for the Effective Potential given by equation (3.11). First, the variables can be changed to simplify the integrals. The change of variables employed is shown in equation (3.13).

$$
\begin{aligned}
x - x_i &= x' \\
y - y_j &= y' \\
z - z_k &= z'
\end{aligned}
\tag{3.13}
$$

Substituting the variables of equation (3.11) by the variables expressed in equation (3.13) results in

$$V_{eff}^{i,j,k} = \sum_{l,m,n} \int_{x_{init}-x_i}^{x_{fin}-x_i} dx' \int_{y_{init}-y_j}^{y_{fin}-y_j} dy' \int_{z_{init}-z_k}^{z_{fin}-z_k} dz' \, V(x' + x_i, y' + y_j, z' + z_k) * \exp\left(-\frac{x'^2}{2\sigma_x{}^2} - \frac{y'^2}{2\sigma_y{}^2} - \frac{z'^2}{2\sigma_z{}^2}\right) \quad (3.14)$$

In equation (3.14), the Hartree potential $V(x' + x_i, y' + y_j, z' + z_k)$ can be estimated using the first-order Taylor approximation, resulting in

$$V(x' + x_i, y' + y_j, z' + z_k) = V(x_i, y_j, z_k) + V_x'(x_i, y_j, z_k)x' + V_y'(x_i, y_j, z_k)y' + V_z'(x_i, y_j, z_k)z' \quad (3.15)$$

where

$$V_x'(x_i, y_j, z_k) = \frac{V_{l,j,k} - V_{i,j,k}}{\Delta_x} \quad (3.16)$$

$$V_y'(x_i, y_j, z_k) = \frac{V_{i,m,k} - V_{i,j,k}}{\Delta_y} \quad (3.17)$$

$$V_z'(x_i, y_j, z_k) = \frac{V_{i,j,n} - V_{i,j,k}}{\Delta_z} \quad (3.18)$$

In equations (3.16), (3.17), and (3.18), $V_{i,j,k}$ is the Hartree potential at the i, j, k mesh point. Δ_x, Δ_y and Δ_z are de distance between the mesh point i, j, k and its neighbor along the x, y and z direction, respectively.

Substituting equations (3.16), (3.17), and (3.18) into equation (3.15), and substituting it into (3.14) results in

$$V_{eff}^{i,j,k} = \frac{1}{(2\pi)^{1.5}\sigma_x\sigma_y\sigma_z}\sum_{l,m,n}\Bigg(V_{i,j,k} * \int_{x_{init}-x_i}^{x_{fin}-x_i} dx' \int_{y_{init}-y_j}^{y_{fin}-y_j} dy' \int_{z_{init}-z_k}^{z_{fin}-z_k} dz' \exp\left(-\frac{(x')^2}{2{\sigma_x}^2}\right)\exp\left(-\frac{(y')^2}{2{\sigma_y}^2}\right)\exp\left(-\frac{(z')^2}{2{\sigma_z}^2}\right) + \left(\frac{V_{l,j,k} - V_{i,j,k}}{\Delta_x}\right) * \int_{x_{init}-x_i}^{x_{fin}-x_i} dx' \int_{y_{init}-y_j}^{y_{fin}-y_j} dy' \int_{z_{init}-z_k}^{z_{fin}-z_k} dz'\, x' \exp\left(-\frac{(x')^2}{2{\sigma_x}^2}\right)\exp\left(-\frac{(y')^2}{2{\sigma_y}^2}\right)\exp\left(-\frac{(z')^2}{2{\sigma_z}^2}\right) + \left(\frac{V_{i,m,k} - V_{i,j,k}}{\Delta_y}\right) * \int_{x_{init}-x_i}^{x_{fin}-x_i} dx' \int_{y_{init}-y_j}^{y_{fin}-y_j} dy' \int_{z_{init}-z_k}^{z_{fin}-z_k} dz'\, y' \exp\left(-\frac{(x')^2}{2{\sigma_x}^2}\right)\exp\left(-\frac{(y')^2}{2{\sigma_y}^2}\right)\exp\left(-\frac{(z')^2}{2{\sigma_z}^2}\right) + \left(\frac{V_{i,j,n} - V_{i,j,k}}{\Delta_z}\right) * \int_{x_{init}-x_i}^{x_{fin}-x_i} dx' \int_{y_{init}-y_j}^{y_{fin}-y_j} dy' \int_{z_{init}-z_k}^{z_{fin}-z_k} dz'\, z' \exp\left(-\frac{(x')^2}{2{\sigma_x}^2}\right)\exp\left(-\frac{(y')^2}{2{\sigma_y}^2}\right)\exp\left(-\frac{(z')^2}{2{\sigma_z}^2}\right)\Bigg) \tag{3.19}$$

Rearranging the terms of equation (3.19) so it can be represented as

$$V_{eff}^{i,j,k} = \frac{1}{(2\pi)^{1.5}\sigma_x\sigma_y\sigma_z}\sum_{l,m,n}\big(V_{i,j,k}I_{i,j,k,l,m,n}^{1} + (V_{l,j,k} - V_{i,j,k})I_{i,j,k,l,m,n}^{2} + (V_{i,m,k} - V_{i,j,k})I_{i,j,k,l,m,n}^{3} + (V_{i,j,n} - V_{i,j,k})I_{i,j,k,l,m,n}^{4}\big) \tag{3.20}$$

where

$$I_{i,j,k,l,m,n}^{1} = \int_{x_{init}-x_i}^{x_{fin}-x_i} dx' \int_{y_{init}-y_j}^{y_{fin}-y_j} dy' \int_{z_{init}-z_k}^{z_{fin}-z_k} dz' \exp\left(-\frac{(x')^2}{2{\sigma_x}^2}\right)\exp\left(-\frac{(y')^2}{2{\sigma_y}^2}\right)\exp\left(-\frac{(z')^2}{2{\sigma_z}^2}\right) \tag{3.21}$$

$$I^1_{i,j,k,l,m,n} = \left(\frac{\sqrt{2}\sqrt{\pi}}{2}\right)^3 \sigma_x\sigma_y\sigma_z \left[erf\left(\frac{x_{fin}-x_i}{\sqrt{2}\sigma_x}\right) - erf\left(\frac{x_{init}-x_i}{\sqrt{2}\sigma_x}\right)\right]\left[erf\left(\frac{y_{fin}-y_j}{\sqrt{2}\sigma_y}\right) - erf\left(\frac{y_{init}-y_j}{\sqrt{2}\sigma_y}\right)\right]\left[erf\left(\frac{z_{fin}-z_k}{\sqrt{2}\sigma_z}\right) - erf\left(\frac{z_{init}-z_k}{\sqrt{2}\sigma_z}\right)\right]$$

$$I^2_{i,j,k,l,m,n} = \frac{1}{\Delta_x}\int_{x_{init}-x_i}^{x_{fin}-x_i} dx' \int_{y_{init}-y_j}^{y_{fin}-y_j} dy' \int_{z_{init}-z_k}^{z_{fin}-z_k} dz'\, x' \exp\left(-\frac{(x')^2}{2{\sigma_x}^2}\right)\exp\left(-\frac{(y')^2}{2{\sigma_y}^2}\right)\exp\left(-\frac{(z')^2}{2{\sigma_z}^2}\right)$$

$$I^2_{i,j,k,l,m,n} = \frac{1}{\Delta_x}{\sigma_x}^2\left[\exp\left(-\frac{(x_{init}-x_i)^2}{2{\sigma_x}^2}\right) - \exp\left(-\frac{\left(x_{fin}-x_i\right)^2}{2{\sigma_x}^2}\right)\right]\sigma_y\sigma_z\frac{\pi}{2}\left[erf\left(\frac{y_{fin}-y_j}{\sqrt{2}\sigma_y}\right) - erf\left(\frac{y_{init}-y_j}{\sqrt{2}\sigma_y}\right)\right]\left[erf\left(\frac{z_{fin}-z_k}{\sqrt{2}\sigma_z}\right) - erf\left(\frac{z_{init}-z_k}{\sqrt{2}\sigma_z}\right)\right] \tag{3.22}$$

$$I^3_{i,j,k,l,m,n} = \frac{1}{\Delta_y}\int_{x_{init}-x_i}^{x_{fin}-x_i} dx' \int_{y_{init}-y_j}^{y_{fin}-y_j} dy' \int_{z_{init}-z_k}^{z_{fin}-z_k} dz'\, y' \exp\left(-\frac{(x')^2}{2{\sigma_x}^2}\right)\exp\left(-\frac{(y')^2}{2{\sigma_y}^2}\right)\exp\left(-\frac{(z')^2}{2{\sigma_z}^2}\right)$$

$$I^3_{i,j,k,l,m,n} = \frac{1}{\Delta_y}{\sigma_y}^2\left[\exp\left(-\frac{\left(y_{init}-y_j\right)^2}{2{\sigma_y}^2}\right) - \exp\left(-\frac{\left(y_{fin}-y_j\right)^2}{2{\sigma_y}^2}\right)\right]\sigma_x\sigma_z\frac{\pi}{2}\left[erf\left(\frac{x_{fin}-x_i}{\sqrt{2}\sigma_x}\right) - erf\left(\frac{x_{init}-x_i}{\sqrt{2}\sigma_x}\right)\right]\left[erf\left(\frac{z_{fin}-z_k}{\sqrt{2}\sigma_z}\right) - erf\left(\frac{z_{init}-z_k}{\sqrt{2}\sigma_z}\right)\right] \tag{3.23}$$

$$I^4_{i,j,k,l,m,n} = \frac{1}{\Delta_z}\int_{x_{init}-x_i}^{x_{fin}-x_i} dx' \int_{y_{init}-y_j}^{y_{fin}-y_j} dy' \int_{z_{init}-z_k}^{z_{fin}-z_k} dz'\, z' \exp\left(-\frac{(x')^2}{2{\sigma_x}^2}\right)\exp\left(-\frac{(y')^2}{2{\sigma_y}^2}\right)\exp\left(-\frac{(z')^2}{2{\sigma_z}^2}\right)$$

$$I^4_{i,j,k,l,m,n} = \frac{1}{\Delta_z}{\sigma_z}^2\left[\exp\left(-\frac{(z_{init}-z_k)^2}{2{\sigma_z}^2}\right) - \exp\left(-\frac{\left(z_{fin}-z_k\right)^2}{2{\sigma_z}^2}\right)\right]\sigma_x\sigma_y\frac{\pi}{2}\left[erf\left(\frac{x_{fin}-x_i}{\sqrt{2}\sigma_x}\right) - erf\left(\frac{x_{init}-x_i}{\sqrt{2}\sigma_x}\right)\right]\left[erf\left(\frac{y_{fin}-y_j}{\sqrt{2}\sigma_y}\right) - erf\left(\frac{y_{init}-y_j}{\sqrt{2}\sigma_y}\right)\right] \tag{3.24}$$

The coefficients $I^1_{i,j,k,l,m,n}$, $I^2_{i,j,k,l,m,n}$, $I^3_{i,j,k,l,m,n}$, and $I^4_{i,j,k,l,m,n}$ depend only on the mesh size. Therefore, they can be calculated ahead of time. Thus, to speed up the process, these coefficients of each mesh point are calculated in the initialization process of the simulation.

To verify the agreement between the integral over the entire space and the sum of integrals over cells, the convolutions expressed in equations (3.25) and (3.26) were calculated numerically using MATLAB software and the approximation given by equation (3.20).

$$C(4,4,4) = \iiint(-x'+12)(-y'+12)(z'+12)\exp\left(-\frac{(4-x')^2}{2(0.5^2)} - \frac{(4-y')^2}{2(0.5^2)}\ \frac{(4-z')^2}{2(0.5^2)}\right) dx'\, dy'\, dz' \tag{3.25}$$

$$C(4,4,4) = \iiint(x'y'z')\exp\left(-\frac{(4-x')^2}{2(0.5^2)} - \frac{(4-y')^2}{2(0.5^2)} - \frac{(4-z')^2}{2(0.5^2)}\right) dx'\, dy'\, dz' \tag{3.26}$$

In these two convolutions, the standard deviation of the Gaussian function is equal to 0.5 and the convolution was calculated at the point (4,4,4). The results of the convolutions are shown in Table 3.1. A good agreement was found when the smoothing was performed over the cells that were in a radius equal to four standard deviations of the Gaussian wave packet. Thus, the distance between the cells considered to calculate the Effective Potential at the point *i,j,k* and the point *i,j,k* is less than four smoothing parameters (standard deviation of the Gaussian wave packet).

Table 3.1: Results of the integrals of equations (3.25) and (3.26).

Linear Function	Convolution Solved analytically	Employing the method of Equation (3.20)
$(-\boldsymbol{x}+\mathbf{12})(-\boldsymbol{y}+\mathbf{12})(-\boldsymbol{z}+\mathbf{12})$	1.0080×10^{3}	1.0078×10^{3}
$(\boldsymbol{xyz})$	125.9969	125.9729

4 EXTRACTION OF THE SMOOTHING PARAMETERS OF THE EFFECTIVE POTENTIAL

As mentioned in Chapter 0, in n-type FinFET and nanowire transistors, the confinement of electrons occurs along the width and height directions of these devices, near the silicon and oxide interface where a two-dimensional quantum well is formed (RAMAYYA; KNEZEVIC, 2010). To obtain the smoothing parameter of the Effective Potential for these two transistors, a 2D Effective Potential-Poisson solver and a 2D Schrödinger-Poisson solver for the cross-section of both devices were developed. The cross-section of the n-type FinFET and n-type nanowire transistors are simulated to calculate the line density of electrons using these two solvers. The smoothing parameter of the Effective Potential for these two transistors is adjusted until the line density of electrons calculated by the Effective Potential coincides with the one calculated by the Schrödinger-Poisson solver. In this way, the Schrödinger equation – which is too time and memory-consuming – needs to be calculated only once. Note that the confinement occurs along the height and width direction of these devices, because of that, in this chapter, only this cross-section is relevant. Figure 4.1 and Figure 4.2 show the cross-section of the Silicon FinFET and the cross-section of the silicon nanowire transistor, respectively.

Figure 4.1 – Cross-section of the FinFET device investigated in this work. The cross-section is along the height and the width of the transistor. The metal gate is represented in red; the silicon is represented in blue, and the dielectric is represented in gray. W_{fin} and H_{fin} represent the fin width and height respectively

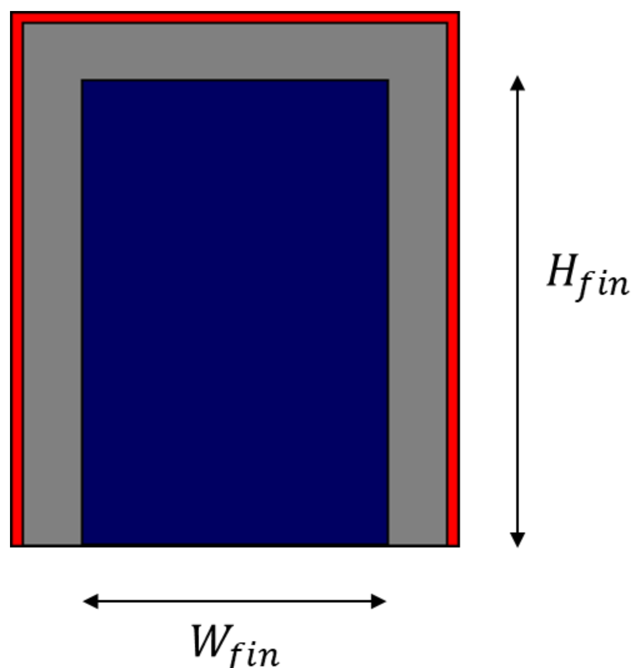

Source: Elaborated by the author.

Figure 4.2: Cross-section of the silicon nanowire transistor investigated in this work. The cross-section is along the height and the width of the transistor. The metal gate is represented in red; the silicon is represented in blue, and the dielectric and the buried oxide are represented in gray. W_{fin} and H_{fin} represent the fin width and height respectively

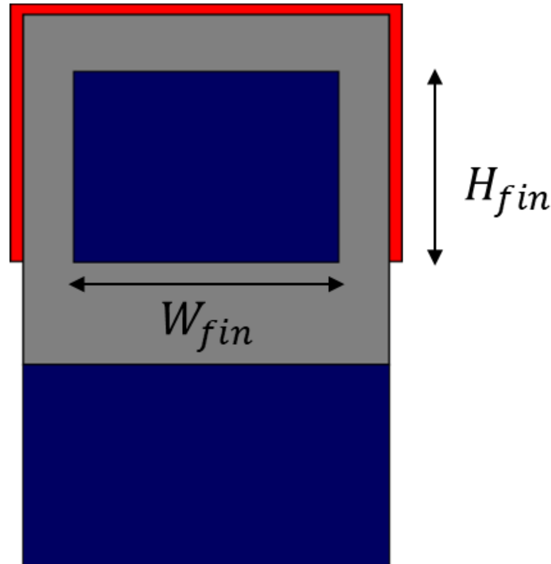

Source: Elaborated by the author.

In this chapter, the 2D Schrödinger-Poisson solver is explained in Section 4.1, and the 2D Effective Potential-Poisson solver is explained in Section 4.2. The results obtained by them are presented in Section 4.3.

4.1 2D Schrödinger-Poisson Solver

In the following sections, the 2D Schrödinger-Poisson solver employed in this work will be explained. The 2D Schrödinger-Poisson solver was developed by Baikadi (2020) to simulate devices of AlGaN-GaN and AlGaN-AlN-GaN. In this work, this solver was modified to simulate the cross-section of tri-gate devices (n-type silicon FinFET and nanowire transistors). In section 4.1.1 the Schrödinger equation solver is explained, then, in Section 4.1.2, the 2D Poisson's equation solver is briefly explained. Section 4.1.3 explains how these two equations are solved self-consistently, and finally, Section 4.1.4 presents the flowchart of the Schrödinger-Poisson Solver.

4.1.1 The 2D Schrödinger equation

The Schrödinger equation of interest is given by (ESSENI; PALESTRI; SELMI, 2011)

$$\big(H_o + U(x,y,z)\big)\Psi(\mathrm{x,y,z}) = E\Psi(\mathrm{x,y,z}) \tag{4.1}$$

Where H_o is the one-electron Hamiltonian of the crystal, and $U(x,y,z)$ is the confinement potential. The Schrödinger equation of the one-electron Hamiltonian is defined as

$$H_o\varphi_{m,\mathbf{k}}(x,y,z) = E_m(\mathbf{k})\varphi_{m,\mathbf{k}}(x,y,z) \tag{4.2}$$

Where $\varphi_{m,\mathbf{k}}(x,y,z)$ is a Bloch wavefunction, and $E_m(\mathbf{k})$ is the energy of the band *m*, which is a continuous function of *k*. The wavefunction of equation (4.1) is defined as (ESSENI; PALESTRI; SELMI, 2011):

$$\Psi(x,y,z) = \varphi_{n,\mathbf{k}}(x,y,z)\psi(x,y,z) \tag{4.3}$$

Where $\psi(x,y,z)$ is an unknown envelope function. Using equation (4.2) and recalling that the energy bands are periodic in the reciprocal space, thus $E_m(\mathbf{k})\varphi_{m,\mathbf{k}}(x,y,z) = E_m(-i\nabla)\varphi_{m,\mathbf{k}}(x,y,z)$, equation (4.1) results in

$$\big(E_m(-i\nabla) + U(x,y,z)\big)\varphi_{m,\mathbf{k}}(x,y,z)\psi(x,y,z) = E\varphi_{m,\mathbf{k}}(x,y,z)\psi(x,y,z) \tag{4.4}$$

Hence, the Schrödinger equation of the envelope function $\psi(x,y,z)$ is given by

$$\big(E_m(-i\nabla) + U(x,y,z)\big)\psi(x,y,z) = E\psi(x,y,z) \tag{4.5}$$

Note that we are interested in the impact of quantum confinement in the conduction band of silicon; thus, we can change the index in equation (4.5) from *m* to *C*. Besides, the confinement potential in n-type FinFET and nanowire transistors is a 2D potential well along height of the transistor (*y*-direction) and along the width of the transistor (*z*-direction) that is formed due to the conduction band offset between silicon and silicon dioxide ($E_C(y,z)$). Considering that, equation (4.5) can be rewritten as

$$\big(E_C(-i\nabla) + E_C(y,z)\big)\psi(x,y,z) = E\psi(x,y,z) \tag{4.6}$$

As it was discussed in Section 2.1.2, the minimum of the silicon conduction band is located at the symmetry point Δ. The Schrödinger equation must be solved for the three-

degenerate valley pairs along the direction (100), (010), and (001), and their degeneracy must be taken into account. The Hamiltonian of the electrons confined in the ν-th valley pair of the silicon conduction band is obtained by substituting **k** for $-i\nabla$ in the dispersion relation of the valley-pair (equation (2.12)) (ESSENI; PALESTRI; SELMI, 2011),(HAMAGUCHI, 2013), and then substituting it in equation (4.6), which results in

$$H = -\left(\frac{\hbar^2}{2{m_x}^\nu}\frac{\partial^2}{\partial x^2}+\frac{\hbar^2}{2{m_y}^\nu}\frac{\partial^2}{\partial y^2}+\frac{\hbar^2}{2{m_z}^\nu}\frac{\partial^2}{\partial z^2}\right)+E_C(y,z) \tag{4.7}$$

where ${m_x}^\nu$ is the effective mass along the x-direction of the ν-th valley pair, ${m_y}^\nu$ is the effective mass along the y-direction of the ν-th valley pair, and ${m_z}^\nu$ is the effective mass along the z-direction of the ν-th valley pair. As it was discussed in Section 2.1.2, the effective mass of the valley pair along the (100) direction is $m_x = m_l$, $m_y = m_t$ and $m_z = m_t$. The effective mass of the valley pair along the (010) direction is $m_y = m_l$, $m_x = m_t$ and $m_z = m_t$. And for the valley pair along the (001) direction $m_z = m_l$, $m_x = m_t$ and $m_y = m_t$.

Considering that the potential $E_C(y,z)$ is constant along the x-direction, the Hamiltonian can be expressed as

$$H = H_\parallel + H_\perp \tag{4.8}$$

Where $H_\parallel$ is the component of the Hamiltonian that is parallel to the confinement, and $H_\perp$ is the component of the Hamiltonian that is perpendicular to the confinement. The perpendicular component is along the length direction of these devices (x-direction). It is assumed that the electrons are free particles along this direction, hence, their wavefunction along this direction is a plane wave.

The parallel component of the Hamiltonian is defined as

$$H_\parallel = -\left(\frac{\hbar^2}{2{m_y}^\nu}\frac{\partial^2}{\partial y^2}+\frac{\hbar^2}{2{m_z}^\nu}\frac{\partial^2}{\partial z^2}\right)+E_C(y,z) \tag{4.9}$$

To obtain the eigenvalues and wavefunctions of the confined electrons, the Schrödinger equation given by equation (4.10) must be solved.

$$-\left(\frac{\hbar^2}{2{m_y}^\nu}\frac{\partial^2}{\partial y^2}+\frac{\hbar^2}{2{m_z}^\nu}\frac{\partial^2}{\partial z^2}\right)\psi^{n,\nu}(y,z)+E_C(y,z)\psi^{n,\nu}(y,z) = E^{n,\nu}\psi^{n,\nu}(y,z) \tag{4.10}$$

where $\psi^{n,\nu}(y,z)$ is the wavefunction (envelope function) of the n subband of the ν valley, and $E^{n,\nu}$ is the eigenvalue of the n subband of the ν valley.

The Schrödinger equation must be discretized to be numerically solved. The control surface employed to solve the Schrödinger equation is represented by the dashed line square denoted by Ω in Figure 4.3. The indexes j and k represent, respectively, the height and width direction of the device.

Figure 4.3: Five-point stencil used to discretize the Schrödinger equation. The volume control is represented by the dashed line square. This volume control is divided into four squares, each with a surface along the *y*-direction and *z*-direction.

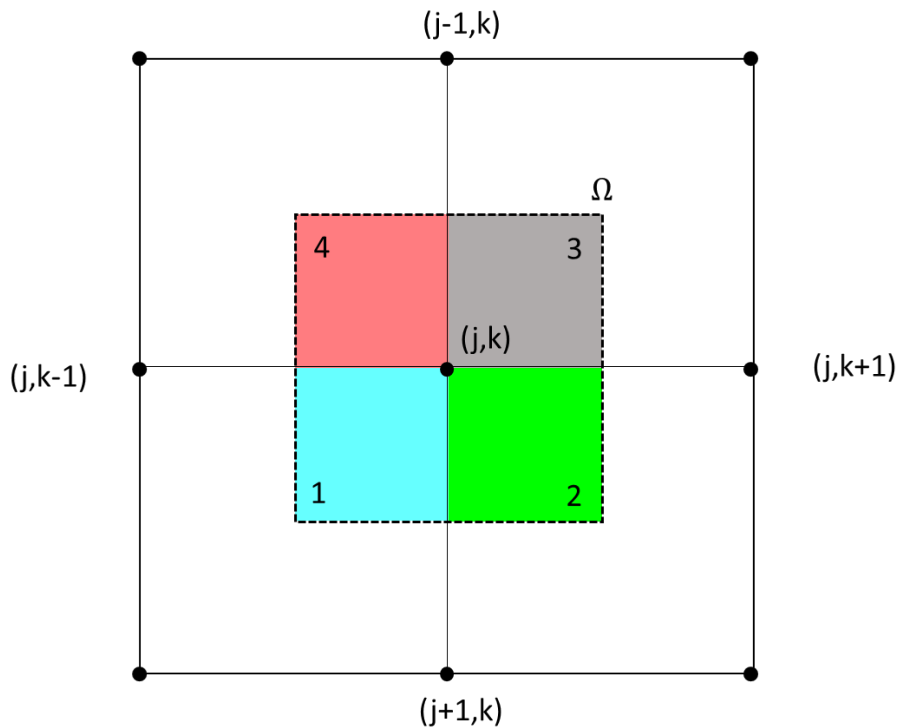

Source: Adapted from Baikadi (2020).

Baikadi (2020) employed the finite volume method to discretize the Schrödinger equation. Hence, rewriting the left-hand side of the Schrödinger equation in its integral form

$$\int\left(-\frac{\partial}{\partial x}\left(\frac{\hbar^2}{2m_y{}^{\nu}}\frac{\partial}{\partial y}\right)-\frac{\partial}{\partial y}\left(\frac{\hbar^2}{2m_z{}^{\nu}}\frac{\partial}{\partial z}\right)\right)\psi^{n,\nu}(y,z)dA+\int E_C(y,z)\psi^{n,\nu}(y,z)dA \qquad (4.11)$$

Using the Divergence Theorem $\int\nabla\cdot FdA=\int F\cdot ds$, the first term of equation (4.11) can be rewritten as

$$\int\left(-\frac{\partial}{\partial x}\left(\frac{\hbar^2}{2m_y{}^\nu}\frac{\partial}{\partial y}\right)-\frac{\partial}{\partial y}\left(\frac{\hbar^2}{2m_z{}^\nu}\frac{\partial}{\partial z}\right)\right)\psi^{n,\nu}(y,z)dA = \int\left(-\frac{\hbar^2}{2m_y{}^\nu}\frac{\partial}{\partial y}-\frac{\hbar^2}{2m_z{}^\nu}\frac{\partial}{\partial z}\right)\psi^{n,\nu}(y,z)\,ds \tag{4.12}$$

Substituting equation (4.12) into equation (4.11) results in

$$\int\left(-\frac{\hbar^2}{2m_y{}^\nu}\frac{\partial}{\partial y}-\frac{\hbar^2}{2m_z{}^\nu}\frac{\partial}{\partial z}\right)\psi^{n,\nu}(y,z)\,ds+\int E_C(y,z)\psi^{n,\nu}(y,z)dA \tag{4.13}$$

Transforming the first integral of equation (4.13) into a sum results in

$$\int\left(-\frac{\hbar^2}{2m_y{}^\nu}\frac{\partial}{\partial y}-\frac{\hbar^2}{2m_z{}^\nu}\frac{\partial}{\partial z}\right)\psi^{n,\nu}(y,z)\,ds = \sum_{k=1}^{4}-\frac{\hbar^2}{2m_y{}^\nu}\frac{\partial}{\partial y}\psi^{n,\nu}(y,z)S_{z,\mathrm{i}}-\frac{\hbar^2}{2m_z{}^\nu}\frac{\partial}{\partial z}\psi^{n,\nu}(y,z)S_{y,\mathrm{i}} \tag{4.14}$$

In equation (4.14), the sum is performed over the four curves that surround the colored squares in Figure 4.3. $S_{y,i}$ is the length of the i-th surface along the y-direction, and $S_{z,i}$ is the length of the i-th surface along the z-direction. Now, writing the derivatives in their discrete form:

$$\begin{aligned}\sum_{i=1}^{4}-\frac{\hbar^2}{2m_y{}^\nu}\frac{\partial}{\partial y}\psi^{n,\nu}(y,z)S_{y,k}-\frac{\hbar^2}{2m_z{}^\nu}\frac{\partial}{\partial z}\psi^{n,\nu}(y,z)S_{z,k} &=\\ -\frac{\hbar^2}{2}\left(\frac{1}{m_{y,1}{}^\nu}\left(\frac{\psi^{n,\nu}_{j+1,k}-\psi^{n,\nu}_{j,k}}{y_{j+1,k}-y_{j,k}}\right)S_{z,1}+\frac{1}{m_{z,1}{}^\nu}\left(\frac{\psi^{n,\nu}_{j,k-1}-\psi^{n,\nu}_{j,k}}{z_{j,k}-z_{j,k-1}}\right)S_{y,1}\right)&\\ -\frac{\hbar^2}{2}\left(\frac{1}{m_{y,2}{}^\nu}\left(\frac{\psi^{n,\nu}_{j+1,k}-\psi^{n,\nu}_{j,k}}{y_{j+1,k}-y_{j,k}}\right)S_{z,2}+\frac{1}{m_{z,2}{}^\nu}\left(\frac{\psi^{n,\nu}_{j,k+1}-\psi^{n,\nu}_{j,k}}{z_{j,k+1}-z_{j,k}}\right)S_{y,2}\right)&\\ -\frac{\hbar^2}{2}\left(\frac{1}{m_{y,3}{}^\nu}\left(\frac{\psi^{n,\nu}_{j-1,k}-\psi^{n,\nu}_{j,k}}{y_{j,k}-y_{j-1,k}}\right)S_{z,3}+\frac{1}{m_{z,3}{}^\nu}\left(\frac{\psi^{n,\nu}_{j,k+1}-\psi^{n,\nu}_{j,k}}{z_{j,k+1}-z_{j,k}}\right)S_{y,3}\right)&\\ -\frac{\hbar^2}{2}\left(\frac{1}{m_{y,4}{}^\nu}\left(\frac{\psi^{n,\nu}_{j-1,k}-\psi^{n,\nu}_{j,k}}{y_{j,k}-y_{j-1,k}}\right)S_{z,4}+\frac{1}{m_{z,4}{}^\nu}\left(\frac{\psi^{n,\nu}_{j,k-1}-\psi^{n,\nu}_{j,k}}{z_{j,k}-z_{j,k-1}}\right)S_{y,4}\right)&\end{aligned} \tag{4.15}$$

Where

$$S_{y,1}=S_{y,2}=\frac{y_{j+1,k}-y_{j,k}}{2} \tag{4.16}$$

$$S_{y,3} = S_{y,4} = \frac{y_{j,k} - y_{j-1,k}}{2}$$

$$S_{z,1} = S_{z,4} = \frac{z_{j,k} - z_{j,k-1}}{2}$$

$$S_{z,2} = S_{z,3} = \frac{z_{j,k+1} - z_{j,k}}{2}$$

The integral in the second term of equation (4.13) is transformed into a sum.

$$\int E_C(y,z)\psi^{n,\nu}(y,z)dA = \sum_{i=1}^{4} E_C(y,z)\psi^{n,\nu}(y,z)A_i \tag{4.17}$$

where A_i is the area of the i-th surface.

Writing equation (4.17) in its discrete form results in

$$\sum_{i=1}^{4} E_C(y,z)\psi^{n,\nu}(x,y)A_i =$$

$$\psi_{j,k}^{n,\nu} E_C^{j,k}\left(\left(\frac{y_{j+1,\mathrm{k}} - y_{j,k}}{2}\right)\left(\frac{z_{j,k} - z_{j,k-1}}{2}\right) + \left(\frac{y_{j+1,\mathrm{k}} - y_{j,k}}{2}\right)\left(\frac{z_{j,k+1} - z_{j,k}}{2}\right) + \left(\frac{y_{j,k} - y_{j-1,\mathrm{k}}}{2}\right)\left(\frac{z_{j,k+1} - z_{j,k}}{2}\right) + \left(\frac{y_{j,k} - y_{j-1,\mathrm{k}}}{2}\right)\left(\frac{z_{j,k} - z_{j,k-1}}{2}\right)\right) \tag{4.18}$$

Thus, equation (4.15) is the discrete form of the first term of equation (4.13) and equation (4.18) is the is the discrete form of the second term of equation (4.13). Equation (4.13) can be rewritten in the discrete form using coefficients

$$A_{j,k}\psi_{j-1,k}^{n,\nu} + B_{j,k}\psi_{j,k-1}^{n,\nu} + C_{j,k}\psi_{j,k}^{n,\nu} + D_{j,k}\psi_{j,k+1}^{n,\nu} + E_{j,k}\psi_{j+1,k}^{n,\nu} \tag{4.19}$$

Where

$$A_{j,k} = \frac{1}{{m_{y,3}}^{\nu}}\left(\frac{z_{j,k+1} - z_{j,k}}{2(y_{j,k} - y_{j-1,k})}\right) + \frac{1}{{m_{y,4}}^{\nu}}\left(\frac{z_{j,k} - z_{j,k-1}}{2(y_{j,k} - y_{j-1,k})}\right)$$

$$B_{j,k} = \frac{1}{{m_{z,1}}^{\nu}}\left(\frac{y_{j+1,k} - y_{j,k}}{2(z_{j,k} - z_{j,k-1})}\right) + \frac{1}{{m_{z,4}}^{\nu}}\left(\frac{y_{j,k} - y_{j-1,k}}{2(z_{j,k} - z_{j,k-1})}\right) \tag{4.20}$$

$$D_{j,k} = \frac{1}{{m_{z,2}}^{\nu}}\left(\frac{y_{j+1,k} - y_{j,k}}{2(z_{j,k+1} - z_{j,k})}\right) + \frac{1}{{m_{z,3}}^{\nu}}\left(\frac{y_{j,k} - y_{j-1,k}}{2(z_{j,k+1} - z_{j,k})}\right)$$

$$E_{j,k} = \frac{1}{m_{y,2}{}^{\nu}}\left(\frac{z_{j,k+1} - z_{j,k}}{2(y_{j+1,k} - y_{j,k})}\right) + \frac{1}{m_{y,1}{}^{\nu}}\left(\frac{z_{j,k} - z_{j,k-1}}{2(y_{j+1,k} - y_{j,k})}\right)$$

$$C_{j,k} = A_{j,k} + B_{j,k} + C_{j,k} + D_{j,k} + E_C^{j,k}\left(\left(\frac{y_{j+1,\mathrm{k}} - y_{j,k}}{2}\right)\left(\frac{z_{j,k} - z_{j,k-1}}{2}\right) + \left(\frac{y_{j+1,\mathrm{k}} - y_{j,k}}{2}\right)\left(\frac{z_{j,k+1} - z_{j,k}}{2}\right) + \left(\frac{y_{j,k} - y_{j-1,\mathrm{k}}}{2}\right)\left(\frac{z_{j,k+1} - z_{j,k}}{2}\right) + \left(\frac{y_{j,k} - y_{j-1,\mathrm{k}}}{2}\right)\left(\frac{z_{j,k} - z_{j,k-1}}{2}\right)\right)$$

Equation (4.19) is the discrete form of the left-hand side of the Schrödinger equation. The right-hand side of the Schrödinger equation can be rewritten as

$$\int E^{n,\nu}\psi^{n,\nu}(y,z)dA = E^{n,\nu}\psi_{i,j}^{n,\nu}A' \quad (4.21)$$

where A' is the area of the surface control Ω.

To solve the discrete form of the Schrödinger equation, equations (4.19) and (4.21) must be substituted in equation (4.22)

$$H\psi^{n,\nu}(y,z) = E^{n,\nu}\psi^{n,\nu}(y,z) \quad (4.22)$$

To solve the eigenvalue problem of equation (4.22), Baikadi (2020) employed the Scalable Library for Eigenvalue Problem Computation (SLEPc) eigenvalue solver. The eigenvector and the eigenvalue of equation (4.22) correspond to the wavefunction and the energy level of the n subband of the ν valley. Equation (4.22) is solved for each valley pair of silicon's conduction band.

After solving the Schrödinger equation, the electron line density of the n subband of the ν valley pair is given by

$$N^{n,\nu} = \int_{E^{n,\nu}}^{\infty} g(E)F(E)dE \quad (4.23)$$

Where $g(E)$ is the density of states, $F(E)$ is the Fermi-Dirac distribution. The nanowire and FinFET devices can be approximate as a quasi 1D system; thus, the density of states of electrons is given by

$$g_{1\mathrm{D}}(E) = \frac{\sqrt{2m_x}}{\pi\hbar}\frac{1}{\sqrt{E - E^{n,\nu}}}\mathcal{H}(E - E^{n,\nu}) \quad (4.24)$$

Where $\mathcal{H}(E - E^{n,\nu})$ is the Heaviside step function. Substituting equation (4.24) into equation (4.23) results in

$$N^{n,\nu} = \frac{\sqrt{2m_z}}{\pi\hbar} \int_{E^{n,\nu}}^{\infty} \frac{1}{\sqrt{E - E^{n,\nu}}} \frac{1}{1 + \exp\left(\frac{E - E_F}{k_B T}\right)} dE \quad (4.25)$$

Substituting the variable E by the variable $\epsilon = (E - E^{n,\nu})/k_B T$ in equation (4.25) results in

$$N^{n,\nu} = \frac{\sqrt{2m_z k_B T}}{\pi\hbar} \int_{0}^{\infty} \frac{\epsilon^{-\frac{1}{2}}}{1 + \exp(\epsilon - \eta^{n,\nu})} d\epsilon \quad (4.26)$$

In which $\eta^{n,\nu} = \frac{E_F - E^{n,\nu}}{k_B T}$

Equation (4.26) can be rewritten as

$$N^{n,\nu} = \frac{\sqrt{2m_z k_B T}}{\pi\hbar} F_{-1/2}(\eta^{n,\nu}) \quad (4.27)$$

where $F_{-1/2}(\eta^{n,\nu})$ is the Fermi-Dirac integral of order -1/2.

The quantum electron density is given by

$$n_Q(y, z) = 2 \sum_{n,\nu} N^{n,\nu} \; |\psi^{n,\nu}(y, z)|^2 \quad (4.28)$$

The number two multiplying the summation takes the degeneracy of the valleys.

4.1.2 The 2D Poisson solver

To solve a 2D Poisson's equation, the same procedure made to solve a 3D Poisson's equation is performed: the 2D Poisson's equation must be linearized and discretized. The difference here is that to describe the point j, k and its neighborhood, a five-point stencil is employed. The five-point stencil is depicted in Figure 4.4.

The 2D Poisson's equation is given by

$$\nabla \cdot \big(\varepsilon \nabla V(y, z)\big) = \rho \quad (4.29)$$

In the 2D Poisson solver, the finite volume method is employed to discretize Poisson's equation. Poisson's equation is represented in its integral form, resulting in

$$\int_{\Omega}\left(\frac{\partial}{\partial y}\left(\varepsilon\frac{\partial}{\partial y}V(y,z)\right)+\frac{\partial}{\partial z}\left(\varepsilon\frac{\partial}{\partial z}V(y,z)\right)\right)dA=\int_{\Omega}\rho dA \tag{4.30}$$

Figure 4.4: Five-point stencil used to discretize the 2D Poisson's equation. Four control surfaces surround the control volume (in gray).

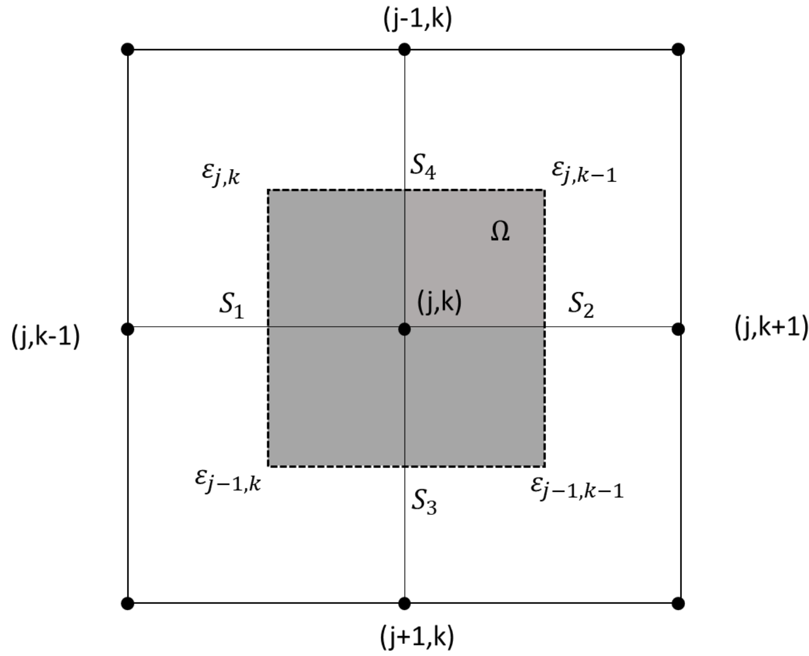

Source: Adapted from Baikadi (2020).

Where Ω is the control surface colored in gray in Figure 4.4. Using the Divergence Theorem $\int \nabla \cdot F dA = \int F \cdot ds$, the integral on the left-hand side of equation is rewritten as

$$\int_{S}\left(\left(\varepsilon\frac{\partial}{\partial y}V(y,z)\right)+\left(\varepsilon\frac{\partial}{\partial z}V(y,z)\right)\right)ds=\int_{\Omega}\rho dA \tag{4.31}$$

Where S is the curve normal to the gradient of the potential that surround the control surface (Ω). Transforming the line integral into a discrete summation over the four curves and the integral of the surface into a discrete summation over the four surfaces, results in

$$\sum_{i=1}^{4}\left(\varepsilon\frac{\partial}{\partial y}V(y,z)+\ \varepsilon\frac{\partial}{\partial z}V(y,z)\right)S_i=\sum_{i=1}^{4}\rho\, A_i \tag{4.32}$$

where S_i and A_i are the length and the area of the i-th surface.

Rewriting the left side of equation (4.32) by substituting the continuous derivatives by their discrete form, and assuming that the permittivity of each surface is the average between the permittivity of the nodes of the surface results in

$$\begin{aligned}\sum_{i=1}^{4}\left(\varepsilon\frac{\partial}{\partial y}V(y,z)+\ \varepsilon\frac{\partial}{\partial z}V(y,z)\right)S_i=&\\ \left(\frac{\varepsilon_{j,k}+\varepsilon_{j-1,k}}{2}\right)\left(\frac{V_{j,k-1}-V_{j,k}}{(z_{j,k}-z_{j,k-1})}\right)\left(\frac{y_{j+1,k}-y_{j-1,k}}{2}\right)+&\\ \left(\frac{\varepsilon_{j-1,k-1}+\varepsilon_{j,k-1}}{2}\right)\left(\frac{V_{j,k+1}-V_{j,k}}{(z_{j,k+1}-x_{j,k})}\right)\left(\frac{y_{j+1,k}-y_{j-1,k}}{2}\right)+&\\ \left(\frac{\varepsilon_{j-1,k-1}+\varepsilon_{j-1,k}}{2}\right)\left(\frac{V_{j+1,k}-V_{j,k}}{(y_{j+1,k}-y_{j,k})}\right)\left(\frac{z_{j,k+1}-z_{j,k-1}}{2}\right)+&\\ \left(\frac{\varepsilon_{j,k-1}+\varepsilon_{j,k}}{2}\right)\left(\frac{V_{j-1,k}-V_{j,k}}{(y_{j,k}-y_{j-1,k})}\right)\left(\frac{z_{j,k+1}-z_{j,k-1}}{2}\right)&\end{aligned} \tag{4.33}$$

While the right side of equation (4.32) is given by

$$\rho_{j,k}\left(\frac{z_{j,k+1}-z_{j,k-1}}{2}\right)\left(\frac{y_{j+1,k}-y_{j-1,k}}{2}\right) \tag{4.34}$$

where j and k represent, respectively, the height and the width direction of the device. Rewriting equation (4.32) using the expressions demonstrated in equations (4.33) and (4.34) results in

$$\begin{aligned}&\left(V_{j,k-1}-V_{j,k}\right)\frac{\left(\varepsilon_{j,k}+\varepsilon_{j-1,k}\right)}{(z_{j,k}-z_{j,k-1})\left(z_{j,k+1}-z_{j,k-1}\right)}+\\ &\left(V_{j,k+1}-V_{j,k}\right)\frac{\left(\varepsilon_{j-1,k-1}+\varepsilon_{j,k-1}\right)}{(z_{j,k+1}-z_{j,k})\left(z_{j,k+1}-z_{j,k-1}\right)}+\\ &\left(V_{j-1,k}-V_{j,k}\right)\frac{\left(\varepsilon_{j-1,k-1}+\varepsilon_{j-1,k}\right)}{(y_{j,k}-y_{j-1,k})\left(y_{j+1,k}-y_{j-1,k}\right)}+\end{aligned} \tag{4.35}$$

$$\left(V_{j+1,k} - V_{j,k}\right)\frac{\left(\varepsilon_{j,k-1} + \varepsilon_{j,k}\right)}{\left(y_{j+1,k} - y_{j,k}\right)\left(y_{j+1,k} - y_{j-1,k}\right)} = \rho_{j,k}$$

Equation (4.35) can be rewritten as a coefficient expression

$$A_{j,k}V_{j-1,k} + B_{j,k}V_{j,k-1} + C_{j,k}V_{j,k} + D_{j,k}V_{j,k+1} + E_{j,k}V_{j+1,k} = \rho_{i,j} \tag{4.36}$$

Where

$$A_{j,k} = \frac{\left(\varepsilon_{j-1,k-1} + \varepsilon_{j-1,k}\right)}{\left(y_{j,k} - y_{j-1,k}\right)\left(y_{j+1,k} - y_{j-1,k}\right)}$$

$$B_{j,k} = \frac{\left(\varepsilon_{j,k} + \varepsilon_{j-1,k}\right)}{\left(x_{j,k} - x_{j,k-1}\right)\left(x_{j,k+1} - x_{j,k-1}\right)}$$

$$D_{j,k} = \frac{\left(\varepsilon_{j-1,k-1} + \varepsilon_{j,k-1}\right)}{\left(x_{j,k+1} - x_{j,k}\right)\left(x_{j,k+1} - x_{j,k-1}\right)} \tag{4.37}$$

$$E_{j,k} = \frac{\left(\varepsilon_{j,k-1} + \varepsilon_{j,k}\right)}{\left(y_{j+1,k} - y_{j,k}\right)\left(y_{j+1,k} - y_{j-1,k}\right)}$$

$$C_{j,k} = -\left(A_{j,k} + B_{j,k} + D_{j,k} + E_{j,k}\right)$$

Poisson's equation must be linearized to be solved numerically. Considering that Poisson's equation is solved iteratively, the potential of the new iteration (V^{new}) can be described as the sum of the potential of the previous iteration (V^{old}) and a small update (δ). Thus, Poisson's equation can be rewritten as

$$\nabla \cdot \left(\varepsilon \nabla V^{old}\right) + \nabla \cdot (\varepsilon \nabla \delta) = \rho^{new} \tag{4.38}$$

In which ρ^{new} is the charge density in the new iteration. It can be linearly approximated using Taylor series, resulting in

$$\rho^{new} = \rho^{old} + \frac{q^2}{k_B T}\left(n^{old} + p^{old}\right)\delta \tag{4.39}$$

After substituting (4.39) into (4.38) and rearranging the terms, the final differential equation that needs to be solved is given by

$$\nabla \cdot (\varepsilon \nabla \delta) - \frac{q^2}{k_B T} \left(n^{old} + p^{old}\right)\delta = \rho^{old} - \nabla \cdot \left(\varepsilon \nabla V^{old}\right) \tag{4.40}$$

Equation (4.40) is solved in terms of δ. The derivatives terms of equation (4.40) must be substituted by their discrete form. Besides, the coefficient $C_{j,k}$ of $\nabla \cdot (\varepsilon \nabla \delta)$ must be rewritten to incorporate the second term on the left-hand side of equation (4.40), resulting in

$$C_{j,k} = -(A_{j,k} + B_{j,k} + D_{j,k} + E_{j,k}) - \frac{q^2}{k_B T} \left(n^{old} + p^{old}\right) \tag{4.41}$$

This system of linear equations is solved by employing the Portable, Extensible Toolkit for Scientific Computation (PETSc) (BALAY, 2020) package.

4.1.3 Solving Poisson and Schrödinger Equations Self-consistently

The confinement potential in the Hamiltonian comes from the solution of Poisson's equation, while the electron density necessary to solve Poisson's equation comes from the solution of the Schrödinger equation. Therefore, Poisson's equation and the Schrödinger equation must be solved self-consistently until the results converge.

During the Schrödinger-Poisson loop, when the Poisson and Schrödinger equations are solved self-consistently, the electron density is given by the quantum electron density (equation (4.28)). Therefore, to solve Schrödinger and Poisson's equation self-consistently, Poisson's equation must be linearized taking into account the quantum electron density.

$$\nabla \cdot \left(\varepsilon \nabla V^{old}\right) + \nabla \cdot (\varepsilon \nabla \delta) = \rho^{new} \tag{4.42}$$

where V^{old} is the potential of the previous iteration and δ is a small update. To linearize Poisson's equation (equation (4.42)), we have to take into account the quantum electron density in ρ^{new}. Thus, ρ^{new}can be linearly approximated using Taylor series, resulting in

$$\rho^{new} = \rho^{old} + \left.\frac{\partial \rho^{new}}{\partial V^{new}}\right|_{V^{old}} \delta \tag{4.43}$$

Considering that the density of holes is given by the Boltzmann approximation

$$\left.\frac{\partial \rho^{new}}{\partial V^{new}}\right|_{V^{old}} = -q^2\left(-\frac{p^{old}}{k_B T} - \left.\frac{\partial n^{new}}{\partial V^{new}}\right|_{V^{old}}\right) \quad (4.44)$$

Since the density of electrons is calculated using equation (4.28), the calculation of $\left.\frac{\partial n^{new}}{\partial V^{new}}\right|_{V^{old}}$ is not straightforward. The final expression used in the simulator is given in equation (4.45). A detailed derivation of this expression can be found in (BAIKADI, 2020).

$$\left.\frac{\partial n^{new}}{\partial V^{new}}\right|_{V^{old}} = \frac{q n_Q^{old}}{k_B T} \quad (4.45)$$

Where

$$n_Q^{old} = \frac{\sqrt{2 m_z K_B T}}{\pi \hbar} 2 \sum_{n,\nu} \frac{F_{-1/2}\left(\eta_{old}^{n,\nu} + h\right) - F_{-1/2}\left(\eta_{old}^{n,\nu}\right)}{h} \left|\psi_{old}^{n,\nu}(x,y)\right|^2 \quad (4.46)$$

In which h is equal to $\frac{\eta_{old}^{n,\nu}}{100}$

Substituting equation (4.46) into equation (4.45) results in

$$\left.\frac{\partial \rho^{new}}{\partial V^{new}}\right|_{V^{old}} = q^2\left(\frac{p^{old}}{k_B T} + \frac{n_Q^{old}}{k_B T}\right) \quad (4.47)$$

Now substituting equation (4.47) into equation (4.44) results in

$$\rho^{new} = \rho^{old} + q^2\left(\frac{p^{old}}{k_B T} + \frac{n_Q^{old}}{k_B T}\right)\delta \quad (4.48)$$

Thus, the final expression of Poisson's equation coupled to the Schrödinger equation is given by

$$\nabla \cdot (\varepsilon \nabla \delta) - q^2\left(\frac{p^{old}}{k_B T} + \frac{n_Q^{old}}{k_B T}\right)\delta = \rho^{old} - \nabla \cdot \left(\varepsilon \nabla V^{old}\right) \quad (4.49)$$

To solve it numerically, the derivatives terms of equation (4.49) must be substituted by their discrete form. Besides that, the coefficient $C_{j,k}$ of $\nabla \cdot (\varepsilon \nabla \delta)$ incorporates the second term on the left-side hand of equation (4.49).

4.1.4 The Flowchart of a 2D Schrödinger-Poisson Solver

The 2D Schrödinger-Poisson solver employed in this work is written in FORTRAN 90 language. Poisson's equation is linearized and discretized, forming a system of linear equations, which is solved by employing the Portable, Extensible Toolkit for Scientific Computation (PETSc) (BALAY, 2020) package. While the eigenvalue problem that comes from the discretized Schrödinger equation is solved using the Scalable Library for Eigenvalue Problem Computation (SLEPc) (ROMAN; CAMPOS; ROMERO; TOMAS, 2015) eigenvalue solver package.

The flowchart of the Schrödinger-Poisson solver is presented in Figure 4.5.

Figure 4.5: Flowchart of the Schrödinger-Poisson solver

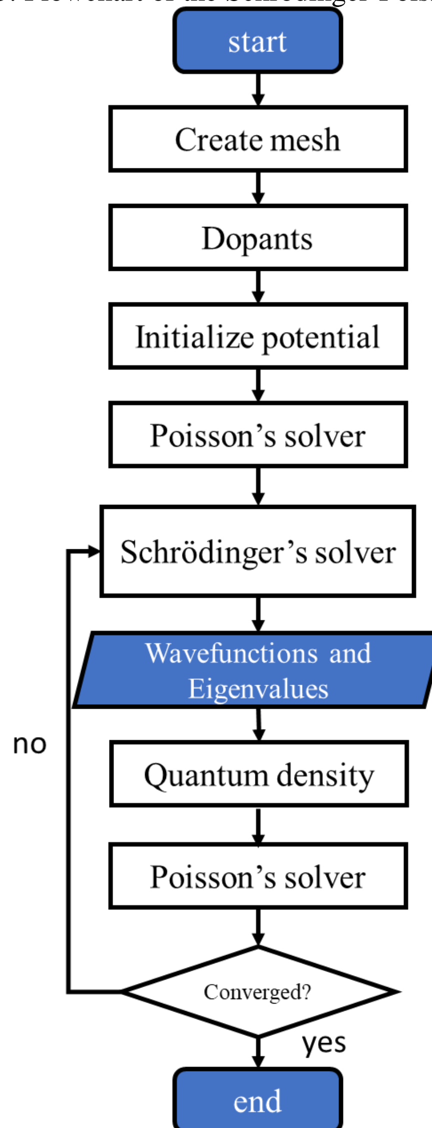

Source: Elaborated by the author.

In this work, the original code (BAIKADI, 2020) was adapted to simulate the devices of interest: Si n-type FinFET and nanowire transistor. From seventeen subroutines, sixteen were modified to take into account these new devices. Although Poisson's equation is solved at the entire device, the Schrödinger equation is solved only in the confinement region.

The Schrödinger-Poisson solver consists of:

1. Creating the mesh.
2. Assigning the dopants to each region of the device.
3. Initializing the potential based on charge neutrality.
4. Calculating the coefficients of Poisson's equation.
5. Solving Poisson's equation using the initial potential calculated in (3) as the initial guess and calculating the hole and electron density assuming Boltzmann approximation.

Finally, the program enters the Schrödinger-Poisson loop, which consists of the following steps:

a. Solving the Schrödinger equation using the conduction band calculated obtained by the Poisson solver as the confinement potential.
b. Calculating the quantum density of the electron using the eigenvalues and the wavefunctions.
c. Calculating the coefficients of Poisson's equation and solving Poisson's equation in the Schrödinger domain using the quantum electron density. For the other regions of the device, the electrostatic potential is not updated.
d. Comparing the potential calculated in the previous iteration and the new potential calculated in (c). If the difference between them is smaller than 10^{-6} V the results converged. Otherwise, go to step (a) until the results converge.

Thus, Schrödinger and Poisson's equations are self-consistently solved.

4.2 2D Effective Potential-Poisson solver

To obtain the smoothing parameters of the Effective Potential that lead to an electron line density that most agrees with the one calculated by the Schrödinger-Poisson solver, the Effective Potential equation was coupled to the Poisson solver that was described in Section 4.1.2.

The flowchart of the solver is depicted in Figure 4.6. The initialization step creates the mesh of the device, assigns the dopant's charge to each mesh node, and initializes the potential at each mesh node based on the charge neutrality of the device. In addition, the coefficients of the Effective Potential are also calculated in the initialization.

Figure 4.6: Flowchart of the Effective Potential-Poisson solver.

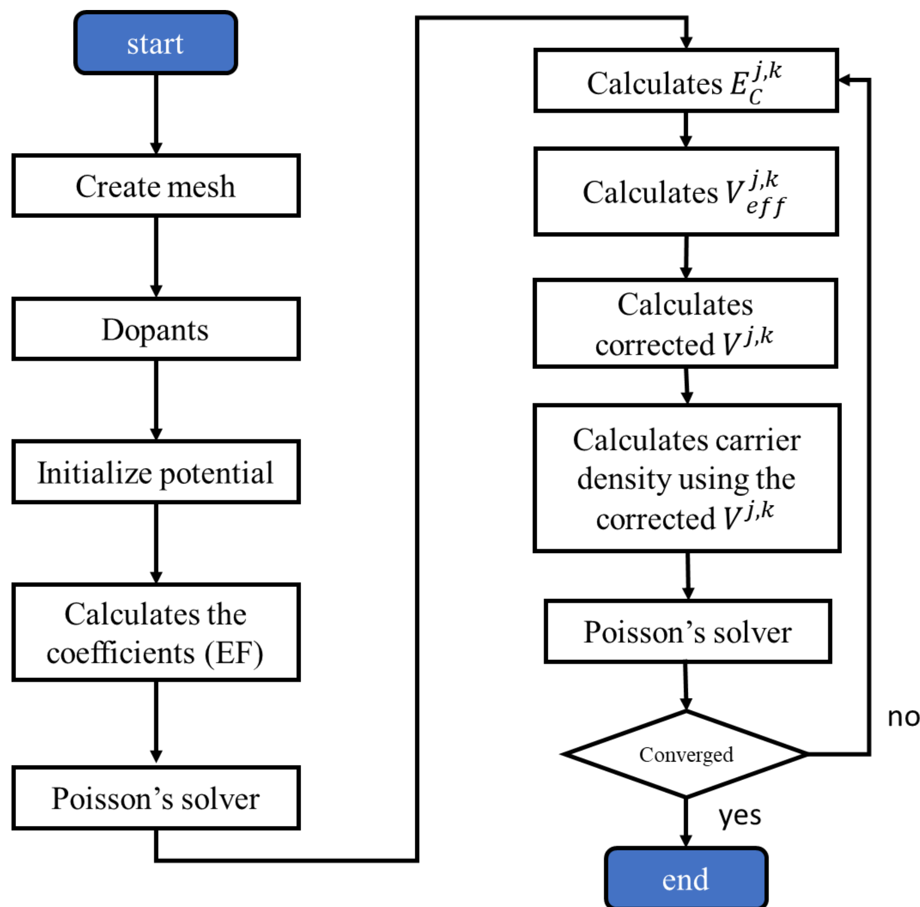

Source: Elaborated by the author.

When the initialization ends, the code enters the Effective Potential-Poisson solver loop. In the first iteration, the first potential guess in the Poisson solver is the initial potential – which is the potential that assures charge neutrality. The other inputs of the Poisson solver are the density of dopants and the density of carriers calculated using the initial potential. To solve Poisson equation, the coefficients of the discrete Poisson's equations are calculated. The output

of Poisson solver is the Hartree potential $V_{j,k}$. Using the updated potential, the conduction band at the point j,k is calculated using equation (4.50)

$$E_C^{j,k} = \chi^{si} + \frac{k_B T}{q} ln\left(\frac{N_c}{n_i}\right) - qV_{j,k} - \chi^{j,k} \quad (4.50)$$

where j and k represent the height and width directions of the device. χ^{si} is the electron affinity of silicon, N_c is the effective density of states of silicon conduction's band, and $\chi^{j,k}$ is the electron affinity at the mesh point j,k. In equation (4.50), the expression $\frac{k_B T}{q} ln\left(\frac{N_c}{n_i}\right)$ is equal to $E_C - E_i$ (which is the conduction band edge minus the intrinsic Fermi level of silicon).

After that, the Effective Potential is calculated by convoluting the conduction band (equation (4.50)) with the Gaussian-wave packet using equation (4.51), which is a 2D version of equation (3.20).

$$V_{eff}^{j,k} = \frac{1}{2\pi\sigma_y\sigma_z} \sum_{m,n} \left(E_C^{j,k} I_{j,k,m,n}^1 + \left(E_C^{m,k} - E_C^{j,k}\right) I_{j,k,m,n}^2 + \left(E_C^{j,n} - E_C^{j,k}\right) I_{j,k,m,n}^3\right) \quad (4.51)$$

where

$$I_{j,k,m,n}^1 = \left(\frac{\sqrt{2}\sqrt{\pi}}{2}\right)^2 \sigma_z\sigma_y \left[erf\left(\frac{z_{fin} - z_k}{\sqrt{2}\sigma_k}\right) - erf\left(\frac{z_{init} - z_k}{\sqrt{2}\sigma_k}\right)\right]\left[erf\left(\frac{y_{fin} - y_j}{\sqrt{2}\sigma_y}\right) - erf\left(\frac{y_{init} - y_j}{\sqrt{2}\sigma_y}\right)\right] \quad (4.52)$$

$$I_{j,k,l,m}^2 = \frac{1}{\Delta_y} {\sigma_y}^2 \left[\exp\left(-\frac{\left(y_{init} - y_j\right)^2}{2{\sigma_y}^2}\right) - \exp\left(-\frac{\left(y_{fin} - y_j\right)^2}{2{\sigma_y}^2}\right)\right] \sigma_z \frac{\sqrt{2}\sqrt{\pi}}{2}\left[erf\left(\frac{z_{fin} - z_k}{\sqrt{2}\sigma_z}\right) - erf\left(\frac{z_{init} - z_k}{\sqrt{2}\sigma_z}\right)\right] \quad (4.53)$$

$$I_{j,k,l,m}^3 = \frac{1}{\Delta_z} {\sigma_z}^2 \left[\exp\left(-\frac{\left(z_{init} - z_k\right)^2}{2{\sigma_z}^2}\right) - \exp\left(-\frac{\left(z_{fin} - z_k\right)^2}{2{\sigma_z}^2}\right)\right] \sigma_y \frac{\sqrt{2}\sqrt{\pi}}{2}\left[erf\left(\frac{y_{fin} - y_j}{\sqrt{2}\sigma_z}\right) - erf\left(\frac{y_{init} - y_j}{\sqrt{2}\sigma_z}\right)\right] \quad (4.54)$$

The corrected electrostatic potential is then calculated using the Effective Potential, as it is expressed in equation (4.55).

$$V_{j,k} = q\left(-V_{eff}^{j,k} + \chi^{si} + \frac{k_B T}{q} ln\left(\frac{N_c}{n_i}\right) - \chi^{j,k}\right) \tag{4.55}$$

Finally, the electron and hole density are calculated using equations (4.56) and (4.57).

$$n_{j,k} = n_i \exp\left(\frac{qV_{j,k}}{k_B T}\right) \tag{4.56}$$

$$p_{j,k} = n_i \exp\left(-\frac{qV_{j,k}}{k_B T}\right) \tag{4.57}$$

In the next iteration, the electron and hole density calculated using the Effective Potential, and the Hartree potential calculated at the beginning of the loop will be the inputs of Poisson's equation solver. The Effective Potential-Poisson solver loop continues until the results converge, which is achieved when the difference between the new potential and the old potential is smaller than the convergence criterion (10^{-6} V).

4.3 Results of the Effective Potential-Poisson Solver and Schrödinger-Poisson Solver

The width and the height of the FinFET investigated in this work are 8 nm and 42 nm, respectively, and the equivalent oxide thickness (EOT) is 1.2 nm. TiN was employed as the metal gate, assuming a work function equal to 4.6 eV. The doping density is $N_A = 1 \times 10^{15}$ cm^{-3}. Since the FinFET has two side gates, the total width of the structure is 10.4 nm. Taking into account the silicon substrate below the Fin and the top gate, the total height of the structure is 57.2 nm. As mentioned before, here the cross-section along the width and height of the device is being simulated; therefore, the length of the transistors is not considered in this section.

Figure 4.7 shows the classical electron density of electrons in the FinFET device when the gate bias (V_G) is equal to 1V. As can be observed in Figure 4.7, the inversion layer in the classical description is formed at the silicon dioxide/silicon interface.

Figure 4.7: Electron density calculated classically (using only Poisson solver). $V_G = 1$ V.

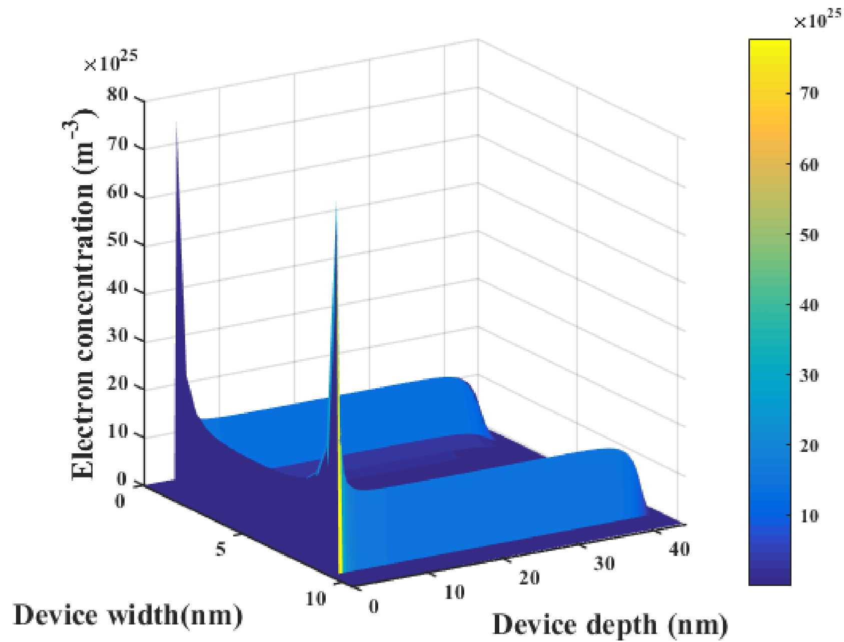

Source: Elaborated by the author.

Figure 4.8: Electron density calculated using the 2D Effective Potential-Poisson solver. $V_G = 1$ V.

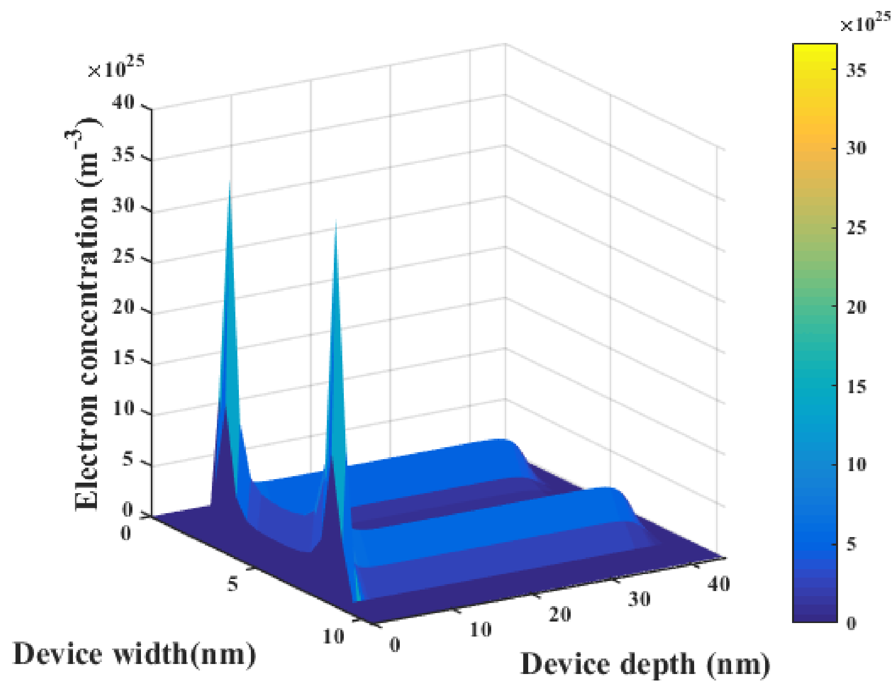

Source: Elaborated by the author.

Figure 4.8 and Figure 4.9 depict the electron density in the FinFET calculated using the 2D Effective-Potential-Poisson solver and the 2D Schrödinger-Poisson solver, respectively when the gate bias is equal to 1 V. In both figures, one can observe that the electron density is

setback from the silicon/silicon dioxide interface, demonstrating the impact of the quantum confinement on the distribution of electrons in the channel. Comparing Figure 4.8 and Figure 4.9, the Effective Potential model can describe the setback of the electrons, effect known as volume inversion. In addition, comparing the classical (Figure 4.7) with the Effective Potential (Figure 4.8) results, the electron density calculated using the Effective Potential is smoothed.

Figure 4.9: Electron density calculated using the 2D Schrödinger-Poisson solver. $V_G = 1$ V.

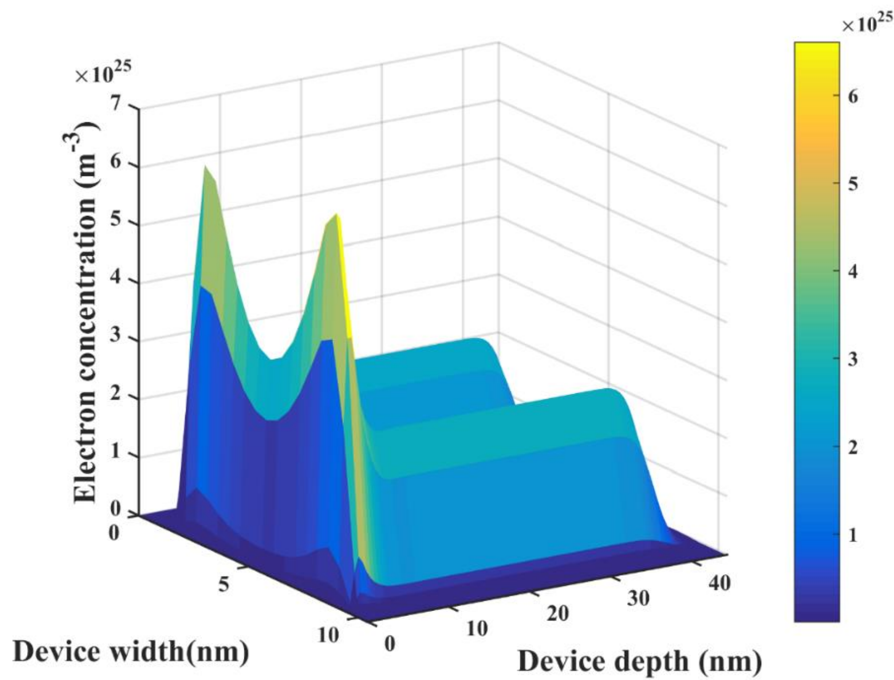

Source: Elaborated by the author.

.

Besides evaluating the impact of the quantum confinement on the position of electrons in the channel, we also investigated qualitatively the impact of the quantum confinement on the electron density. Figure 4.10 depicts the line density of electrons in the FinFET calculated classically, using the Effective Potential-Poisson solver, and the Schrödinger-Poisson solver described in this work. For the FinFET of interest, using a smoothing parameter of the Effective Potential model equal to 0.45 nm generates the line density that best agrees with the Schrödinger-Poisson results.

Figure 4.10: Line density of the electrons in the FinFET as a function of the gate bias calculated using the semiclassical model (blue curve), the Effective Potential solver (red curve), and the Schrödinger-Poisson solver (black curve).

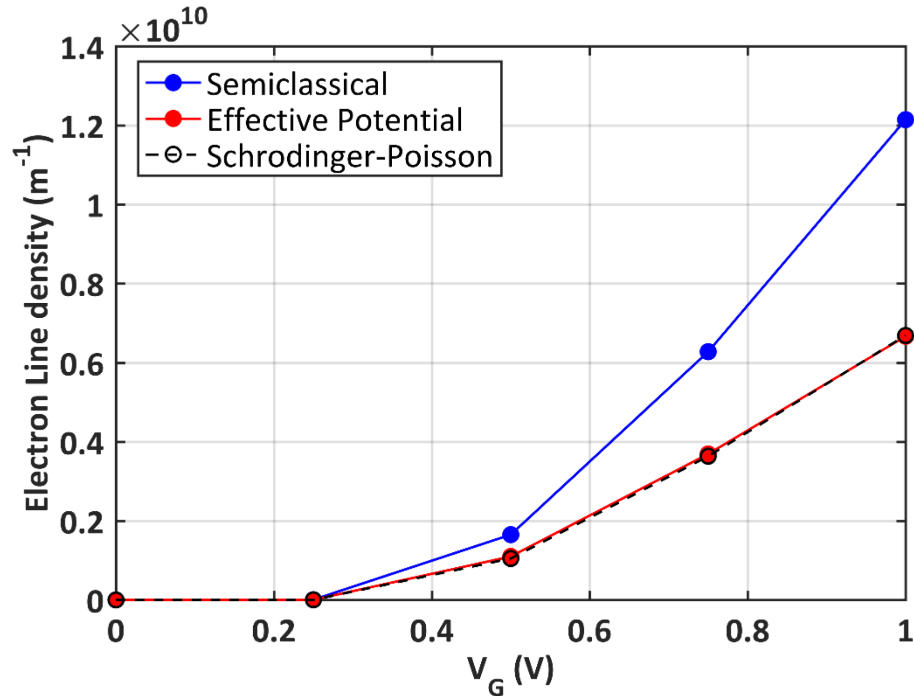

Source: Elaborated by the author.

The silicon nanowire investigated in this work has a width and height equal to 10 nm, and an EOT of 1.3nm. The work function of the metal is 4.52 eV. The thickness of the buried silicon dioxide layer is 150 nm. The doping density is assumed to be $N_A = 1 \times 10^{15}$ cm^{-3}.

Figure 4.11 shows the line density of electrons in the silicon nanowire transistor calculated semiclassically, using the Effective Potential-Poisson solver, and using the Schrödinger-Poisson solver. For the silicon nanowire transistor, the best agreement between the line density calculated using the Effective Potential-Poisson solver and the Schrödinger-Poisson solver was obtained by employing a smoothing parameter equal to 0.4 nm. From Figure 4.10 and Figure 4.11, we can also observe that the semiclassical model overestimates the line density. Thus, the semiclassical model might misrepresent the drain current of these nanoscale devices.

Figure 4.11: Line density of the electrons in the nanowire transistor as a function of the gate bias calculated using the semiclassical model (blue curve), the Effective Potential solver (red curve), and the Schrödinger-Poisson solver (black curve).

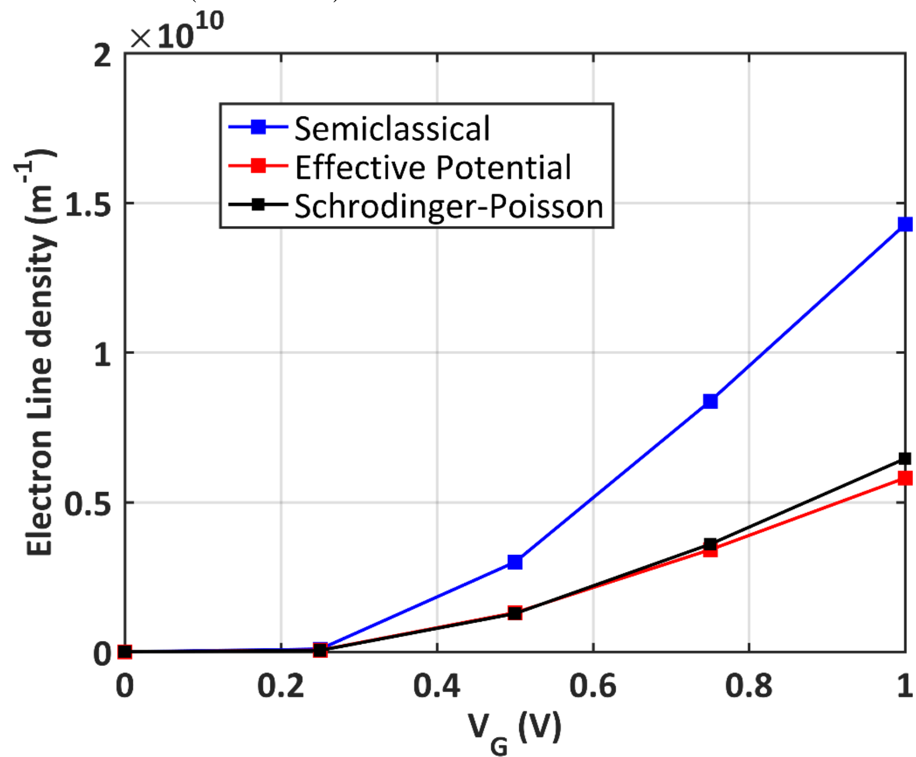

Source: Elaborated by the author.

Figure 4.12: Potential energy calculated classically and by the Effective Potential-Poisson solver. Using $V_G = 1$ V.

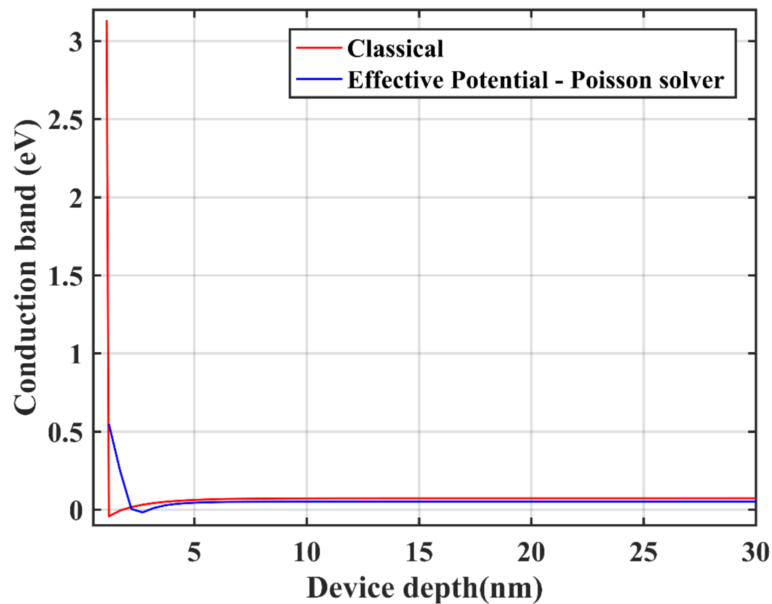

Source: Elaborated by the author.

Figure 4.12 shows the difference between the conduction band of the FinFET device calculated by the classical and Effective Potential model when the gate bias is equal to 1V. The

minimum of the classical conduction band occurs at the silicon/silicon dioxide interface. Because of that, the density of electrons is maximum at this interface. However, the minimum of the conduction band in the Effective Potential model occurs a few nanometers away from this interface, resulting in volume inversion. Besides, the minimum of the conduction band in the Effective Potential model is higher in energy than the minimum of the classical model. Because of that, the electron density in the Effective Potential model is smoothed in comparison with the classical electron density.

For these two devices, there is a great agreement between the electron line density calculated by the Effective Potential and the one calculated by the Schrödinger solver in the entire range of gate bias simulated. The smoothing parameter of the FinFET device investigated here is 0.45 nm and the smoothing parameter of the silicon nanowire investigated here is 0.4 nm. These results show that the Effective Potential approach represents the effect of quantum confinement. Thus, the Effective Potential approach is an adequate quantum correction to the Monte Carlo device simulator of these tri-gate transistors. When employing the Effective Potential approach as a quantum correction, the electrons can still be treated as particles that are subjected to the Effective Potential.

5 DEVICE SIMULATOR WITH EFFECTIVE POTENTIAL AS QUANTUM CORRECTION

When employing the Effective Potential in the device simulator as quantum correction, the electron's size is incorporated by the Effective Potential. Thus, the electron is modeled as a zero-size particle that is exposed to the Effective Potential instead of being exposed to the Hartree potential. The flowchart of the quantum-corrected atomistic device simulator is shown in Figure 5.1, and the two new routines included in the simulator to perform the quantum correction are represented by red rectangles.

Figure 5.1: Flowchart of the quantum-corrected MC device simulator.

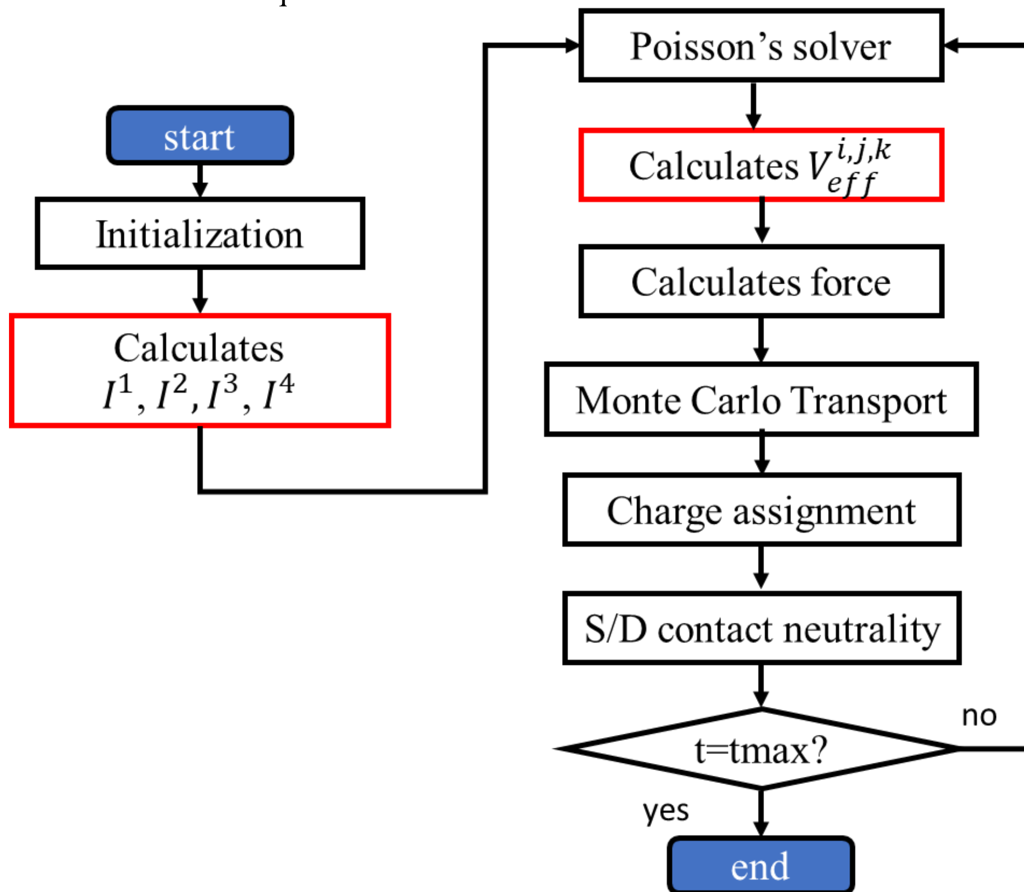

Source: Elaborated by the author.

One of these routines concerns calculating and storing the coefficients of the Effective Potential $I^1_{i,j,k,l,m,n}$, $I^2_{i,j,k,l,m,n}$, $I^3_{i,j,k,l,m,n}$ and $I^4_{i,j,k,l,m,n}$ (described by equations (3.21), (3.22), (3.23), and (3.24)). Since these coefficients depend only on the distance between the mesh nodes, they are calculated at the initialization process rather than being calculated at every

Monte Carlo – Poisson iteration. The other routine concerns calculating the Effective Potential at each mesh point using equation (3.20). Note that, the Effective Potential is calculated at each observation time only in the region where the confinement occurs. In n-type FinFET and nanowire transistors, it occurs in the channel.

As it is depicted in Figure 5.1, the first step of the simulation is the initialization, where the structure of the transistor is defined, the boundary conditions are set, the mesh is created, the electrons are initialized, and the dopants are distributed following the doping density of each region. The doping profile can be uniform or non-uniform, where the dopants are treated as discrete particles, which leads to a more realistic representation of the device, enabling the random dopant fluctuation to be investigated. As mentioned above, the coefficients of the Effective Potential are also calculated in the initialization. So, the difference between the initialization process of a semiclassical simulator (described in Section 2.4) and the initialization process of the quantum-corrected simulator presented in this work is the calculation of the Effective Potential coefficients.

After the initialization process ends, the simulation enters the Monte Carlo – Poisson iteration loop where the dynamics of all electrons are evaluated at multiples of observation time until the final simulation time is reached. The first step of this loop iteration is assigning the charge of electrons to the nearby mesh nodes and then solving Poisson's equation. After Poisson's equation is solved, the conduction band is calculated using equation (5.1).

$$E_C{}^{i,j,k} = \chi^{si} + (E_C - E_i) - qV_{i,j,k} - \chi^{i,j,k} \tag{5.1}$$

Then, the Effective Potential is calculated in the new routine employing the expression given by equation (3.20). The input of this routine is the conduction band calculated using equation (5.1), while its output is the Effective Potential $V_{eff}^{i,j,k}$.

The electric field at each mesh node can be calculated as the gradient of the Effective Potential, using:

$$\mathbf{E} = \nabla V_{eff}^{i,j,k} \tag{5.2}$$

The electrostatic force that acts upon the electrons is calculated by interpolating the mesh forces of the cell where the electron is located using the CIC method. Note that outside the quantum confinement regions, the mesh force and the density of holes are calculated using the Hartree potential calculated by Poisson's solver.

Then, the transport of the electrons is simulated using the Monte Carlo transport simulation method. After simulating the transport of all electrons in the device, the transport boundary conditions are verified to model the physical boundaries correctly. After that, the charge neutrality in the vicinity of the drain and source contacts is verified. Electrons can be added or deleted to balance the charge in these regions, assuring that the source and drain contacts are being correctly modeled as ohmic contacts. The current that flows through the channel at the observation time is then calculated.

In summary, in the Monte Carlo – Poisson iteration loop, the input data of the Poisson solver is the charge density at each mesh node calculated after evaluating the electron's transport during an observation time. The output of the Poisson solver is the Hartree potential that will be employed to calculate the Effective Potential, which will accelerate the electrons in the next observation time. The next iteration is started unless the simulation has reached the final time.

6 RESULTS OF THE N-TYPE FINFET

The n-type FinFET simulated in this chapter has the same physical parameters as the one simulated in Section 4.3. Hence, the smoothing parameter of the Effective Potential (σ) of this device is 0.45 nm. Figure 6.1 depicts the 3D schematic of the FinFET investigated. The width and the height of the FinFET are 8 nm and 42 nm, respectively, and the EOT is 1.2 nm. The total height of the structure is 57.2 nm, and the total width is 10.4 nm. The metal gate is TiN (assuming its work function is 4.6 eV). The source and drain regions were doped with donor dopants, using a doping density of $N_D = 5 \times 10^{19}$ cm^{-3}. The length of the channel is 18 nm, and its doping density is $N_A = 1 \times 10^{15}$ cm^{-3}.

Figure 6.1: Schematic of the FinFET investigated in this work. The silicon regions are in blue, the silicon oxide region in gray, and the gate dielectric in light gray. The gate metal is represented in red. The region referred to as S represents the source, G represents the gate and D represents the drain. W_{fin} and H_{fin} represent the fin width and height respectively, and L represents the channel length.

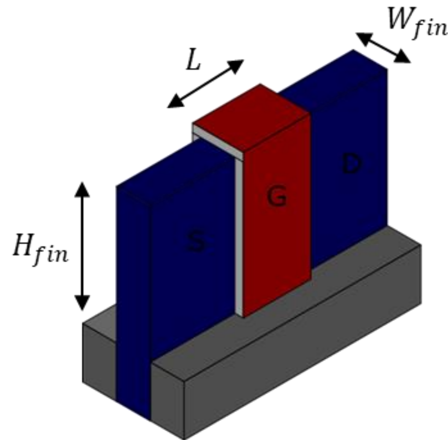

Source: Elaborated by the author.

The semiclassical device simulator for the FinFET device was developed by Furtado (2021). To compare the semiclassical model and the quantum-corrected model, we have simulated the FinFET device using the semiclassical and the quantum-corrected simulators. To consider the quantum confinement along the device's height and width, the mesh spacing along these directions was set to 0.5 nm. Considering that there is no charge confinement along the length of the device, the mesh spacing employed in this direction was 2 nm. Using these mesh spacings, the observation time equal to 0.01 fs led to good coupling of the Poisson solver and the Monte Carlo transport simulation. Following (BUFLER; SMITH, 2013), the specular scattering probability was set to 85%, thus the diffuse probability was set to 15%. Although the

quantum confinement is only depicted in the quantum-corrected simulation, the same mesh spacing and observation time were employed in the classical simulation, so the only difference between the results is related to the quantum correction.

To estimate the average characteristics of the device, the simulation must first reach a steady-state condition. After the steady-state condition is achieved, the simulation must be run for a couple of picoseconds to obtain sufficient data to estimate the average characteristics of the device. For this transistor, the total time of the simulation was set to 10 ps. The data used to estimate the average properties of the device was collected from 3 ps to 10 ps.

Figure 6.2 shows the cumulative charge that flows in the source and drain contact as a function of time. Thus, the curves in Figure 6.2 represent the net charge that enters and exits the source and drain contact. The drain and the gate biases were equal to 1 V, while the back and source contact were set to 0 V. The current of the device can be estimated by extrapolating the slope of these curves. These curves must be parallel to each other, otherwise, the source and drain contacts are not being modeled correctly.

Figure 6.2: Cumulative charge as a function of the time through the source and drain contact with V_{DS}=1.0 V, V_{GS} = 0.8 V, and V_{BS} = 0 V.

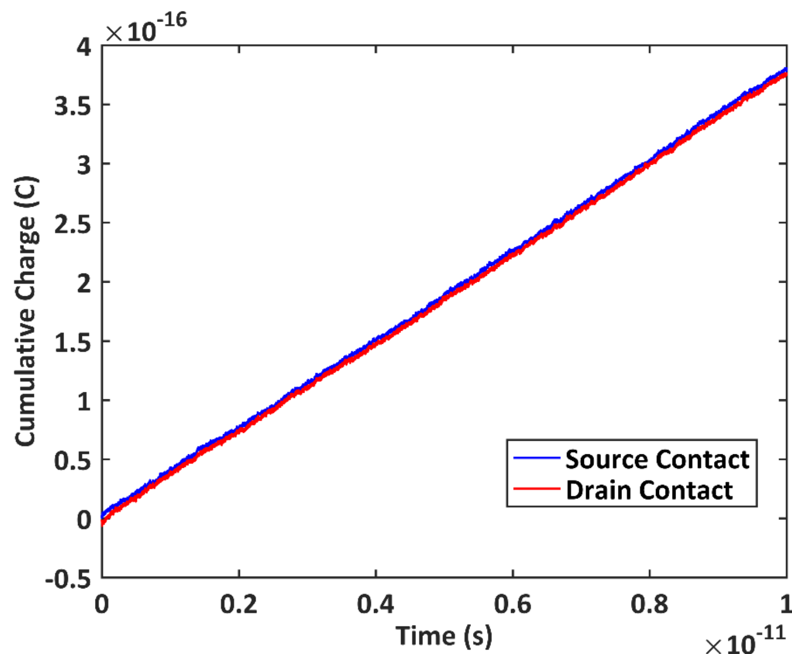

Source: The author.

Ten different samples of the same FinFET were investigated. These ten devices have the same physical parameters; however, each device presents a distinct spatial distribution of

dopant and distinct number of dopants. Those devices were investigated using the semiclassical and the quantum-corrected simulators.

Figure 6.3 and Figure 6.4 show the conduction band profile for a given dopant distribution along the height and length of the n-FinFET taken at the center of the fin width obtained, respectively, by the semiclassical and quantum-corrected simulators.

Figure 6.3: Conduction band taken at the middle of the FinFET width calculated using the semiclassical simulator. $V_{DS} = 0.2$ V, $V_{GS} = 0.8$ V and $V_{BS} = 0$ V.

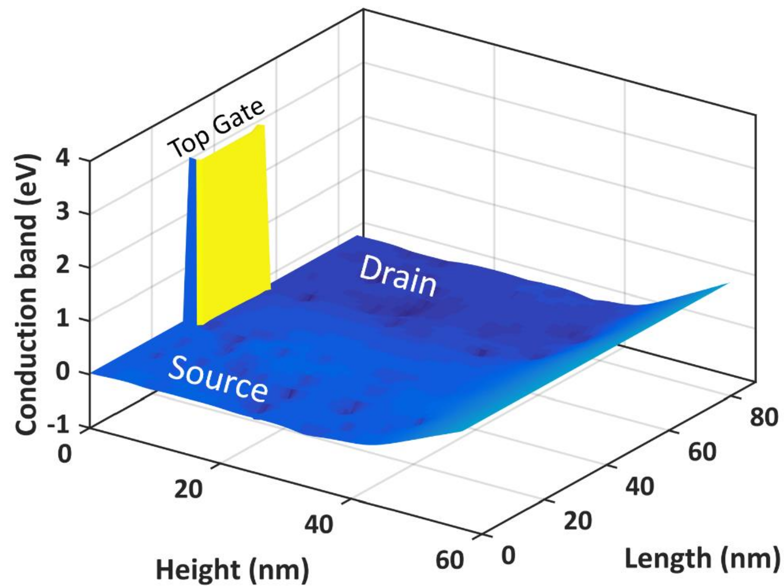

Source: Elaborated by the author.

Figure 6.4: Conduction band taken at the middle of the FinFET width calculated using the quantum-corrected simulator. The circle in red indicates the region where the conduction band is smoothed. $V_{DS} = 0.2$ V, $V_{GS} = 0.8$ V and $V_{BS} = 0$ V.

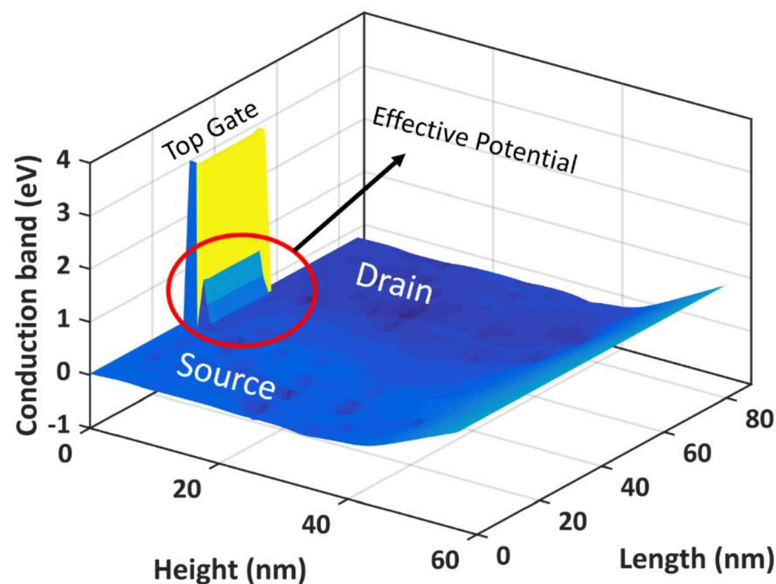

Source: Elaborated by the author.

In both simulators, the discrete behavior of dopants can be observed in the source and doping regions. The conduction band calculated using the quantum-corrected simulator shows a smoothed profile close to the silicon/silicon dioxide interface (encircled in Figure 6.4) when compared to the semiclassical conduction band. The smoothed conduction band models the effect of quantum confinement, because it reduces the electron density and places the inversion layer a few nanometers away from the silicon/silicon dioxide interface, which leads to volume inversion.

Figure 6.5 Electron density taken at a cross-section in the channel region calculated using the semiclassical simulator. $V_{DS} = 0.2$ V, $V_{GS} = 0.8$ V and $V_{BS} = 0$ V.

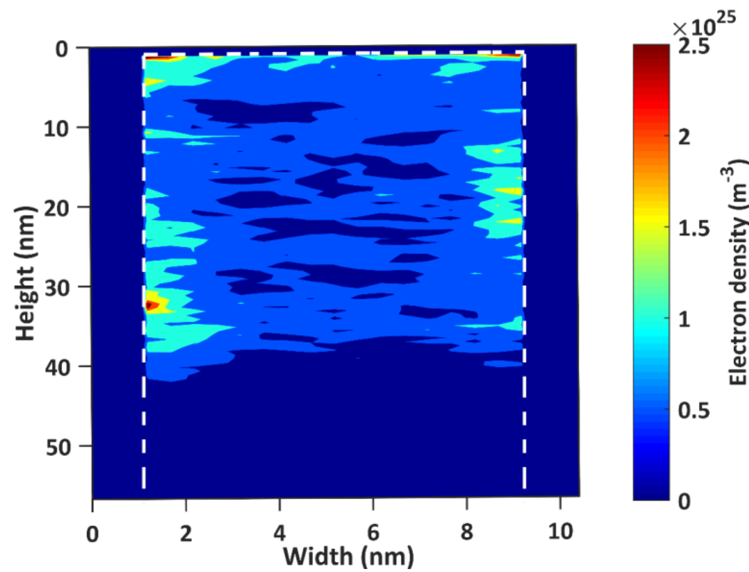

Source: Elaborated by the author.

Figure 6.6: Electron density taken at a cross-section in the channel region calculated using the quantum-corrected simulator. $V_{DS} = 0.2$ V, $V_{GS} = 0.8$ V and $V_{BS} = 0$ V.

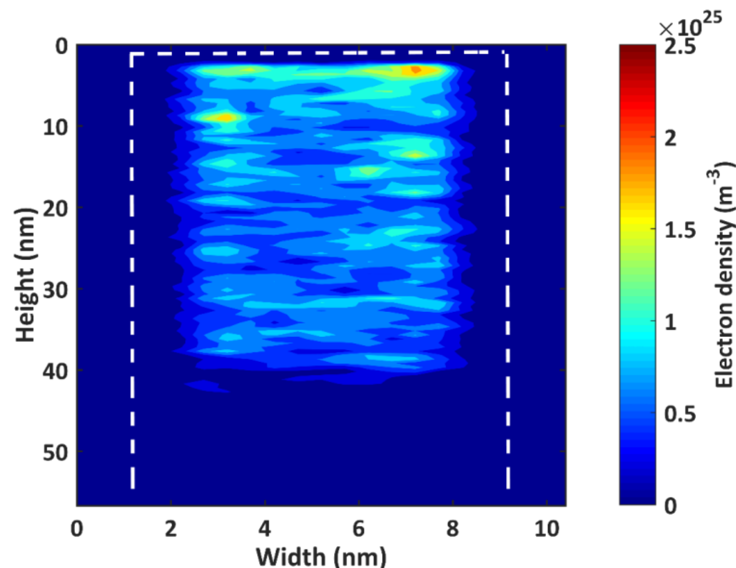

Source: Elaborated by the author.

The electron density along the fin width and height taken at a cross-section in the middle of the channel obtained by the semiclassical simulator is depicted in Figure 6.5, while the one obtained by the quantum-corrected simulator is shown in Figure 6.6. The dashed lines represent the silicon/silicon dioxide interface. In the quantum-corrected simulator (Figure 6.6), the inversion layer is formed a few nanometers away from the interface, which corroborates that volume inversion is modeled.

Figure 6.7 shows the average number of diffusive surface roughness scattering events an electron undergoes while crossing the channel as a function of the gate bias in the semiclassical and quantum-corrected simulations. The surface roughness scattering mechanism plays an important role in the semiclassical simulation, while in the quantum-corrected simulation, the probability of an electron interacting with the interface is reduced. As a result of volume inversion, the surface roughness scattering is expected to be less relevant in the quantum-corrected simulation.

Figure 6.7: Average surface roughness scattering events per electron crossing the channel in the semiclassical simulator (blue curve) and quantum-corrected simulator (red curve) for 10 samples. The error bars indicate 95% confidence interval. $V_{DS} = 0.5$ V, and $V_{BS} = 0$ V.

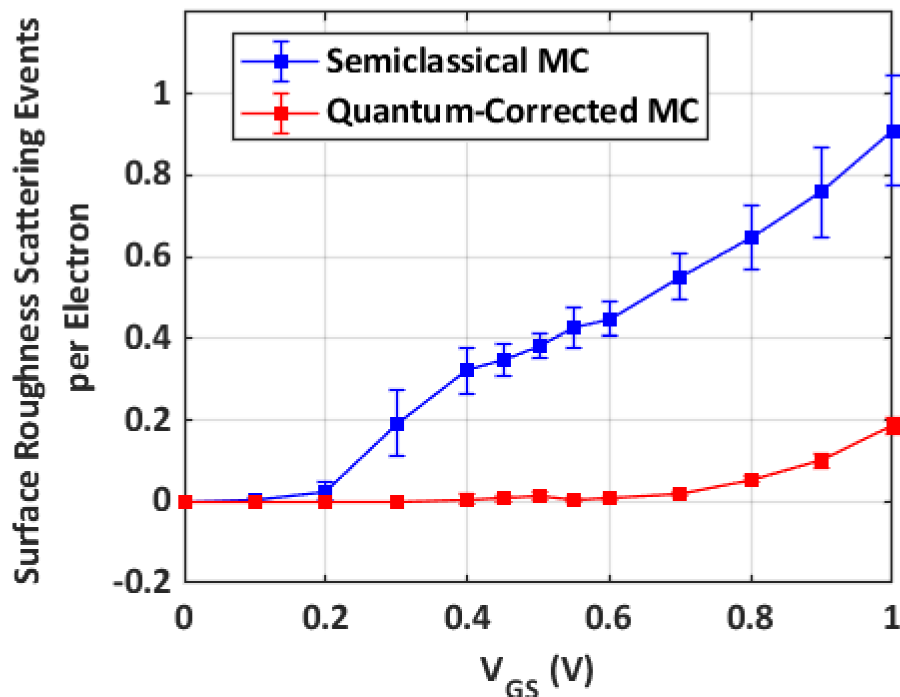

Source: Elaborated by the author.

Figure 6.8 shows the average number of phonon scatterings events an electron undergoes while crossing the channel as a function of the gate bias in the semiclassical and quantum-corrected simulations. Phonon scattering is less likely to occur in the quantum-

corrected simulation in the entire range of gate bias. In the range of gate bias simulated, the difference between the number of phonon scatterings events per electron in the semiclassical and quantum-corrected simulation reaches its peak at V_{GS} = 1 V, where the number of phonon scatterings events per electron in the quantum-corrected simulation is 28.43% smaller than the number of phonon scatterings events per electron in the semiclassical simulation. The phonon scattering is less likely to occur in the quantum-corrected simulation because the smoothing of the Effective Potential reduces the density of states by moving the ground state upwards.

Figure 6.8: Average phonon scattering events per electron crossing the channel in the semiclassical simulator (blue curve) and quantum-corrected (red) simulators for 10 samples. The error bars indicate 95% confidence interval. V_{DS} = 0.5 V, and V_{BS} = 0 V.

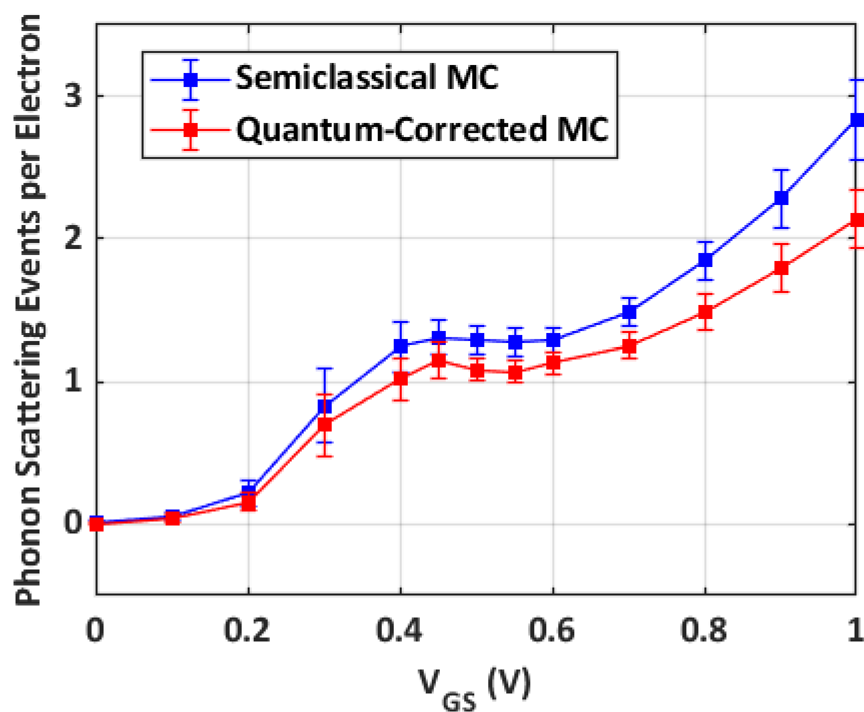

Source: Elaborated by the author.

The average electron's velocity along the length of the device estimated using the semiclassical and quantum-corrected simulator are shown in Figure 6.9. The velocity of electrons in the channel is higher in the quantum-corrected simulation than in the classical simulation. This result can be due to volume inversion (since the interaction between the electron and the interface is less likely to occur in the quantum-corrected simulation). The number of phonon-scattering events an electron undergoes while crossing the channel in the quantum-corrected simulation is also smaller than the one in the semiclassical simulation, so it might contribute to this result presented in Figure 6.9.

Figure 6.9: Average electron velocity along the device length for 10 samples. Curves estimated by the semiclassical simulator are in blue, while curves estimated by the quantum-corrected simulator are in red. The error bars indicate 95% confidence interval. $V_{BS} = 0$ V, $V_{DS} = 0.5$ V, $V_{GS} = 0.8$ V.

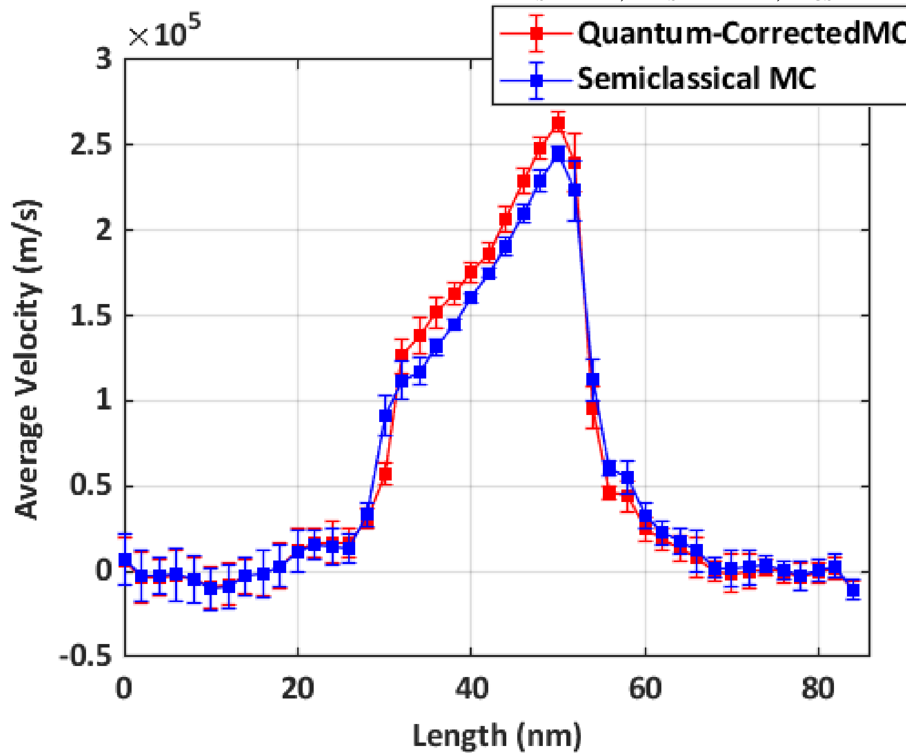

Source: Elaborated by the author.

Figure 6.10: Electron density along the device length for 10 samples. Curves estimated by the semiclassical simulator in blue, while curves estimated by the quantum-corrected simulator are in red. The error bars indicate 95% confidence interval. $V_{BS} = 0$ V, $V_{DS} = 0.5$ V, $V_{GS} = 0.8$ V.

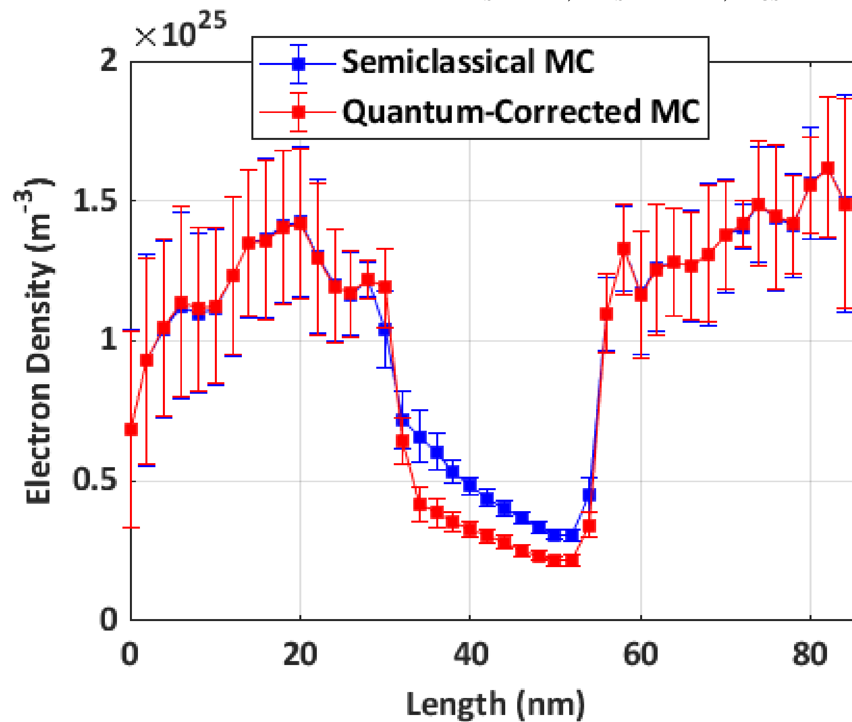

Source: Elaborated by the author.

The electron density along the length of the device estimated using the semiclassical and quantum-corrected simulators are shown in Figure 6.10. Note that in the channel, the electron density is smaller in the quantum-corrected simulation. This demonstrates that the Effective Potential is modeling the impact of quantum confinement on the density of states of electrons in the channel.

The transfer characteristic curves of the n-type FinFET studied in this work estimated by the semiclassical and quantum-corrected simulators are depicted in Figure 6.11. The quantum-corrected curve is slightly shifted in comparison to the semiclassical curve. As shown in Figure 6.11 in the weak inversion, the semiclassical conduction band is nearly flat, thus, the impact of the correction employed by the Effective Potential is small. In the strong inversion region of the transfer characteristic curves, the impact of the Effective Potential is considerable. As the gate bias increases, the conduction band bends, forming a 2D triangular well where the electrons are confined. Figure 6.11 shows that as the gate bias increases, the difference between the current obtained by the two simulators becomes more relevant.

Figure 6.11 Transfer characteristic curves estimated by the semiclassical (blue curve) and quantum-corrected (red) simulator. The curves represent the average value of the 10 samples. The error bars indicate 95% confidence interval. $V_{BS} = 0$ V, $V_{DS} = 0.5$ V.

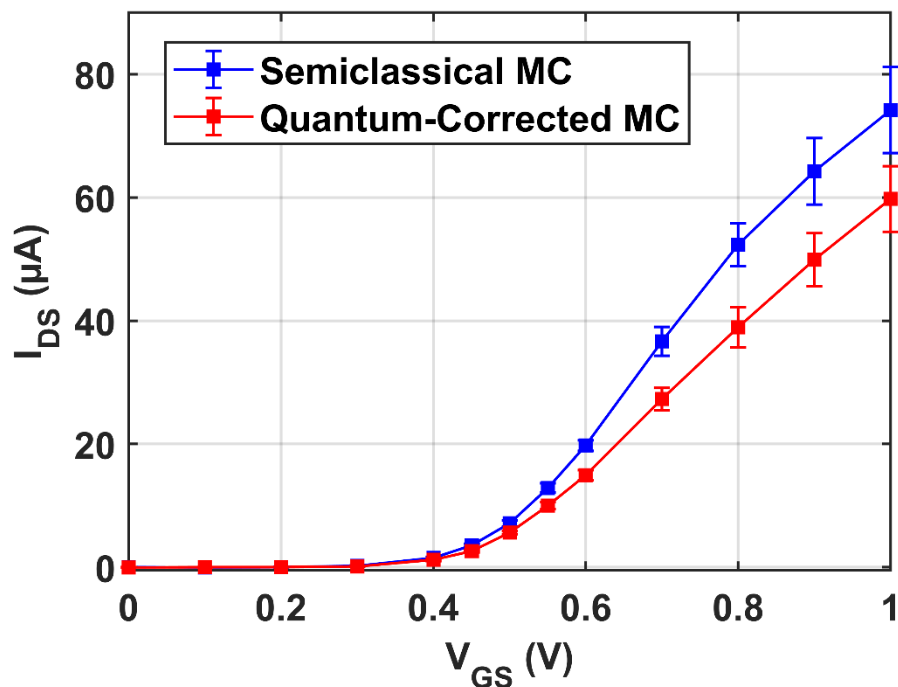

Source: Elaborated by the author.

Figure 6.12 shows the output curves estimated by both simulators. The current estimated by the semiclassical simulator is higher than the one estimated by the quantum-corrected simulator. As shown in Figure 6.9, the electron velocity is higher in the quantum-corrected simulation, which improves the output current. Nevertheless, the electron density calculated by this simulation is smaller than the one calculated by the semiclassical simulation, having an opposite effect on the current. The volume inversion reduces the surface roughness scattering events, resulting in improved electron velocity; however, the other effect of quantum confinement is the reduction of electron density, which degrades the current. Overall, the quantum confinement degrades the current of FinFET.

Figure 6.12 Output curves estimated by the semiclassical (blue) and quantum-corrected (red) simulators. The curves represent the average value of the 10 samples. The error bars indicate 95% confidence interval. $V_{BS} = 0$ V, $V_{GS} = 0.8$V.

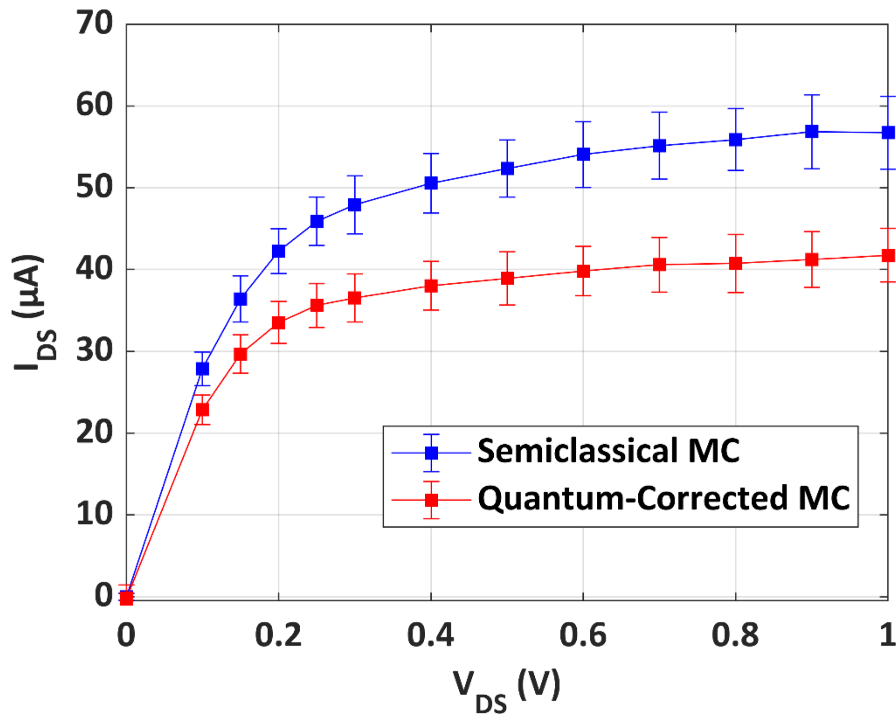

Source: Elaborated by the author.

7 RESULTS OF THE NANOWIRE TRANSISTOR

The n-type nanowire transistor simulated in this chapter has the same physical parameters as the one simulated in Section 4.3. Hence, the smoothing parameter of the Effective Potential (σ) of this device is 0.4 nm. Figure 7.1 shows the 3D schematic of the n-type nanowire transistor investigated here. The width and the height are given by a square cross-section of dimension 10 nm, the buried oxide thickness is 75 nm. The metal gate is TiN (assuming its work function is 4.52 eV), and this transistor presents an EOT of 1.3 nm. The source and drain regions were dopped with donor dopants, using a doping density of $N_D = 4 \times 10^{19}$ cm^{-3}. The length of the channel is 40 nm, and the channel is undoped (N_A between 1×10^{15}cm^{-3} and 3×10^{15}cm^{-3}).

Figure 7.1: Schematic of the nanowire transistor investigated in this work. The silicon dioxide is represented in gray, the gate dielectric is represented in gray, the buried oxide is represented in light gray, and the silicon regions are represented in blue. The gate metal is represented in red. The region referred to as S represents the source, G represents the gate and D represents the drain. W_{fin} and H_{fin} represent the fin width and height respectively, and L represents the channel length.

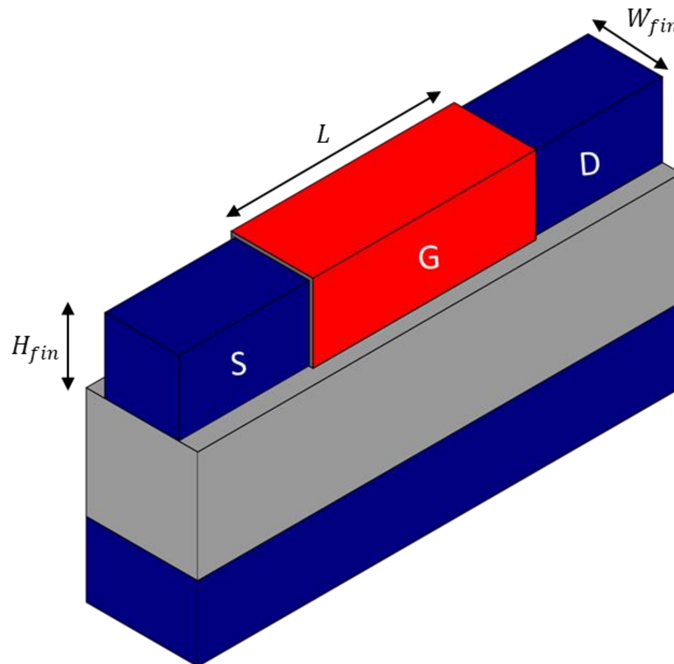

Source: Elaborated by the author.

Figure 7.2 presents the transfer characteristic curves of this device at V_D = 0.7 V obtained experimentally (PAVANELLO, 2023) and estimated by the quantum-corrected Monte Carlo device simulator presented in this work. The simulation curve is the average of twenty samples, simulated for 4 ps. For this device, the surface roughness scattering is modeled as 85% diffusive and 15% specular.

Figure 7.2: Transfer characteristic curve estimated by the quantum-corrected simulator (red) and measured experimentally (black). The curves represent the average value of the 20 samples. The error bars indicate 95% confidence interval. $V_{BS} = 0$ V, $V_{DS} = 0.7$ V.

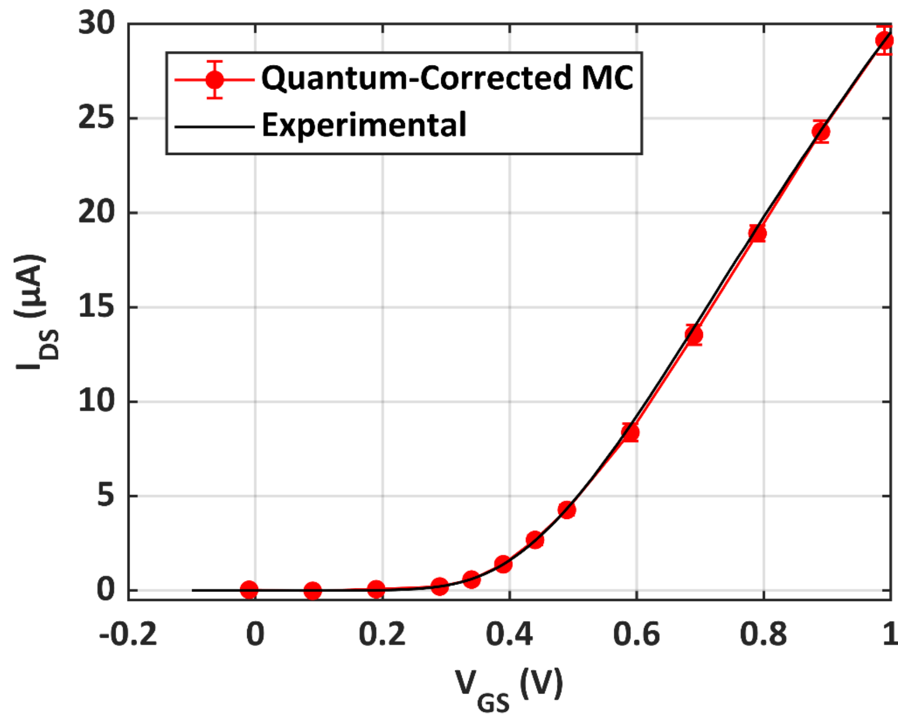

Source: Elaborated by the author.

Figure 7.3: Transfer characteristic curves in log scale estimated by the quantum-corrected simulator (red) and measured experimentally (black). The curves represent the average value of the 20 samples. The error bars indicate 95% confidence interval. $V_{BS} = 0$ V, $V_{DS} = 0.7$ V.

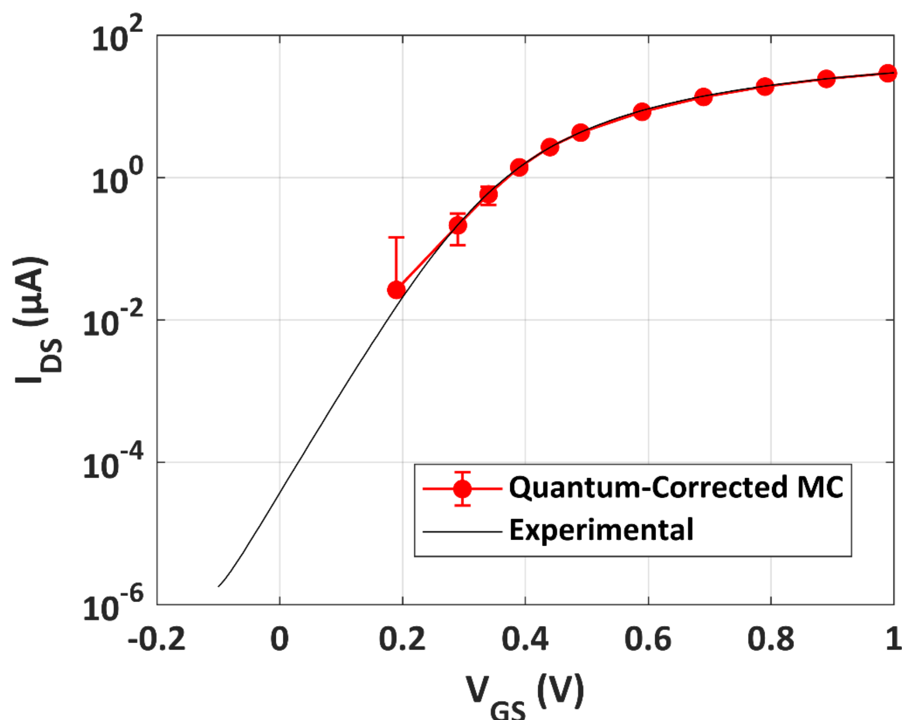

Source: Elaborated by the author.

Figure 7.3 shows the transfer characteristic curves in the log scale, in which the subthreshold region is better observed. There is a great agreement between the experimental and simulation results for the entire range of gate bias, which demonstrates that the quantum-corrected Monte Carlo device simulator is an adequate tool to investigate the electrical behavior and the reliability of this device.

The conduction band along the device length and height taken at the middle of the device width is shown in Figure 7.4. The Effective Potential smooths the conduction band in the region close to the silicon/silicon dioxide interface (encircled in Figure 7.4). Note that the discrete effect of dopant distribution in the source and drain regions is depicted in the conduction band.

Figure 7.4: Conduction band taken at the middle of the nanowire width calculated using the quantum-corrected simulator. The circles in red indicate the regions where the conduction band is smoothed. $V_{DS} = 0.7$ V, $V_{GS} = 0.9$ V and $V_{BS} = 0$ V.

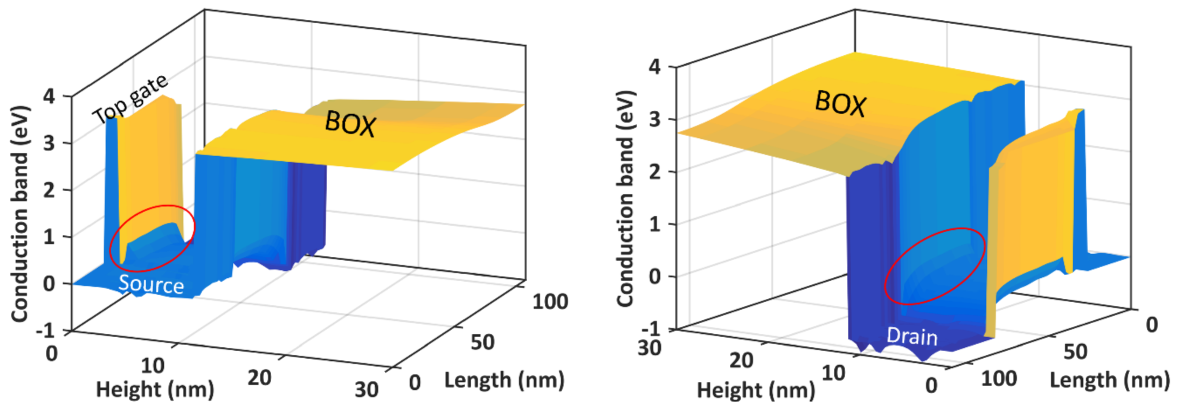

Source: Elaborated by the author.

The effect of quantum confinement on the electron distribution is shown in Figure 7.5 where the electron density along the fin width and height taken at the middle of the channel is depicted. Figure 7.5 shows that the inversion occurs a few nanometers away from the silicon/silicon dioxide interfaces (represented by the white dashed lines). Therefore, volume inversion is also modeled in the nanowire transistor by the Effective Potential.

Figure 7.6 shows the average number of phonon scattering events and surface roughness scattering events an electron undergoes while crossing the channel as a function of gate bias. It is shown that at low gate bias, phonon scattering is more likely to occur than surface roughness scattering. Therefore, in this range, the mobility is limited by phonon scattering mechanisms. However, at gate biases higher than 0.9 V, the surface roughness scattering becomes more relevant than phonon scattering. At this range of gate bias, electrons are being pushed towards all the three silicon/silicon dioxide interfaces by a higher electrostatic force, and because of that, they interact with the surface more often.

Figure 7.5: Electron density taken at a cross-section in the channel region calculated by the quantum-corrected simulator results. $V_{DS} = 0.7$ V, $V_{GS} = 0.9$ V and $V_{BS} = 0$ V.

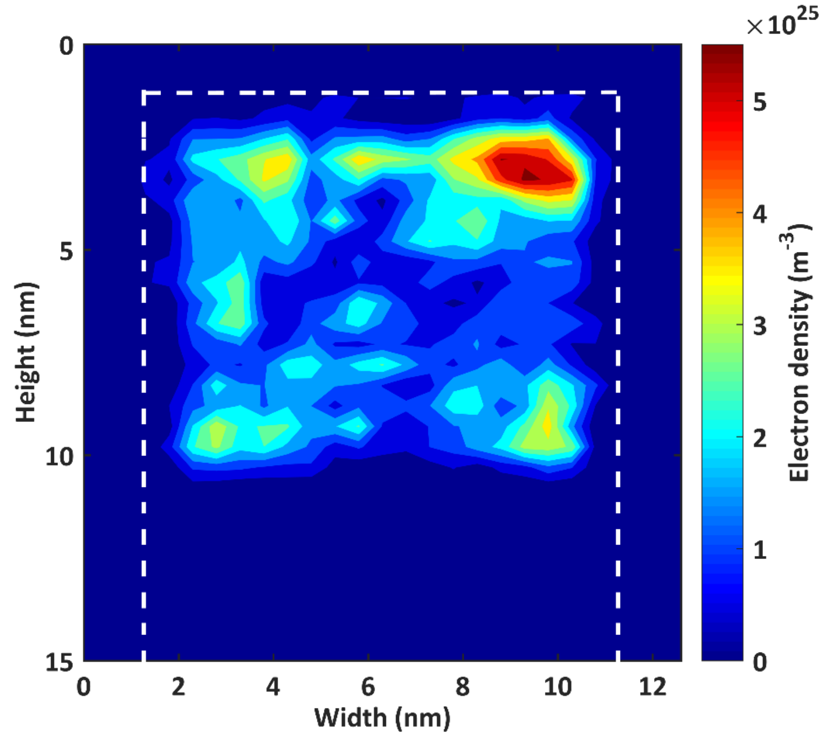

Source: Elaborated by the author.

Figure 7.6: Phonon scattering events (green) and surface roughness scattering events (magenta) per electron crossing the channel in the quantum-corrected simulator. The curves represent the average value of the 20 samples. The error bars indicate 95% confidence interval. V_{DS}=0.7 V, and $V_{BS} = 0$ V.

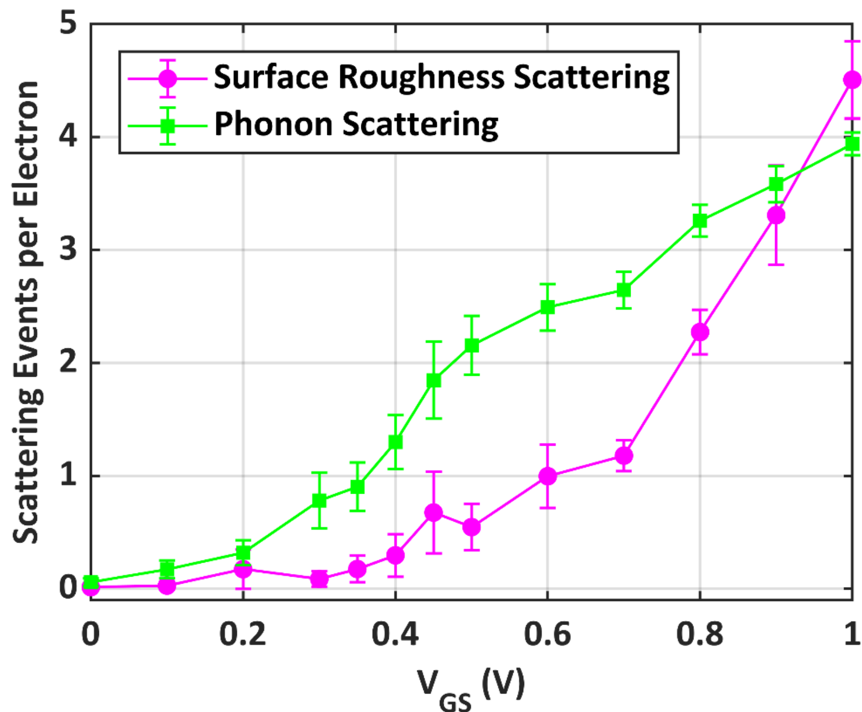

Source: Elaborated by the author.

7.1 Random Dopant Fluctuation

In the current technology, the channel of tri-gate transistors is said undoped. However, despite no intentional dopants are introduced, the channel may not be perfectly free of dopants (intrinsic), due to the fabrication process. Thus, undoped in the context of the studied device means that the doping density is very small (N_A is around 1×10^{15} cm^{-3} and 3×10^{15} cm^{-3}), while the intrinsic carrier density is around $n_i = 1.5 \times 10^{10}$ cm^{-3} at 300 K. The number of dopants in the channel amongst devices follows a Poisson distribution function (SRIVASTAVA; SYLVESTER; BLAAUW, 2005). For the nanowire transistor of interest, if $N_A = 3 \times 10^{15}$ cm^{-3}, the probability of having zero dopant atoms in the channel is 98.81%, the probability of having one dopant atom in the channel is 1.1857%, and the probability of having two dopant atoms is 0.0071%. This process variation is called random dopant fluctuation (RDF) and results in transistors with distinct numbers of dopants; hence, it is a source of device-to-device variability (GRASSER, 2014), (REIS; CAO; WIRTH, 2015).

As mentioned, in the Monte Carlo device simulator, the dopants are treated as discrete particles. Therefore, the effect of random dopant fluctuation can be investigated by the device simulator. In the case of study performed in this work, one dopant atom was inserted in the channel of the nanowire. The channel length of the nanowire transistor is 40 nm, and length of the source and drain regions are 34 nm; thus, the total length of the structure is 108 nm. The dopant was positioned at the center of the width (z = 6.3 nm), at 1.75 nm from the top silicon/silicon dioxide interface (y = 3.05 nm), and at 11 nm from the beginning of the channel (x = 45 nm). To reduce the Monte Carlo statistical noise, the same device was simulated with and without the dopant atom using 200 different Monte Carlo seeds. The simulations were carried out at 300 K, $V_B = V_S = 0$ V, $V_D = 0.2$ V, and $V_G = 0.5$ V for 10 ps. The average current and its standard error were estimated for both devices. The current of the device without dopants is 4.0478 ± 0.0185µA, while for the device with the dopant atom it is 3.4576 ± 0.0169 µA. The current variation δI induced by this dopant is 14.58% of the current without any dopant atom.

Figure 7.7 shows the electron density along the channel for the device without dopants in the channel and for the device with one dopant in the channel. The dopant is at x = 45 nm. The impact of the single dopant on the electron density is to significantly reduce the electron density over a large portion of the channel. The type of dopant in the channel is acceptor, thus, it electrostatically repels the electrons, which decreases the number of electrons in this region.

Figure 7.7: Electron density along the channel length of the device without any dopant in the channel (black curve) and of the device with one dopant in the channel at $x = 45$ nm (red curve). The channel length of the nanowire transistor is 40 nm (from $x = 34$ nm to $x = 74$ nm).

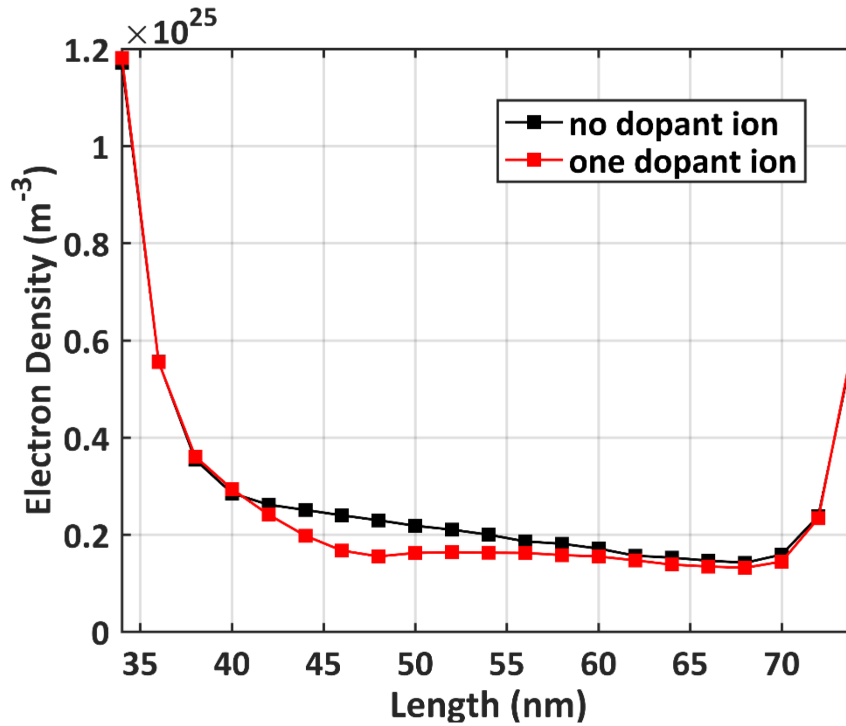

Source: Elaborated by the author.

Figure 7.8 Average velocity of electrons along the length of the device without any dopant in the channel (black curve) and of the device with one dopant in the channel at $x = 45$ nm (red curve). The channel length of the nanowire transistor is 40 nm (from $x = 34$ nm to $x = 74$ nm). The dashed lines represent the limits of the channel region.

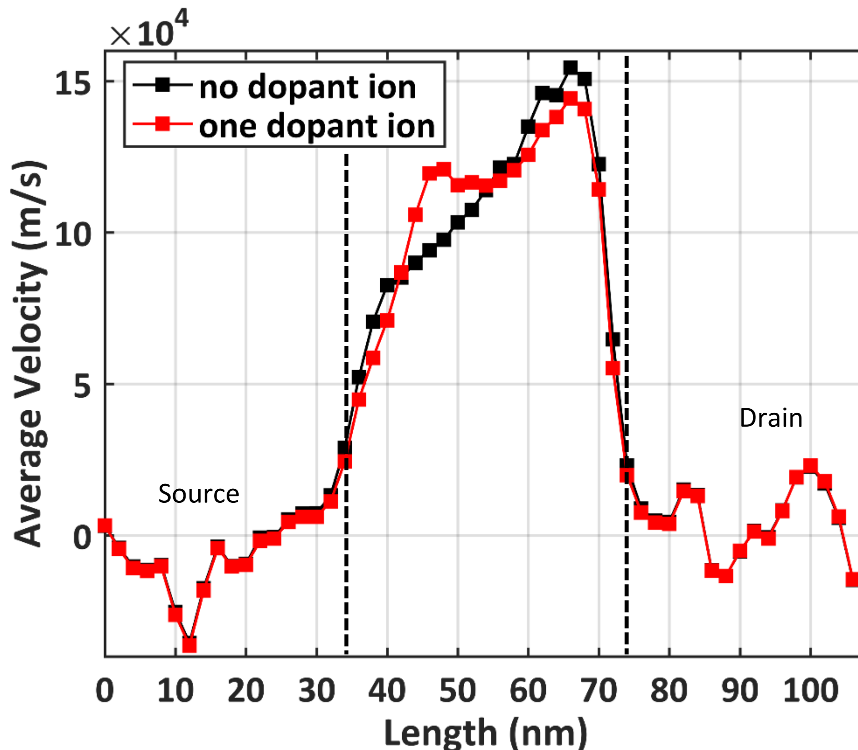

Source: Elaborated by the author.

Figure 7.8 depicts the velocity of the electrons along the channel for the device without dopants in the channel and for the device with one dopant. In the channel region where the dopant is located, the electron velocity is increased in comparison to the case without dopants. To support current conservation, the velocity of electrons in this region is higher, compensating for the smaller number of electrons. Note that in the channel region right after the dopant the electron velocity is almost flat. Considering that the electron density in the region around the dopant is smaller than in the rest of the channel, this gradient of electron density might generate diffusion of electrons that are right after the dopant position.

8 CONCLUSIONS AND FUTURE WORK

To implement the quantum correction in the Monte Carlo device simulator, firstly, a Schrödinger-Poisson solver and an Effective Potential-Poisson solver were developed to simulate the cross-section of silicon n-type FinFET and silicon n-type nanowire transistors. Then, the smoothing parameter of the Effective Potential of these devices was adjusted until the electron line density calculated using the Effective Potential-Poisson solver agrees with the one calculated using the Schrödinger-Poisson solver in a range of gate biases. For the n-type FinFET of interest, the Effective Potential smoothing parameter is equal to 0.45 nm, while for the n-type nanowire transistor, it is equal to 0.4 nm.

The Effective Potential was included in the Monte Carlo device simulator as a quantum correction to simulate the n-type FinFET transistor of interest. The FinFET simulated is unintentionally doped, with width and height equal to 8 nm and 42 nm, respectively, channel length of 18 nm, and EOT of 1.2 nm. This transistor was simulated using the semiclassical and the quantum-corrected simulator. The output and the transfer characteristic curves of this transistor were estimated using both simulators, and it was demonstrated that the semiclassical simulator overestimates the on-current. In the quantum-corrected simulator, it was observed that the channel is formed a few nanometers away from the interface, and it was shown that the volume inversion reduces the surface roughness scattering events. As a result of that, the electron's velocity along the channel is higher in the quantum-corrected simulator than in the semiclassical simulator. Although the electron's velocity along the channel is higher in the quantum-corrected simulator, the electron density in the channel is smaller due to quantum confinement, which degrades the on-current of the transistor. Overall, the effect of quantum confinement reduces the on-current in the FinFET transistor. The impact of the quantum-correction in the subthreshold region is small, because in this region, the transistor is on weak inversion; therefore, the potential well is not formed yet. As the gate bias increases, the band bending increases and a 2D quantum well is formed where the electrons are confined.

In terms of the n-type nanowire, an unintentionally doped nanowire with squared cross-section of 10 nm, EOT of 1.3 nm, and channel length of 40 nm was simulated. The transfer characteristic curve in the saturation region (V_D = 0.7 V) estimated by the quantum-corrected simulator was compared with experimental results. There is an excellent agreement between the simulation and experimental results, even in the subthreshold region. It was shown that the volume inversion is being modeled by the quantum-corrected simulator. The surface roughness

scattering mechanism in this transistor is relevant. Note that in the nanowire transistor there are four interfaces between silicon and silicon dioxide. In addition to that, the height of the nanowire transistor is about four times smaller than the height of the FinFET investigated in this work. Therefore, the interaction between the electrons and the surface is more likely to occur in the nanowire transistor than in the FinFET investigated. At gate biases smaller than 0.9 V, the phonon scattering events are more likely to occur than surface roughness scattering events. At gate biases higher than that, the electrons mobility is limited by surface roughness scattering. In addition, a brief study of the impact of RDF on the on current of the nanowire transistor was presented.

As future work it is suggested to perform a more extensive study concerning the effect of RDF on the nanowire transistor, where the position of the dopant atom is changed and the variation in current is measured as a function of the dopant position. In addition, an excellent contribution to this work would be perform an investigation of the impact of trap activity on the nanowire transistor employing the quantum-corrected Monte Carlo device simulator, employing the same methodology presented in ((ROSSETTO; CAMARGO; BOTH; VASILESKA; WIRTH, 2020). In terms of new transistors, it would be relevant to include the nanosheet transistor in the quantum-corrected device simulator, since it is expected to be the transistor of the next generation (YE; ERNST; KHARE, 2019), (AJAYAN, J. et al., 2021). To do that, the smoothing parameter of the Effective Potential for this transistor would have to be obtained. The 2D Schrödinger-Poisson solver and the 2D Effective Potential-Poisson solver can be easily adapted to simulate the cross-section of nanosheet transistors. In terms of the quantum-corrected device simulator, the structure of the nanosheet transistors has to be included and the boundary conditions should be modified to properly describe the interfaces and surfaces of the nanosheet transistors.

9 REFERENCES

AJAYAN, J. *et al*. Nanosheet field effect transistors-A next generation device to keep Moore's law alive: an intensive study. **Microelectronics Journal**, [S.L.], v. 114, p. 105141, ago. 2021. Elsevier BV. http://dx.doi.org/10.1016/j.mejo.2021.105141

AKIS, R., MILICIC, S. N., FERRY, D. K., & VASILESKA, D. An effective potential method for including quantum effects into the simulation of ultra-short and ultra-narrow channel MOSFETs. In M. Laudon, & B. Romanowicz (Eds.), 2001 International Conference on Modeling and Simulation of Microsystems - MSM 2001 (pp. 550-553).

ASCHROFT, N. W., MERMIN, N. D., **Solid State Physics**. Philadelphia, PA: Saunders College Publishing, 1976.

BAIKADI, Pranay Kumar Reddy. **Efficient Schrödinger-Poisson Solvers for Quasi 1D Systems That Utilize PETSc and SLEPc**. 2020. Tese de Mestrado. Arizona State University.

BALAY, Satish, et. all PETSc user's manual. Technical Report ANL-95/11 - Revision 3.14, Argonne National Laboratory, 2020.

BOHR, M. and MISTRY, K. Intel's revolutionary 22 nm transistor technology. Intel website; 2011.

BUFLER, F.M.; SCHENK, A.; FICHTNER, W.. Efficient Monte Carlo device modeling. **Ieee Transactions on Electron Devices**, [S.L.], v. 47, n. 10, p. 1891-1897, 2000. Institute of Electrical and Electronics Engineers (IEEE). http://dx.doi.org/10.1109/16.870568.

BUFLER, F.M.; SMITH, L. 3D Monte Carlo simulation of FinFET and FDSOI devices with accurate quantum correction, **Journal of Computational Electronics**, New York, v. 12, n. 12, p. 651–657, Dec. 2013.

CAMARGO, V. V. A. *Evaluating the Impact of Charge Traps on MOSFETs and Circuits*. PhD Thesis, Universidade Federal do Rio Grande do Sul, Porto Alegre, Brasil, 2016.

CAMARGO, Vinicius V. A.; ROSSETTO, Alan C. J.; VASILESKA, Dragica; WIRTH, Gilson I.. 3-D Monte Carlo device simulator for variability modeling of p-MOSFETs. **Journal Of Computational Electronics**, [S.L.], v. 19, n. 2, p. 668-676, 17 fev. 2020. Springer Science and Business Media LLC. http://dx.doi.org/10.1007/s10825-020-01461-1

COLINGE, J. P. FinFETs and Other Multi-gate Transistors. Springer, 2008.

COLINGE, J., & GREER, J. Nanowire Transistors: Physics of Devices and Materials in One Dimension. Cambridge: Cambridge University Press. (2016).

DENNARD, Robert H., GAENSSLEN, F.H., YU, H.N., RIDEOUT, V. L., BASSOUS, E., and LEBLANC, A.R., "Design of Ion-Implanted MOSFETS with Very Small Physical Dimensions," *IEEE J. Solid-State Circuits*, Vol. 51, pp. 256- 264, 1974

ESSENI, David; PALESTRI, Pierpaolo; SELMI, Luca. **Nanoscale MOS transistors: semi-classical transport and applications**. Cambridge University Press, 2011.

FERRY, D. K. “The onset of quantization in ultra-submicron semiconductor devices”. *Superlattices and Microstructures*, Vol. 27, n. 2/3, pp. .62-66, 2000.

FERRY, D. K. *An Introduction to Quantum Transport in Semiconductors*, Pan Stanford Publishing, 2018.

FISCHETTI, Massimo V.; LAUX, Steven E.. Monte Carlo analysis of electron transport in small semiconductor devices including band-structure and space-charge effects. **Physical Review B**, [S.L.], v. 38, n. 14, p. 9721-9745, 15 nov. 1988. American Physical Society (APS). http://dx.doi.org/10.1103/physrevb.38.9721

FUCHS, K. “The conductivity of thin metallic films according to the electron theory of metals”. Mathematical Proceedings of the Cambridge Philosophical Society, 34(1), (1938). https://doi.org/10.1017/S0305004100019952

FURTADO, G.F. **State-of-the-art 3-D Monte Carlo Device Simulation: from n-MOSFETs to n-FinFETs.** Dissertation (Doctorate in Microelectronics) - Universidade Federal do Rio Grande do Sul, Porto Alegre, Brasil, 2021.

FURTADO, Gabriela F.; CAMARGO, Vinicius V. A.; VASILESKA, Dragica; WIRTH, Gilson I.. Correlation of HCD and Percolation Paths in FinFETs: study of RDF and MGG impacts through 3-D particle-based simulation. **IEEE Transactions on Device and Materials Reliability**, [S.L.], v. 22, n. 3, p. 381-386, set. 2022. Institute of Electrical and Electronics Engineers (IEEE), https://doi.org/10.1109/TDMR.2022.3178900

FURTADO, Gabriela F.; CAMARGO, Vinicius V. A.; VASILESKA, Dragica; WIRTH, Gilson I.. Evaluating the Ballistic Transport in nFinFETs: a carrier centric perspective. **IEEE Transactions on Nanotechnology**, [S.L.], v. 21, p. 311-319, 2022. Institute of Electrical and Electronics Engineers (IEEE), https://doi.org/10.1109/TNANO.2022.3186147

FURTADO, Gabriela Firpo; CAMARGO, Vinícius Valduga de Almeida; VASILESKA, Dragica; WIRTH, Gilson Inácio. 3-D TCAD Monte Carlo Device Simulator: state-of-the-art finfet simulation. **Journal Of Integrated Circuits and Systems**, [S.L.], v. 16, n. 2, p. 1-11, 16 ago. 2021. Journal of Integrated Circuits and Systems.https://doi.org/10.29292/jics.v16i2.476

GONZALEZ, S. **Empirical pseudopotential method for the band structure calculation of strained Si1-xGex materials**. Thesis (Master of Science) - Arizona State University, Tempe, AZ, 2001.

GRASSER, T. *Bias Temperature Instability for Devices and Circuits*. Springer, 2014.

GROSS, W. J. Three-dimensional Particle-based Simulations of Deep Sub-micron MOSFET Devices. Tese (Doutorado)—Arizona State University, Tempe, U.S.A., 1999.

HAMAGUCHI, C. **Basic Semiconductor Physics**. Alemanha, Springer Berlin Heidelberg, 2013.

HAMAGUCHI, C. **Basic Semiconductor Physics**. New York: Springer, 2001.

HAN, W. and WANG, Z. M. *Toward Quantum FinFET*. Springer, 2013.

HERRING, Conyers; VOGT, Erich. Transport and Deformation-Potential Theory for Many-Valley Semiconductors with Anisotropic Scattering. **Physical Review**, [S.L.], v. 101, n. 3, p. 944-961, 1 fev. 1956. American Physical Society (APS). http://dx.doi.org/10.1103/physrev.101.944.

JACOBONI, C. **Theory of Electron Transport in Semiconductors**: A Pathway from Elementary Physics to Nonequilibrium Green Functions. Springer, 2010.

JACOBONI, C., LUGLI, P. **The Monte Carlo Method for Semiconductor Device Simulation**. First edition. Springer-Verlag, New York, 1989.

KANO, K. **Semiconductor Devices**. New Jersey: Prentice Hall, 1998.

KHANNA, V. K. *Integrated Nanoelectronics: Nanoscale CMOS, Post-CMOS and Allie Nanotechnologies. NanoScience and Technology*. Springer India 2016.

KOBAYASHIA, M. AND HIRAMOTO, T. Experimental study on quantum confinement effects in silicon nanowire metal-oxide-semiconductor field-effect transistors and single-electron transistors. Journal of Applied Physics 103, 053709 (2008); doi: 10.1063/1.2874247

LAUX, S. E. and FISCHETTI, M. V., "Monte Carlo study of velocity overshoot in switching a 0.1-micron CMOS inverter," **International Electron Devices Meeting.** IEDM Technical Digest, Washington, DC, USA, 1997, pp. 877-880, https://doi.org/10.1109/IEDM.1997.650521

LEE, H. et al., "Sub-5nm All-Around Gate FinFET for Ultimate Scaling," 2006 Symposium on VLSI Technology, 2006. Digest of Technical Papers., 2006, pp. 58-59, doi: 10.1109/VLSIT.2006.1705215.

LUNDSTROM, M. **Fundamentals of Carrier Transport**. Cambridge, U.K: Cambridge University Press, 2000.

LUNDSTROM, M. *Fundamentals of Nanotransistors*. World Scientific Publishing Company, 2016

MOORE, Gordon E., “Cramming more components onto integrated circuits”. *Electronics*, Vol. 38, n. 8, pp. 114-117, 1965.

N. Mendiratta and S. L. Tripathi “A review on performance comparison of advanced MOSFET structures below 45 nm technology node” *Journal of Semiconductors*, Vol. 41, n. 6, 2020.

NAYAK, D. K., WOO, J. C. S., PARK, J. S., WANG, K. and MACWILLIAMS, K. P., "Enhancement-mode quantum-well Ge/sub x/Si/sub 1-x /PMOS," *IEEE Electron Device Letters*, Vol. 12, n. 4, pp. 154-156, April 1991, https://doi.org/10.1109/55.75748.

PAVANELLO, M. A. Dados de corrente versus tensão de porta de transistores nanofio. 2023

RAMAYYA, E. B.; KNEZEVIC, I. Self-consistent Poisson-Schrödinger-Monte Carlo solver: electron mobility in silicon nanowires. **Journal Of Computational Electronics**, [S.L.], v. 9, n. 3-4, p. 206-210, 28 out. 2010. Springer Science and Business Media LLC. http://dx.doi.org/10.1007/s10825-010-0341-8.

RAMEY, S.M. FERRY, D.K. Modeling of quantum effects in ultrasmall FD-SOI MOSFETs with effective potentials and three-dimensional Monte Carlo, Physica B: Condensed Matter, Volume 314, Issues 1–4, 2002, Pages 350-353.

RAMEY, Stephen M. *The effective potential in simulation of SOI MOSFETS*. PhD Thesis, Arizona State University, Tempe, AZ, USA, 2003.

REIS, Ricardo; CAO, Yu; WIRTH, Gilson (Ed.). **Circuit design for reliability**. New York, NY: Springer New York, 2015.

RODRÍGUEZ-BOLÍVAR, S; GÓMEZ-CAMPOS, F M; CARCELLER, J. Simple analytical valence band structure including warping and non-parabolicity to investigate hole transport in Si and Ge. **Semiconductor Science and Technology**, [s.l.], v. 20, n. 1, p.16-22, 27 nov. 2004. IOP Publishing. http://dx.doi.org/10.1088/0268-1242/20/1/003.

ROMAN, J. E. CAMPOS, C. ROMERO, E. and TOMAS, A. Slepc user's manual. D. Sistemas Informáticos y Computación, Universitat Politecnica de Valencia, Valencia, Spain, Report No. DSIC-II/24/02, 2015.

ROSSETTO, A. C. **Modeling and Simulation of Self-heating Effects in p-type MOS Transistors.** Dissertation (Doctorate in Microelectronics) - Universidade Federal do Rio Grande do Sul, Porto Alegre, Brasil, 2018.

ROSSETTO, Alan C. J.; CAMARGO, Vinicius V. A.; BOTH, Thiago H.; VASILESKA, Dragica; WIRTH, Gilson I.. Statistical analysis of the impact of charge traps in p-type MOSFETs via particle-based Monte Carlo device simulations. **Journal Of Computational Electronics**, [S.L.], v. 19, n. 2, p. 648-657, 6 mar. 2020. Springer Science and Business Media LLC https://doi.org/10.1007/s10825-020-01478-6.

SÓLYOM, J. Fundamentals of the Physics of Solids. V.1 – Structure and Dynamics. Springer-Verlag Berlin Heidelberg, 2007.

SRIVASTAVA, Ashish; SYLVESTER, Dennis; BLAAUW, David. **Statistical analysis and optimization for VLSI: Timing and power**. New York: Springer, 2005.

STONE, H. L., "Iterative solution of implicit approximations of multidimensional partial differential equations." **SIAM Journal on Numerical Analysis**, v. 5, n. 3, p. 530-558, 1968.

VASILESKA, D. and ASHRAF, N. "Atomistic Simulations on Reliability". In: Reis R., Cao Y., Wirth G. (eds) *Circuit Design for Reliability*. Springer, New York, NY, 2015. https://doi.org/10.1007/978-1-4614-4078-9_4

VASILESKA, D., GOODNICK S. M. and KLIMECK, G.: **Computational Electronics: From Semi-Classical to Quantum Transport Modeling**, CRC Press, June 2010.

VASILESKA, D., GOODNICK S. M.: **Computational Electronics**, Morgan and Claypool Publishers, 2006.

VASILESKA, D., KNEZEVIC, I., AKIS, R. ET AL. The Role of Quantization Effects on the Operation of 50 nm MOSFETs, 250 nm FIBMOS Devices and Narrow-Width SOI Device Structures. Journal of Computational Electronics 1, 453–465 (2002). https://doi.org/10.1023/A:1022980703489

VASILESKA, D.; GROSS, W.J.; FERRY, D.K. Monte Carlo particle-based simulations of deep-submicron n-MOSFETs with real-space treatment of electron–electron and electron–impurity interactions. **Superlattices And Microstructures**, [S.L.], v. 27, n. 2-3, p. 147-157, fev. 2000. Elsevier BV. http://dx.doi.org/10.1006/spmi.1999.0806

WU, Y. and SU, P. "Analytical Quantum-Confinement Model for Short-Channel Gate-All-Around MOSFETs Under Subthreshold Region," in IEEE Transactions on Electron Devices, vol. 56, no. 11, pp. 2720-2725, Nov. 2009, doi: 10.1109/TED.2009.2030714.

YAMAKAWA, S. *Transport Modeling in GaN Materials and Devices Based on Full-Band Cellular Monte Carlo Simulation*, PhD Thesis, Arizona State University, Tempe, AZ, USA, 2005.

YE, P. ERNST, T. and KHARE, M. The last silicon transistor: Nanosheet devices could be the final evolutionary step for Moore's Law, **IEEE Spectrum**, vol. 56, no. 8, pp. 30-35, Aug. 2019, doi: 10.1109/MSPEC.2019.8784120

YORSTON, Ronald M. Free-flight time generation in the Monte Carlo simulation of carrier transport in semiconductors. **Journal of Computational Physics**, [S.L.], v. 64, n. 1, p. 177-194, maio 1986. Elsevier BV. http://dx.doi.org/10.1016/0021-9991(86)90024-0